Polarization modeling and predictions for DKIST, part 8: calibration polarizer spatial variation impacts

David M. Harrington,[a,*] Tom Schad,[a] Stacey Sueoka,[b] and Amanda J. White[b,c]

[a]National Solar Observatory, Makawao, Hawaii, United States
[b]National Solar Observatory, Boulder, Colorado, United States
[c]University of Colorado, Department of Astrophysical and Planetary Sciences, Boulder, Colorado, United States

Abstract. Astronomical spectropolarimeters require high accuracy polarizers with large aperture and stringent uniformity requirements. In solar applications, wire grid polarizers are often used as performance is maintained under high heat loads and temperatures over 200°C. DKIST is the NSF's new 4-m aperture solar telescope designed to deliver accurate spectropolarimetric solar data across a wide wavelength range, covering a large field of view simultaneously using multiple facility instruments. Polarizers at 120 mm diameter are used to calibrate DKIST instruments but vary spatially in transmission, extinction ratio, and orientation of maximum extinction. We combine new spatial and spectral metrology for polarizers and retarders to simulate the accuracy losses with field angle and wavelength caused simultaneously by spatial variation of several optical parameters including beam decenter from misalignments. We also present testing of a new crystal sapphire substrate polarizer designed and fabricated to improve DKIST long wavelength calibrations. We assess spatial thickness variation of sapphire and fused silica wafer substrates using spectral interference fringes. [DOI: 10.1117/1.JATIS.7.3.038002]

Keywords: instrumentation; polarization; Mueller matrix; Daniel K. Inouye Solar Telescope; spectropolarimetry.

Paper 21026 received Mar. 6, 2021; accepted for publication Jul. 15, 2021; published online Aug. 2, 2021.

1 Introduction: DKIST and Polarization Models for Calibration

The National Science Foundation's Daniel K. Inouye Solar Telescope (DKIST) on Haleakalā, Maui, Hawai'i is presently transitioning from ending of the construction phase to an early operations phase. The telescope has a 4.2-m-diameter off-axis $F/2$ primary mirror folding a 4.0-m-diameter circular beam. Four separate spectropolarimeters are being installed in the coudé laboratory, each with multiple sensors of various imaging capabilities and wavelength ranges.[1–4] All instruments have spectral resolving power above 30,000 and some achieve over 300,000 in certain cases. Each instrument has optomechanical methods to allow for stepping the instrument sensor field of view across a much larger portion of the DKIST beam field of view. All instruments deliver imaging spectropolarimetry of some kind either by scanning through wavelengths with Fabry–Perot systems, stepping slit masks across a focal plane, tilting field scanning mirrors near pupil planes, and/or using imaging fiber bundles. These techniques build up imaging spectropolarimetric capability over visible and near-infrared wavelengths. DKIST is specified to operate at least eight spectropolarimetric cameras simultaneously at frame rates of at least 40 Hz to achieve the combined spatial, spectral, and temporal polarimetric goals. Accurate polarization calibration of this instrument suite is a critical scientific performance driver. A recent observatory overview was provided in Ref. 1.

*Address all correspondnce to David M. Harrington, dharrington@nso.edu

DKIST uses six mirrors to collect and relay light to a rotating coudé lab to provide flexible capabilities.[2,5–11] The first two mirrors, comprising the off-axis Gregorian telescope, are static with respect to the alt/az telescope mount. DKIST has a Gregorian Optical System (GOS) built around the secondary Gregorian focus. The GOS contains a level for apertures, stops, and calibration targets at Gregorian focus. The GOS also contains retarders, polarizers, and artificial light sources at other levels roughly 350 to 550 mm ahead of the Gregorian focus.[8,12–17] Four polarimetric instruments presently spanning the 380- to 5000-nm wavelength range are in various phases of construction or installation on the summit in the coudé lab. The visible spectropolarimeter (ViSP) is a three-arm slit-based spectropolarimeter. The visible tunable filter is a tunable Fabry–Perot-type imaging spectropolarimeter.[18,19] The diffraction-limited near-infrared spectropolarimeter (DL-NIRSP) is a fiber-bundle fed imaging spectropolarimeter. The cryogenic near-infrared spectropolarimeter (Cryo-NIRSP) is also a slit-based infrared optimized system. We also have two high speed (30 Hz) 4k full frame cameras within the visible broadband imager red and blue instruments (VBI-red and VBI-blue).[20–26]

Three static mirrors level and collimate the beam in the coudé laboratory (M7 through M9). Then, a sequence of dichroic beam splitters, windows, and/or mirrors called the facility instrument distribution optics (FIDO) allows changing of instrument configurations on a timescale of less than half an hour. The FIDO optics allow simultaneous operation of three polarimetric instruments optimized for 380 to 1800 nm while using the facility adaptive optics (AO) system for correction to provide diffraction-limited performance.[8,9,19,27,28] All AO-assisted instruments see the first beamsplitter in the wavefront correction system (WFC-BS1) in transmission. The optics are designed such that the wedge angles are matched in each optic, and every instrument sees either two or four beamsplitters in transmission to compensate for the wedge and associated wavelength variation in beam deflection. Cryo-NIRSP can receive all wavelengths to 5000 nm but without use of the AO system in a seeing limited, all-reflective beam path fed by a FIDO pick-off mirror called M9a.

All instruments are supported by the DKIST data center. The center will receive and calibrate 3000 TB of new data per year with 8 TB expected on an average day.[29–31] We refer the reader to recent papers outlining the various capabilities of the first-light instruments.[2,2,4,6,8,9] Complex polarization modulation and calibration strategies are required for multi-instrument astronomical systems.[8,9,12,13,32,33] The planned 4-m on-axis European Solar Telescope (EST) will also require similar calibration considerations.[34–36] Many solar and night-time telescopes have performed polarization calibration of complex many-mirror pathways.[37–60]

This paper continues a series deriving polarization performance expectations for the DKIST telescope and instruments. In Ref. 61 (HS17), we outlined the DKIST optical layout and system Mueller matrix properties when using a simple enhanced silver mirror coating model. In Ref. 62 (H17), we showed polarization calibrations of a night-time telescope with a ViSP using the daytime sky. In Ref. 63 (H18), we applied the Berreman calculus[64,65] to polarization fringes formed in multilayer crystals with predictions and data collected in the lab and at a solar telescope. We then extended this calculus in Ref. 63 (HS18a) to include fringe magnitude estimates in converging and diverging beams. We recently have investigated spatial variation of retardance across multilayer retarders made of polished crystals, stretched polycarbonate, and ferroelectric liquid crystals in Ref. 66 (HS18b). This variation was then included in the DKIST optical model to show polarization calibration errors as functions of field angle and wavelength. In Ref. 67 (H19), we extend the coating efforts of HS17[61] to many mirror types from multiple vendors, highly enhanced metal coatings, hundred-layer dichroic coatings, and our system of beam splitters. We show additional mirror measurements and new ellipsometric metrology from an outside vendor (J. A. Woollam) in H21[68] at a range of incidence angles matching the DKIST mirrors to improve the system polarization model.

We have recently updated our laboratory metrology equipment to measure spatial variation of transmission to better than 0.01%, polarizer contrast ratio easily in excess of 100,000, and orientation changes in the polarizer extinction axis at levels below 0.002 deg. We combine these polarizer imperfections with spatial variation of the calibration retarders with improved spatial transmission variations combined with the retardance spatial variation reported previously in HS18b.[66] These errors in calibration optics can all influence the calibration accuracy for all observatory data products. We show here estimates for the calibration accuracy impact using

our newly measured calibration polarizer optical properties. We create synthetic data sets using imperfect polarizer and retarder optics. We include spatial variation across individual beam footprints in a Mueller matrix propagation simulation. This simulation creates synthetic modulated data as a function of field angle and wavelength as the footprints sample the calibration optics well away from the optical bore sight. With the synthetic data, we then explore several calibration algorithms and assess the accuracy of the derived modulation matrices. This provides error limit estimates and tools for assessing DKIST calibration accuracy. We run our simulations over the AO-assisted DKIST instrument suite wavelength range and cover field angles out to ± 1.9 arc min as the current limit of our spatial metrology data sets.

In addition to the spatial variation of the calibration optics, we also include additional errors caused by imperfect mounting and beam alignment. If an optic is spun while not perfectly centered in a beam, the spatial variations of that optic will cause changes in derived polarization that depends on the orientation and decentering. The DKIST active optics system (aO) and AO systems coordinate alignment of the beam.[5,7,28,69–72] However, this correction uses moving optics in the telescope to compensate the beam in the WFC installed in coudé laboratory. Imperfect optical alignment can lead to increased decenters on telescope optics to enforce centering of the pupil image and focal plane inside the WFC. The beam footprints on the calibration optics are not actively stabilized, leading to changes in beam centering with all axes of motion. Gravity-induced flexure is only partially compensated by the ao system leaving at least ~ 1 mm of motion throughout a day. The GOS optics themselves are also decentered by an additional 2.5 mm, awaiting an opportunity for recentering.

We have a dedicated metrology tool called the National Solar Observatory Coudé lab Spectro-Polarimeter (NCSP) described in H21.[68] This system calibrates the full telescope using either our Gregorian focus calibration lamp or the solar beam itself. The calibration optic misalignments present limitations in calibration accuracy even for the on bore sight beam. The quasistatic wavefront control system is implemented using the push–pull actuators on M1, constrained hexapod motion control on M2, tip-tilt control of M3 (near a focal plane steering the pupil), and tip-tilt control of both M5 and M6 (near a pupil plane, steering the focal plane). As these mirrors are actuated to stabilize the WFC beam, the beam will wander on the polarization calibration optics. In the future, the mirror controllers can position their mirrors based on lookup tables that calculate the best position based on telescope elevation, azimuth, temperature, and temperature gradient across M1.[69] For now, the mirrors are only positioned to a single static position with beam pointing variations as the system changes azimuth, elevation, and coudé table angle. As we noted in H21,[68] the DKIST coudé lab beam was only stabilized to roughly ± 9.7 arc sec field angle during some of our early polarization calibrations. Recent alignment work and on-going optical installations make this number dependent on construction project activities, changing frequently, with a range over ± 15 arc sec anticipated. For the optical path to our NCSP and the Cryo-NIRSP, the aO and AO systems are not simultaneously sampling the coudé beam. This leads to temporal drifts in the beam centering and preliminary polarization calibration errors at levels we simulate in this paper. We explore the impact of decentered beams coupled spatial variation both across the beam footprint and with field dependence.

Spectral interference fringes also adversely impact polarization accuracy for astronomical instruments requiring optical fringe modeling and/or removal methods through design and data processing.[47,48,59,73–85] We outline in this paper, the detection of spectral interference fringes in both sapphire and fused silica polarizer substrates. We measure spatial variation of these fringes using a higher spectral resolving power upgrade to our custom lab metrology tools. We calculate spectral and spatial fringe properties anticipated for our $F/13$ converging beam at the GOS calibration station and outline how polarizer fringes may be present in other astronomical systems. We designed and built several newly upgraded polarization optics based on polycarbonate and optically contact crystal designs in Ref. 87 (H20). These retarders suppress polarization fringes by one to three orders of magnitude compared to the previously designed multilayer crystal optics. We also identified alignment errors between individual crystals as a major source of retarder error. Misalignment produces spectral oscillations in retardance, which introduce a coupling between temperature changes and the spectral drift of these elliptical retardance oscillations. We showed in H21[68] detection of the clocking oscillations outlined in H20[86] with

calibrations both on-sun and with the DKIST calibration lamp. We also showed in H21[68] successful on-sun use of the optically contacted calibration retarder (OCcal) and system calibration with time-efficient calibration sequences. We compile here additional information about the interference fringe properties anticipated for our polarizers.

1.1 *System Model for Calibration*

$$\mathbf{M} = \begin{pmatrix} II & QI & UI & VI \\ IQ & QQ & UQ & VQ \\ IU & QU & UU & VU \\ IV & QV & UV & VV \end{pmatrix}. \tag{1}$$

Most large modern telescopes are articulated in azimuth and elevation and require a pointing-dependent system model. Polarization calibration requires removing the influence of the telescope mirrors. The Mueller matrix is the 4×4 matrix that transfers Stokes vectors.[87–89] Each element of the Mueller matrix is denoted by a transfer coefficient.[89,90] For instance, the coefficient [0,1] in the first row transfers Q to I and is denoted QI. The first row terms are denoted II, QI, UI, VI. The first column of the Mueller matrix elements are II, IQ, IU, IV. In this paper, we will use the notation in Eq. (1). The output Stokes vector is related to the input vector via a simple transfer equation $\mathbf{S}_{\text{out}} = \mathbf{M}\mathbf{S}_{\text{in}}$ using the standard matrix multiplication. With this formalism, the Stokes vector from some patch of solar atmosphere would be transferred by the Mueller matrix of each optic between the sun and the sensor:

$$\begin{pmatrix} i_1 \\ i_2 \\ \cdots \\ i_n \end{pmatrix} = \begin{pmatrix} O_{I1} & O_{Q1} & O_{U1} & O_{V1} \\ O_{I2} & O_{Q2} & O_{U2} & O_{V2} \\ \cdots & \cdots & \cdots & \cdots \\ O_{Im} & O_{Qm} & O_{Um} & O_{Vm} \end{pmatrix} \begin{pmatrix} I \\ Q \\ U \\ V \end{pmatrix}. \tag{2}$$

The modulation matrix is commonly defined as m modulation states by four Stokes vector components multiplying the incident Stokes vector to create a column vector of detected intensities (i).[48,51–53,91–98] Equation (2) shows this matrix multiplication. We use subscripts ($IQUV$) in the first index of the modulation matrix (O) to denote which Stokes vector component is being modulated. The numerical second index ($1,2,\ldots,m$) denotes the modulation state 1 through m corresponding to the modulating retarder setting (orientation, voltage, etc.).

1.2 *Calibration Input Sequence: 10 States Created with a Polarizer and Retarder*

$$\mathbf{M}_{\text{Stokes}} = \begin{pmatrix} I_1 & Q_1 & U_1 & V_1 \\ I_2 & Q_2 & U_2 & V_2 \\ \cdots & \cdots & \cdots & \cdots \\ I_n & Q_n & U_n & V_n \end{pmatrix}. \tag{3}$$

The end-to-end system Mueller matrix or modulation matrix can be calibrated by injecting a series of known polarization states using well-characterized polarization calibration optics, which for DKIST include linear polarizers followed by elliptical retarders. Below, we simulate a specific sequence of calibration optic orientations to generate a diverse set of Stokes vectors. For operational efficiency, DKIST must calibrate as many instruments as possible in a simultaneous configuration. For thermal forcing and efficiency, the measurement duration needs to be minimized while maintaining robustness. Thermal performance and heat loading of downstream optics also suggests several reasons to leave the polarizer always in the beam ahead of the retarder. Minimizing the calibration sequence total duration while ensuring near-optimal

photon-limited uncertainties involves maximizing what we refer to as the calibration efficiency, which is an analog to modulation efficiency.[48,92,95,99]

In Ref. 100 on the polarization calibration of the Swedish Solar Telescope, some simple optimization procedures are summarized. In Sec. 2.5.2 of Ref. 100, the orthogonality of the Stokes vectors created by the calibration unit is assessed in matrix form with one row per input state. Equation (3) shows the Stokes vector matrix ($\mathbf{M}_{\text{Stokes}}$) used to derive the condition number and the relative calibration efficiency of the exposure sequence for input vectors from 1 to n. The pseudoinverse of $\mathbf{M}_{\text{Stokes}}$ is created as $E_{i,j} = (\mathbf{M}_{\text{Stokes}}^T \mathbf{M}_{\text{Stokes}})^{-1} \mathbf{M}_{\text{Stokes}}^T$. The efficiencies are computed from the pseudoinverse as the usual sum of squared elements $e = (n \sum_1^n E^2)^{-0.5}$ where n is the number of input states. This pseudoinverse (E) can also be assessed by its condition number. This is the same approach as for finding optimum demodulation matrices.[48,92,95,99]

In our National Solar Observatory Lab Spectropolarimeter (NLSP) used for metrology in our prior DKIST calibration papers, an ansatz sequence was implemented to measure polarization with high efficiency across 380 to 1650 nm wavelengths. The sequence used 60 deg steps and a 30-deg offset between the retarder fast axis at 630 nm wavelength. The sequence worked well for reconstructing sample Mueller matrices with simultaneous fits to all polarization optic parameters. We guessed a similar sequence for DKIST polarization calibration with 10 input states in Table 1. The first column (Pol) shows the polarizer orientation in degrees. The second column (Ret) shows the retarder orientation in degrees. For most astronomical instruments, the sequences include additional measurements where the calibration optics are removed from the beam, typically called the clear exposures. We ignore these clear measurements where both optics are OUT in Table 1. The ansatz sequence uses three polarizer-only states and then another six states with both polarizer and retarder in the beam. There are no exposures with the retarder alone in the beam. We allowed for one free exposure to optimize the sequence efficiency for the multiple different retarders fabricated for DKIST. This additional exposure brought the total number of input states to 10. This extraoptimization followed the same technique we outlined in Sec. 7.4 of HS18b,[66] delivering high efficiencies over the 380 to 1650 nm range. On-sky demonstrations for DKIST calibrations were shown in H21.[68] The brute force fitting routine finds an orientation of 0 deg with the polarizer at 45 deg provides an improvement in efficiency balance for one of the DKIST calibration retarders (ViSP SAR). This is highlighted as the bold final line of Table 1. Intuitively this is sensible as the three polarizer-alone states create linear polarization suggesting the states with the retarder should make substantial circular polarization with a diversity of orientations.

Table 1 $N = 10$.

Pol	Ret
0	Out
60	Out
120	Out
0	0
0	60
0	120
45	30
45	90
45	150
45	**0**

1.3 *Modulation Matrix: Rotating Retarder and Analyzing Polarizer*

$$\mathbf{O}_i = \Omega \mathbf{M}_a \mathbf{M}_{LR}(\theta_i). \tag{4}$$

In the synthetic data generation used herein, we simulate a simple ideal polarimeter using a retarder and perfect analyzing polarizer as a proxy for an instrument modulation matrix. A simple true modulation matrix ($\mathbf{O}$) is used for all simulated wavelengths and field angles with a theoretical model for a 127-deg pure linear retarder rotating as a modulator. Uniformly spaced 30 deg steps are used to provide the same theoretical six state modulation for all simulations. We start the modulation with a half step offset of 15 deg to create symmetry in the modulation matrix as the retarder Mueller matrix would be a symmetric function of rotation angle ($\mathbf{M}_{LR}(\theta_i)$). A theoretical polarizer is used for the Mueller matrix of the analyzer ($\mathbf{M}_a$):

$$\mathbf{O}_{\text{true}} = \begin{pmatrix} 1 & 0.6 & 0.7 & -0.4 \\ 1 & -0.6 & 0 & -0.8 \\ 1 & 0.6 & -0.7 & -0.4 \\ 1 & 0.6 & 0.7 & 0.4 \\ 1 & -0.6 & 0 & 0.8 \\ 1 & 0.6 & -0.7 & 0.4 \end{pmatrix}, \tag{5}$$

$$\mathbf{D}_{\text{true}} = \begin{pmatrix} 0.13 & 0.25 & 0.13 & 0.13 & 0.25 & 0.13 \\ 0.21 & -0.42 & 0.21 & 0.21 & -0.42 & 0.21 \\ 0.36 & 0. & -0.36 & 0.36 & 0. & -0.36 \\ -0.21 & -0.42 & -0.21 & 0.21 & 0.42 & 0.21 \end{pmatrix}. \tag{6}$$

We show the derivation of the true modulation matrix for each modulation state ($\mathbf{O}_i$) for each orientation (θ_i) of the rotating pure linear retarder in Eq. (4). The matrix Ω represents the detector only recording total flux without any sensitivity to the transmitted polarization state. This matrix is written as [1,0,0,0] and is applied after propagation through the ideal analyzer (perfect linear polarizer). In real detector systems, there is some wavelength-dependent polarized response from optics between the analyzer and detector, which we ignore for this simulation.

We show the theoretical modulation matrix in Eq. (5) rounded to a single decimal place. This true modulation matrix will be used for all wavelengths, field angles, and footprint spatial locations in our simulations to represent a theoretically perfect instrument response. We also show the demodulation matrix ($\mathbf{D}$) rounded to two decimals in Eq. (6) computed using the pseudo-inverse. We note that the modulation efficiency for this scheme is [0.943, 0.566, 0.566, 0.565] for [I,Q,U,V].

1.4 *Fitting Output: Modulation Matrices Using a Calibration Sequence*

Daily polarization calibrations for astronomical instruments are typically performed to derive an accurate modulation matrix for each instrument configuration. Often these procedures simultaneously include fits to several calibration optic parameters using a calibration sequence creating a diverse set of Stokes vectors input to the system. Examples of this process we call PolCal for DKIST are in H21.[68] Derivation of an instrument modulation matrix involves multivariable fits to at least one PolCal data set where a PolCal comprises modulated flux measurements for all the input calibration states. We outline the variables used in our nominal simulation in Table 2. We note that we assess several separate algorithms that fit or ignore several variables detailed in Appendix B.

We can fit variables (or use database values) for the transmission of the calibration polarizer (t_{pol}) and calibration retarder (t_{ret}). The nominal procedure tested here is to fit for the transmission of the two polarization calibration optics, three elliptical parameters for the calibration retarder, and a full instrument modulation matrix. Most astronomical instruments use anywhere from 4 to >10 modulation states giving a range of modulation matrix elements from 16 to over

Table 2 PolCal fit variables.

Name	Description
t_{pol}	Polarizer transmission
t_{ret}	Retarder transmission
CalRet	3 elliptical retardances
Mod Mat	23 modulation variables

40 variables. For this simulation, we have 24 modulation variables and 5 system variables. In our nominal simulation, we ignore the clear measurements. We use only the 10 input states along with six modulation states for 60 photometric measurements. As the simulation does not include input states with the polarizer out of the beam, any variation from 1 in the modulation matrix normalization is degenerate with the polarizer transmission. We enforce modulation matrix normalization by setting the [0,0] element to 1 for our nominal simulation. We nominally fit 28 variables, 23 for modulation and 5 for the calibration optics at each wavelength (λ) and field angle. Thus, the simulated intensities are on a scale from 0 to 1 with the analyzer transmission assumed to be 100% for the particular linear polarization state incident on the polarized transmission axis. We consider other modulation normalization choices as well as a common technique for mitigating time variable intensity (e.g., atmospheric transmission fluctuations) in simulations ranging from 27 to 36 variables in Appendix B.

1.5 *Assessing Calibration Inaccuracies: the Error Matrix*

$$\Delta\mathbf{S} = \mathbf{S}_{\text{meas}} - \mathbf{S}_{\text{true}}, \tag{7}$$

$$\Delta\mathbf{S} = \mathbf{D}_{\text{fit}}\mathbf{I}_{\text{meas}} - \mathbf{S}_{\text{true}}, \tag{8}$$

$$\Delta\mathbf{S} = \mathbf{D}_{\text{fit}}\mathbf{O}_{\text{true}}\mathbf{S}_{\text{true}} - \mathbf{S}_{\text{true}}, \tag{9}$$

$$\Delta\mathbf{S} = (\mathbf{D}_{\text{fit}}\mathbf{O}_{\text{true}} - \mathbf{1}_{ij})\mathbf{S}_{\text{true}}, \tag{10}$$

$$\Delta\mathbf{S} = \epsilon_{ij}\mathbf{S}_{\text{true}}. \tag{11}$$

We estimate the errors introduced in a measured Stokes vector using an error matrix formalism. We show a 4×4 transfer matrix of errors demonstrating the role of spatial inhomogeneities and beam misalignments in the calibration optics on the calibration scheme. In absolute terms, the errors are quantified as the difference between the calibrated Stokes vector measurement $\mathbf{S}_{\text{meas}}$ and the true incoming Stokes vector $\mathbf{S}_{\text{true}}$ shown in Eq. (7). For our case of a system characterized by and calibrated using the optimal modulation matrix formalism, the measured Stokes vector is the calibrated best fit demodulation matrix ($\mathbf{D}_{\text{fit}}$) multiplied by the measured intensities ($\mathbf{I}_{\text{meas}}$) as shown in Eq. (8). To create an estimate of error, we substitute in the true incoming Stokes vector $\mathbf{S}_{\text{true}}$ multiplied by the true modulation matrix $\mathbf{O}_{\text{true}}$ in place of the measured intensities, as shown in Eq. (9). This simplifies to a single expression multiplying the true incoming Stokes vector in Eq. (10) where $\mathbf{1}_{ij}$ is the identity matrix. We set this expression as the 4×4 error matrix ϵ_{ij} in Eq. (11).

We note that this concept of an error matrix was previously introduced by Elmore on the Advanced Stokes Polarimeter[101] and Ichimoto et al.[102] (I08) on the calibration of the Solar Optical Telescope on board the Hinode spacecraft. However, in those cases, the modulation matrix was not an optimal one from a statistical noise perspective.[92] This led to the use of a polarization response matrix (X_{ij}), which described how a measured Stokes vector related to the true incident Stokes vector with terms far away from the identity matrix. This response matrix is still computed as the demodulation matrix (D_{ij}) multiplied by the modulation matrix (O_{ij}) but

now using a demodulation matrix with elements potentially far away from optimal. In the case of Hinode, the demodulation matrix elements were all assigned to be ± 1 instead of the optimal floating point numbers due to other constraints. Terms of ~ 0.5 are seen in the Hinode response matrix.[102] The error matrix in this case was not given by $(\mathbf{D}_{\text{fit}}\mathbf{O}_{\text{true}} - \mathbf{1}_{ij})$ but instead is given by the difference from identity for the product of the calibrated best fit response matrix and the true response matrix $(\mathbf{X}_{\text{fit}}^{-1}\mathbf{X}_{\text{true}} - \mathbf{1}_{ij})$:

$$\epsilon_{ij} = 10^{-2}\begin{pmatrix} 1 & 1 & 1 & 1 \\ 0.05 & 1 & 0.5 & 0.5 \\ 0.05 & 0.5 & 1 & 0.5 \\ 0.05 & 0.5 & 0.5 & 1 \end{pmatrix}. \tag{12}$$

For DKIST, a nominal generic specification for these error limits is shown in Eq. (12). We followed a similar approach to Hinode in I08.[102] We assume the maximum incoming linear and circular polarization signals have 10% magnitudes, and we assume limits on depolarization at 1% and on polarizance from I to QUV of 0.05%. This gives the first row and the diagonal of Eq. (12) all having errors of 1%. The QUV to I terms are all 0.05%. The off-diagonal rotation submatrix terms are 0.5%. Actual error matrix limits will depend on the particular science use case, observing strategy, weather, wavelengths, and a very long list of instrument performance parameters. In general, concerns about the continuum polarization stability, depolarization, and retardance can be specified considering constraints on the length, zero point, and orientation of the reconstructed Stokes vectors.

2 Measuring Polarizer Spatial and Spectral Properties

Astronomical calibration polarizers must have a known orientation with minimal variation across the aperture to create a high quality reference beam. Wire grid polarizers are common for use at astronomical telescopes, and their heat tolerance makes them quite favorable for solar telescopes. As manufacturing techniques improve, high contrast, broad band transmission, and uniform orientation of extinction are achievable. Most telescopes require calibration as far up stream in the beam as possible, usually requiring mounting away from a pupil plane, often near focal planes. Spatial variation of polarizer properties mounted near focus impacts calibrations across the field of view as well as coupling in mounting decenter and beam footprint size impacts with inhomogeneous polarizer performance. We outlined in the introduction several optomechanical issues specific to DKIST but generally applicable to telescopes mounting polarizers near focal planes in an active, articulated optics system. Spatial variation of polarizer properties mounted near focus impacts calibrations across the field of view. The induced errors are sensitive to both the beam footprint size relative to the spatial variations as well as the decenter of the footprints from the optical rotation axis.

We performed extensive spatial mapping of polarizer transmission, contrast, and orientation of maximum extinction to ensure that the DKIST calibration polarizers were high quality reference optics. Transmission spatial variation is very significant at magnitudes of a few percent. The orientation for maximum extinction does also vary as functions of aperture and wavelength but at magnitudes below $\pm 0.05°$. We find we achieve contrast in the 1000 to $>50,000$ range for a pair of polarizers depending on wavelength, polarizer fabrication type, and coating. Spatial variation of contrast can be severe, often a factor of few to as high as a factor of 6. However, as noted in Ref. 15, propagation through a DKIST calibration retarder can also induce $\sim 0.5\%$ depolarization. The polarizer contrast should not be the largest error in a typical polarization calibration when depolarizing terms are ignored, including those caused by nonuniform retarders in noncollimated beams, nonuniform coated optics, and powered mirrors (e.g., HS17[61]). We show some examples of contrast, extinction, Mueller matrix elements, and the degree of polarization (DoP) in Appendix E. All these polarizer imperfections must be considered in calibration of any telescope on the common assumption that the polarizer defines +Q.

2.1 *DKIST Calibration, Test and Spare Large Aperture Polarizers*

DKIST has procured several Moxtek wire grid polarizers for use in the telescope calibration. We also procured a number of test polarizers and associated small test polarizers cut from the same wafer. The DKIST nominal calibration polarizer named CalPol1 is a UVT-240A type Moxtek wire grid with 100-nm wire pitch on an Ohara SK-1300 fused silica wafer. Wire heights are near 200 nm with a few nm etched into the substrate, a 55-nm wire width, and a 45-nm space between adjacent wires. For longevity and improved thermal performance, Moxtek applied a 3.8-nm thickness conformal Al_2O_3 protective coating over the wire grid. The back surface is uncoated. We note that for common multilayer coatings, the reflectivity can be much worse than the uncoated substrate at wavelengths outside the control bandpass. As we operate from 380 to 5000 nm in a harsh environment, we did not pursue back side coatings. The CalPol Spare is a replica of the 120-mm-diameter UVT-240A wire grid polarizer on a fused silica substrate including the conformal Al_2O_3 protective coating procured months later from a different run. This optic was used extensively in lab testing of the Cryo-NIRSP and DL-NIRSP instruments in place of a modulator. This spare was mounted in DKIST as of January 2020. Another UVT-240A wire grid was fabricated as our master polarizer is mounted one level above all DKIST calibration polarizers. This optic mount includes three laser tracker nests and was tested in the Boulder laboratory for alignment of the polarizer wire extinction orientation against known optical and mechanical references. See H21[68] for details.

We selected and worked with Moxtek to develop a crystal sapphire substrate wire grid polarizer. This substrate was chosen as it accommodates our 380- to 4600-nm wavelength range, minimizes substrate absorption, and has a thermal conductivity roughly 20 times higher than fused silica (27 versus 1.4 W/m/K). Both A- and C-plane cut wafers were tested with aluminum wire structure heights around 170 to 200 nm. Our final choice for large area polarizers was a 0.7-mm-thick C-plane cut sapphire wafer. The coating absorption estimated as the losses not attributable to S&P transmission or reflection were in the range of 12% to 16% per the Moxtek preliminary metrology on the test wafer for wavelengths between 380 and 900 nm. We did extensive testing on a preliminary Sapphire Test optic along with thermal testing deployed in the 300-W DKIST beam. Moxtek made improvements to their nanoimprint lithography (NIL) fabrication process. We received and tested the sapphire CalPol, which achieved the expected uniformity improvements from the sapphire test polarizer. The substrate back surfaces are also uncoated.

We finally compare the spatial and spectral metrology with two Moxtek ultra broad-band (UBB) wire grids at 150-mm diameter (UBB-01A) mounted inside the Cryo-NIRSP instrument filter wheel for internal instrument calibrations. These wire grid polarizers have a wider wire spacing (120 nm) but the same Ohara-fused silica substrate. We denote these two polarizers CN Inst Pol 1 and CN Inst Pol 2.

Table 3 shows the large area polarizers we have mapped spatially and spectrally. The first column names the polarizer (name). The second column lists the process type. The third column lists the substrate wafer material as either fused silica from Ohara or the crystal sapphire wafers.

Table 3 DKIST calibration polarizers: substrates, wires, and coating optical properties.

Name	Type	Substrate	Pitch (nm)	Coat	Diam. (nm)	Meas
CalPol 1	UVT-240A	Ohara SK-1300	100	Al_2O_3	120	bEVO
CalPol Spare	UVT-240A	Ohara SK-1300	100	Al_2O_3	120	mCCD, mDEVO
Master Pol	UVT-240A	Ohara SK-1300	100	Al_2O_3	120	bEVO, mCCD
Sapphire CalPol	NIL	C-plane Sapphire	90	Al_2O_3	120	mDEVO
Sapphire Test	NIL	C-plane Sapphire	90	Al_2O_3	120	mCCD, mDEVO
CN Inst Pol 1	UBB-01A	Ohara SK-1300	120	None	152	mDEVO, mCCD
CN Inst Pol 2	UBB-01A	Ohara SK-1300	120	None	152	mDEVO, mCCD

The fourth column lists the pitch between wires for the manufacturing process. The fifth column lists the presence and type of wire protective coating. The sixth column lists the diameter (diam.) of the polarizer cut for DKIST. In the sixth column, we list the lab spectrograph setup used for measurements presented here. We have multiple fiber-fed USB spectrographs in multiple locations. We denote b for Boulder labs and m for Maui labs. The Avantes CCD-based spectrograph systems are called out as CCD. Our Boulder lab setup also has infrared capability from 0.9 to 1.7 μm wavelengths using an Avantes AvaSpec-NIR512-1.7TEC. We call out the higher spectral resolving power Avantes AvaSpec-ULS4096CL-EVO system with a CMOS sensor at 4096 pixels in our Boulder lab as bEVO. We call out a more recent dual spectrograph Maui-based setup with two separate AvaSpec-ULS4096CL-EVO systems in a single enclosure (for 8192 pixels total) as mDEVO (Maui, Dual-EVO).

2.2 *DKIST Calibration Polarizer: CalPol1 Spare*

We performed thermal testing with the DKIST observing the sun in January 2020. During this campaign, we had decided to mount the polarizer called the CalPol1 Spare in the telescope as the lab metrology was more thorough and this polarizer was deemed to be slightly more uniform spatially. This polarizer has been in use on the telescope since that installation.

Spatial mapping of the spare calibration polarizer (CalPol1 Spare) in the lab prior to mounting in the telescope shows that we achieve contrast ratios in the 1000 to 40,000 range with orientation of maximum extinction variation below ± 0.03 deg both spatially and spectrally. This is the combined contrast of two wire grid polarizers, one being the fixed Moxtek analyzer. The part was mounted with the wires facing away from the incoming test beam, the same as the mounting orientation within DKIST. This setup represents a wires-in configuration against the lab analyzer. We used a 1.5-mm-diameter mask attached to the lens tube holding the collimating lens on the collimated beam side to size the probe beam.

2.2.1 *CalPol1 spare: contrast and extinction orientation spectra*

The contrast data set spatial sampling pattern used a 3-mm radial step and 60-deg angular sampling in a Rosette pattern for the first annulus decreasing as x^{-1} to the last radius of 54 mm. We recorded 1027 individual spectra across the aperture for each map. We repeated these measurements for a nonuniform set of 13 analyzer angles ranging by 3.2 deg to separate extinction ratio from the orientation of the polarization axis spatially varying across the aperture. This spatial and temporal sampling allows a simultaneous fit to the best-fit crossed orientation for the analyzer (θ_0), the flux transmitted at this best-fit crossed orientation (C), and the intensity amplitude (I_0) for the nominal $\cos^2$ function for rotating polarizer pairs. The model fit is $I = I_0 \cos^2(\theta - \theta_0) + C$. The contrast ratio is typically defined as the ratio of transmission through parallel and perpendicular polarizers, computed as $(I_0 + \mathrm{C})/\mathrm{C}$. The orientation for maximum extinction is θ_0.

Note that the spatial mapping scripts were modified to record lamp flux calibrations with no sample in the beam at a user-specified cadence usually selected between 2 and 10 min. The Avantes CCD system used for this test had significant electronic problems with temporal drifts in background offset levels as well as in system gains. Some spectral pixels also had significantly corrupt data, which we filter and reject using the 13 separate angles and a global fit to the rotating polarizer model. We performed the model fitting after the individual spectra are normalized by a linear interpolation of the two adjacent lamp calibration spectra. The model fit is assisted by initial solution guesses estimated using the minimum detected flux ratio and the amplitude estimated from the edge points.

The contrast and orientation of maximum extinction is shown in Fig. 1 after a 16× binning in wavelength. Spatial variation of contrast is shown Fig. 1(a) along the maximum extinction orientation. Figure 1(b) shows the orientation of maximum contrast at every spatial location. There is significant spatial variation detected at amplitudes of 0.05 deg along with some significant wavelength-dependent behavior. The solid blue curve shows the median orientation across the aperture at every wavelength.

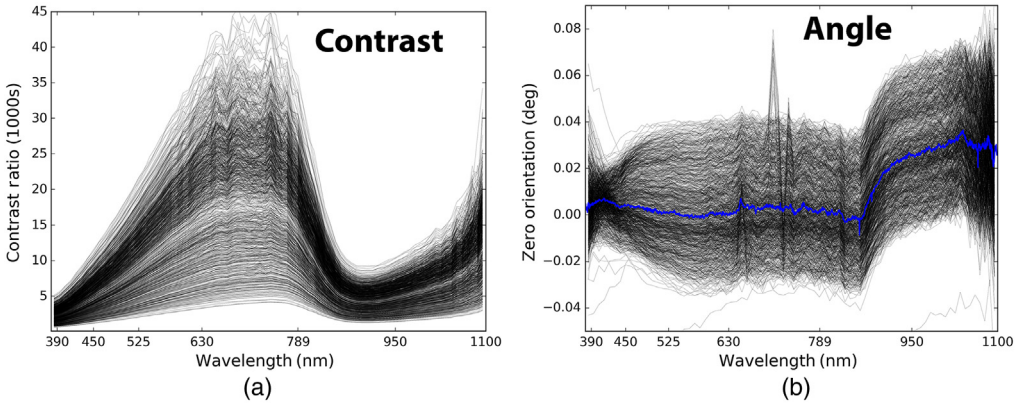

Fig. 1 (a) The contrast ratio at all 1027 spatial locations derived from the fit to the spatial maps at the 13 analyzer orientations. (b) The analyzing polarizer orientation for maximum extinction for all 1027 spatial locations.

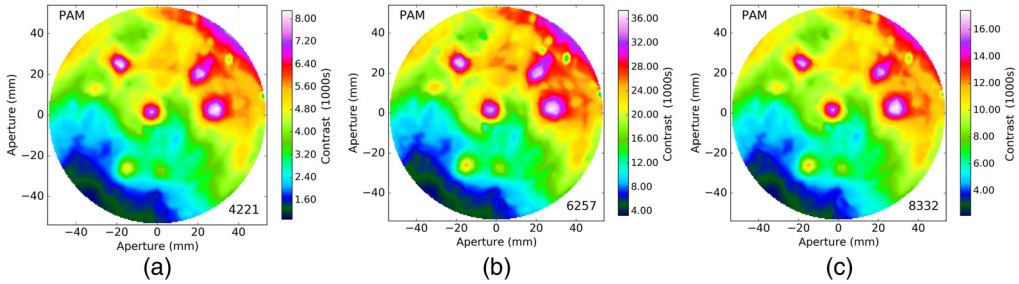

Fig. 2 The contrast spatial maps at maximum extinction orientation reconstructed from model fitting of 1027 spatial spectra at 13 separate analyzer orientations from January 27th with 1.5 mm spatial masking and 3 mm radial steps. Wavelengths shown are (a) 422.1 nm, (b) 625.7 nm, and (c) 833.2 nm. We note the CalPol1 Spare was also used in instrument functional testing as a polarizer-as-modulator (PAM).

2.2.2 *CalPol1 spare: mapping contrast variation across the aperture*

The spatial variation of contrast of CalPol1 Spare against the analyzer is shown in Fig. 2. Several roughly circular features of relatively high contrast are seen. We note that these features are also visible in scattered light under a visual inspection using high powered lighting. The nonuniform dots are sometimes seen in the UV-240 product. This comes from lift pins in the interference lithography process equipment, and the UV240 process is particularly susceptible to temperature changes around those lift pins. Wavelengths shown are 422.1 nm in Fig. 2(a), 625.7 nm in Fig. 2(b), and 833.2 nm in Fig. 2(c) chosen to span the VIS to NIR wavelength range.

2.2.3 *CalPol1 spare: mapping extinction orientation variation across the aperture*

The spatial variation of the orientation for maximum extinction is shown in Fig. 3. Wavelengths shown are 422.1 nm in Fig. 3(a), 625.7 nm in Fig. 3(b), and 833.2 nm in Fig. 3(c). The small circular features in contrast are not present. The spatial variation shows <0.05 deg orientation variation across the aperture with a linear change from left to right as the dominant feature. As shown in Fig. 1, the spatial variation is relatively constant for wavelengths in the range 480 to 1100 nm with some reduction in spatial variation at shorter wavelengths.

We note that this angular variation for the maximum extinction orientation is very small (<0.05 deg). This creates a negligible impact on the independent measurement of contrast and transmission spatial variation. For instance, the contrast ratio results of single map at a single

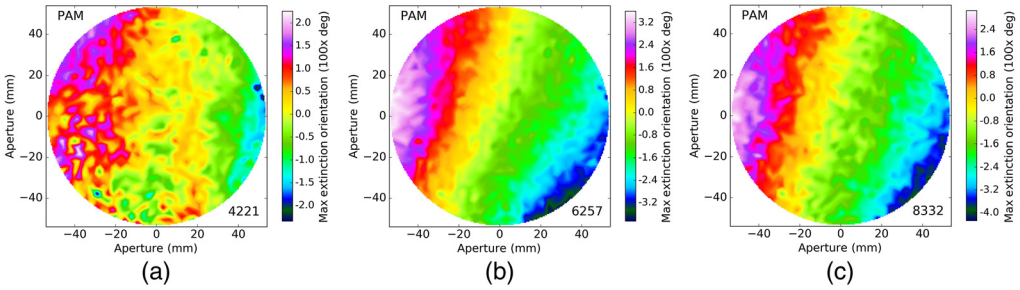

Fig. 3 The orientation of maximum extinction reconstructed from model fitting of 1027 spatial spectra at 13 separate analyzer orientations from January 27th with 1.5 mm spatial masking and 3 mm radial steps. The orientation has been multiplied by 100 for clarity. Variation ranges by less than ± 0.05 deg. Wavelengths shown are (a) 422.1 nm, (b) 625.7 nm, and (c) 833.2 nm. We note the CalPol1 Spare was also used in instrument functional testing as a PAM.

analyzer orientation within ± 0.5 deg of the maximum extinction orientation are very similar in both spatial behavior and contrast magnitude to Fig. 2. A simultaneous fit to 13 maps at variable analyzer orientation gives essentially identical contrast and transmission results to a single map at the appropriate orientation.

2.2.4 *CalPol1 spare: transmission spectra*

We collected the transmission through parallel polarizers using the aperture averaged orientation for maximum extinction. We created four repeated data sets with spatial sampling pattern having a 1.5-mm radial step and 60-deg angular sampling for the first annulus decreasing as x^{-1} to the last radius of 54 mm. We record 3997 individual spectra across the aperture with a duration of 2.0 s per step and 131 min total per map. The four repeat maps represent 16,000 individual spectra. An additional single transmission map used a 1.0-mm radial sampling out to a maximum radius of 54 mm for 8911 individual spectra across the aperture. We show the 3997 individual transmission spectra recorded across the aperture in Fig. 4. The electronic issues with the CCD sensor caused small erratic spectral behavior seen in the 600- to 850-nm bandpass. A few spectra show transmission losses several percent below the majority of the spatial points clustered within roughly $\pm 1\%$ of the aperture average.

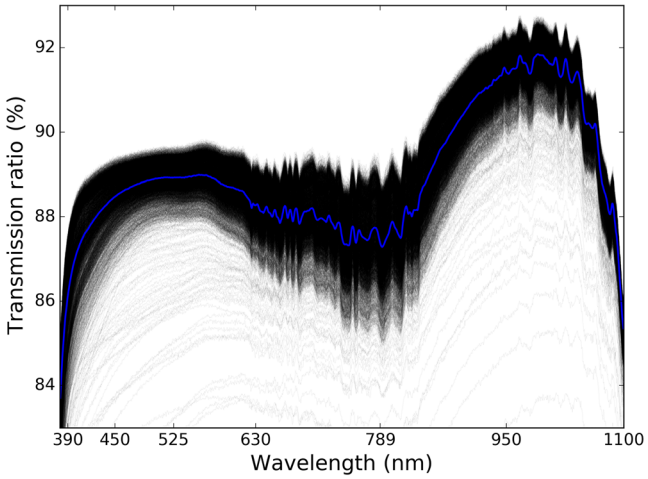

Fig. 4 The transmission spectra for CalPol1 Spare at each of the 3997 spatial locations after median-combining the four repeated spatial maps. Blue shows the aperture median transmission spectrum.

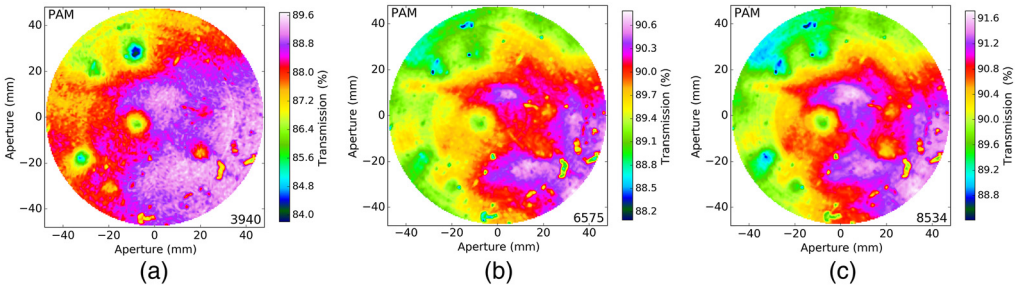

Fig. 5 The transmission spatial maps with a parallel analyzer derived from median combining four separate spatial maps with 12,481 spatial spectra each from February 17th with 1.5 mm spatial masking and 0.75 mm radial steps. Wavelengths shown are (a) 394.0 nm, (b) 657.5 nm, and (c) 853.4 nm. The 9.5-min cadence lamp temporal drift correction has been applied. We note the CalPol1 Spare was also used in instrument functional testing as a PAM.

2.2.5 *CalPol1 spare: mapping transmission across the aperture*

We show the spatial maps derived using the 1.5-mm-diameter beam footprint spectra in Fig. 5. The orientation is different than the contrast maps in Secs. 2.2.2 and 2.2.3. The optic was also freshly cleaned using compressed air though a few small dust spects remain as obvious and significant transmission losses. We average spectrally by factor of several spectral pixels to remove the spectral fringes and their associated spatial variation detailed below. A $\pm 0.5\%$ spatial fringe contribution is present in single specctral bin maps of a few percent spatial variation in transmission.

3 Measuring Retarder Spatial and Spectral Properties

There are several DKIST calibration retarders mounted in the GOS. For this simulation, we focus on the OCcal retarder. This retarder was fabricated without any refractive index matching oils, with improved spectral clocking alignment between crystals, with many-layer fringe mitigating coatings, and improved spatial uniformity through deterministic fluid jet polishing. We described the preliminary retardance in H20.[86]

3.1 *Optically Contacted Calibration Retarder: Elliptical Retardance*

We presented spatial maps of retardance and spectral oscillations for the OCcal in H20[86] and will not add any new metrology. We will continue to include the spatial and spectral variation of the three components of elliptical retardance in our simulations, as we did in HS18a.[63] We note that we have improved our data analysis algorithms to use independent exposures of the lab light source recorded without the sample optic under test for every spatial step of the maps. The data sets presented in H20[86] were reprocessed using these new algorithms. The retardance properties did not change significantly. However, using the lamp spectral calibrations recorded on every data set ($\sim$12 min cadence), we were able to provide retarder transmission measurements with much better temporal stability. We note that multiple spatial maps were recorded taking over 6 days each where drifts in lamp brightness would corrupt transmission measurements. In one case, a bulb was replaced and subsequently changed brightness by over 10% in the course of a 6-day mapping data set. The new data processing removes artifacts in transmission spatial variation to levels of a few parts in 10,000 without impacting the derived retardance.

3.2 *Optically Contacted Calibration Retarder Transmission*

Spatial variation of transmission is also a concern through our 120-mm-diameter coated optics. Additional complications come from optical contact bonds being imperfect with trapped dust particles, air, and areas of noncontact. Coatings typically have some spatial variation over larger optic diameters (see H19[67] for FIDO dichroics). We show in Fig. 6 example defects near the edge of the clear aperture for our OCcal retarder. In Fig. 6(b), we show the transmission of the optically contacted part in the clear aperture as well as within certain noncontact defect regions.

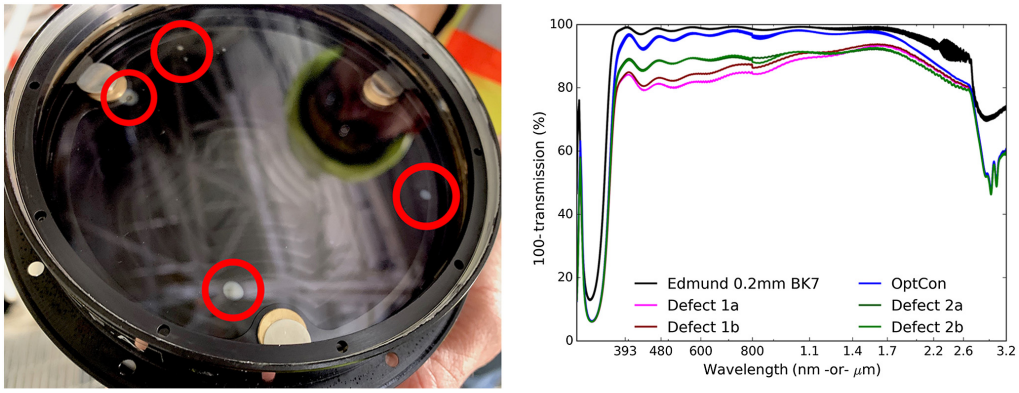

(a) (b)

Fig. 6 The transmission of the coated, optically contacted quartz compound retarder as measured in the MLO Cary. (b) The transmission scans including an Edmunds ultrathin BK7 coating witness sample in black, the OCcal aperture center in blue, and several defects in other colors. (a) A picture of the optic during on-summit installation. Red circles highlight patches of noncontact. We note the noncontact patch shrank significantly after thermal cycling and even more during shipping, lab testing, and summit install.

In Fig. 6(a), we show spatial regions of noncontact as the light-colored patches inside red circles drawn to highlight the aperture defects. There is a special black anodized holding tool with small metal disks seen behind the optic just inside the aperture. The larger region in the lower left was originally elliptical at 15 mm on the long axis but has shrank with time to ∼5 mm in the image. The smaller defect in the upper left is roughly circular at 5 mm diameter with a trapped dust spec creating an air gap of a few waves thickness, enough to create color and intensity rings seen in the image.

The MLO Cary transmission scans are done with the beam nominally centered on the noncontact region and then adjacent to the noncontact region. We note that during thermal chamber testing of the optical contact bond, these defects shrank significantly. The defects shrank further during shipping, lab testing, and storage on the summit before installation. The lab-derived transmission maps use a 3.5-mm diameter beam, which clearly sees large changes from the noncontact patch and trapped dust defects. Figure 7 shows the unpolarized transmission for the

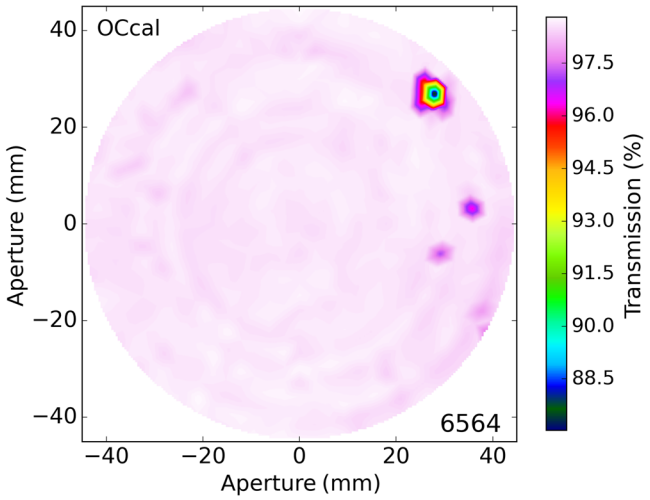

Fig. 7 The transmission measured across a 90-mm aperture for the OCcal. Colors for transmission include a wide range from 87% to 98% highlighting one large trapped dust spec creating a >10% transmission loss near the edge of the aperture as well as a few other smaller defects. Ring-shaped artifacts at scales of ±0.0025% show measurement noise limits with no significant variation detected in coating or crystal transmission.

OCcal at a wavelength of 656.4 nm derived from the [0,0] element of the Mueller matrix measured with our Boulder-based lab metrology system. We show the full scale of transmission variation showing ~10% losses in the noncontact patch. We note that errors on intensity scales of ±0.0025% in ring shapes are our current measurement systematic error limit. There are no substantial spatial patterns outside a few small trapped dust particles. The scratch dig and coating uniformity specifications nominally would preclude variations that would create a photometric error detectable above statistical noise limits within a beam footprint.

4 Footprints on the DKIST Calibration Optics

The beam footprint on the GOS calibration optics is a moderate function of the distance away from the Gregorian focus. Level 3 is 550 mm above Gregorian focus where the master polarizer is mounted. The beam footprint for a single field angle is 42.1 mm diameter with the full 5.0-arcmin field illuminating a 110.5-mm aperture. Level 2 is 450 mm above Gregorian focus where the suite of calibration polarizers are mounted. The single field footprint is 34.5 mm in diameter with a 104.3-mm illuminated aperture at full field. Level 1 is 350 mm above Gregorian focus where the suite of calibration retarders are mounted. The single field footprint diameter is 26.8 mm with a 98.4-mm illuminated aperture. We collect the footprint information for the calibration optics in Table 4. The optic name is in the first column. The distance ahead of Gregorian focus is listed in the second column. The beam footprint diameter for any single field angle is shown in the third column (footprint). We collect the beam decenter for a 1.4-arcmin field angle in the fourth column and for a 2.5-arcmin field angle in the fifth column with the decenter increasing away from the pupil toward the focal plane. The final sixth column shows the illuminated aperture. We show more details on the optical beam footprints and spatial variation impacts in Appendix A.

The optics spin through a nonuniform calibration sequence such as Table 1 during calibration. The area of the optic sampled changes as a function of field angle, decentering the beam. Figure 8 shows examples of the footprints for a +1.4-arcmin field angle when the calibration retarder is spun through the unique polarizer angles of 0 deg, 45 deg, 60 deg, and 120 deg of the 10 state sequence in Table 1. We note that 8 of 10 states use only the 0-deg and 45-deg polarizer orientations providing a strong weighting of polarizer aperture nonuniformities to that particular arc of the optic. To compute the polarization calibration optic properties, we extract the metrology information from the appropriate footprint as in Fig. 8.

We include a 2.5-mm spatial misalignment of the GOS optics to simulate the measured decenter from preliminary alignment during the commissioning phase. This can and should be improved later. We include the offset to represent the early DKIST commissioning phase calibrations and show an example of how optical misalignments can create errors that limit the calibrations on the beam bore sight.

We note that there is much choice in optimizing the calibration efficiency of a sequence, the number of states in that sequence, and the starting orientation of the calibration optics. The trade offs are substantial. We leave questions about optimizing the starting optic orientation and number of states in the presence of spatial variation for later. We showed in HS18b[66] that substantial broad-band calibration efficiency optimization is possible with the number of input states and starting optic orientations. Additional complication comes from the nonzero delay times in instrument response causing thermal drifts.

Table 4 Footprints, decenters, and apertures.

Name	Distance (mm)	Footprint (mm)	1.4′ DeCn (mm)	2.5′ DeCn (mm)	Aperture (mm)
MasterPol	550	42.1	19.5	34.9	110.5
Cal. Pol	450	34.5	19.9	35.4	104.3
Cal. Ret	350	26.8	20.2	36.0	98.4

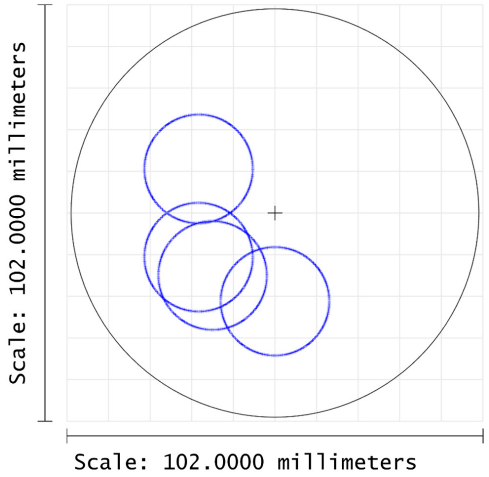

Fig. 8 The footprints for a beam on the calibration polarizer as the optic spins through unique polarizer angles of 0 deg, 45 deg, 60 deg, and 120 deg at +1.4-arcmin field angle. We note that for our 10 state calibration sequence, four of the polarizer states are at 0 deg and four more states are at 45 deg.

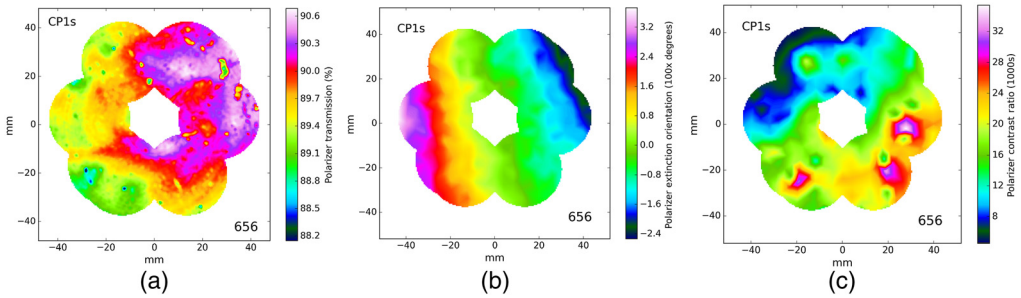

Fig. 9 The properties within individual footprints for the beam on the calibration polarizer while spinning through the 10 state calibration sequence at a wavelength of 656 nm and field angle of ±114 arc sec. (a) The contrast ratio, (b) the orientation of maximum extinction, and (c) the transmission. The angles for the polarizer in the 10-state sequence include 0 deg, 45 deg, 60 deg, 120 deg with four of the states at 0 deg, and four of the states at 45 deg.

4.1 *Polarizer Spatial Variation Sampled by Beam Footprint*

We show examples of the footprint for the beam on the calibration polarizer in Fig. 9 for the combined orientations in the 10 state calibration sequence. We included the current ∼2.5 mm decenter of the GOS to show the magnitude of errors near the optical system bore sight. Footprint optical properties have been extracted from the metrology in the appropriate spatial region of the optic following Fig. 8 appropriate to each field angle. Positive and negative field angles are now not symmetric about the center of the optic due to the modeled 2.5-mm GOS misalignment.

4.2 *Retarder Spatial Variation Sampled by Beam Footprint*

We show examples of the footprint for the beam on the calibration retarder in Fig. 10 for the combined orientations in the 10 state calibration sequence at 630 nm wavelength. As the optic rotates through many different angles, the decentered beam samples different spatial regions, giving rise to variable retarder properties for each input state. As the field angle increases, the beam decenter increases sampling a larger and larger annulus on the retarder from left to right in the graphics. We have included the current ∼2.5 mm decenter of the GOS to show the magnitude of errors near the optical system bore sight. We do not show the fast axis of linear retardance as the behavior is similar to other retardance terms.

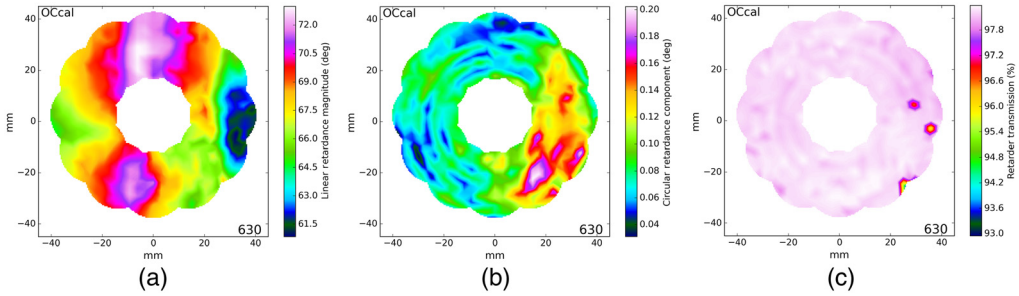

Fig. 10 The properties within footprints for a beam on the OCcal as the optic spins through the 10 state calibration sequence. (c) Retarder transmission. (b) The circular retardance magnitude. (a) The linear retardance magnitude. The unique angles for the retarder in our 10-state sequence include 0 deg, 30 deg, 60 deg, 90 deg, 120 deg, and 150 deg. We note the fast axis variation is included in the simulations but not plotted here.

4.3 *Modulated Intensities Across Footprint*

We propagate intensities through the calibration optics, ideal modulator, ideal analyzer, and detector to simulate intensity during the calibration process. We interpolate the Mueller matrix from the metrology for each calibration optic onto a common spatial grid across the beam footprint to ensure uniform sampling.

We use the appropriate Mueller matrix from each footprint spatial position for each field angle at each step of the calibration sequence at each wavelength. The unpolarized input Stokes vector simulates a calibration using continuum (line-free) wavelengths observing solar disk center. Flux is propagated through the sequence of calibration optics and also the modulation sequence to provide the simulated intensity transmitted through the entire system. The simulation begins with the imperfect calibration polarizer and ends after the analyzer on the ideal sensor. Figure 11 shows intensity variation across a few select footprints when using our ideal modulator and our 10 state calibration sequence for a wavelength of 630 nm at a field angle of $+114$ arc sec. Other modulation states have the same general spatial variation characteristics. Intensity variation levels are roughly 1% to 2% in line with the polarizer and retarder transmission variation combined with the retardance spatial nonuniformity.

The field-dependent variation of <2% intensity is a small fraction of the modulated intensity. Figure 12(a) shows modulated intensities as a function of the 10 state calibration sequence step for 630 nm wavelength covering the full ± 1.9 arc min field of view. Each footprint spatial location was graphed as a separate thin line of the appropriate modulation state color. The footprint

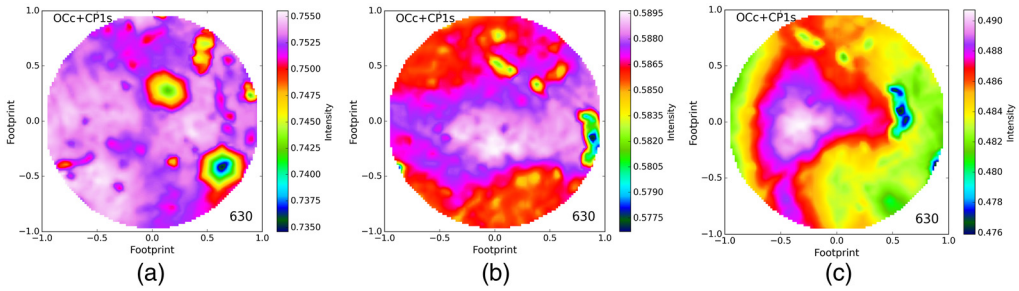

Fig. 11 The intensity variation within individual footprints for the beam when calibrating a +1.9-arcmin field angle at a wavelength of 630 nm. (a) Input state 3 where both polarizer and retarder are in the beam including a large optical contact transmission defect in the retarder. (b) An input state with only the polarizer. (c) Another state with both retarder and polarizer in the beam where small structures are seen contributing from the high spatial resolution polarizer metrology but also some substantial retardance spatial variation at larger spatial scales. We selected modulation states of 0, 0, and 2 from left to right to demonstrate dissimilar spatial behavior. All other modulation states have similar spatial morphologies to these.

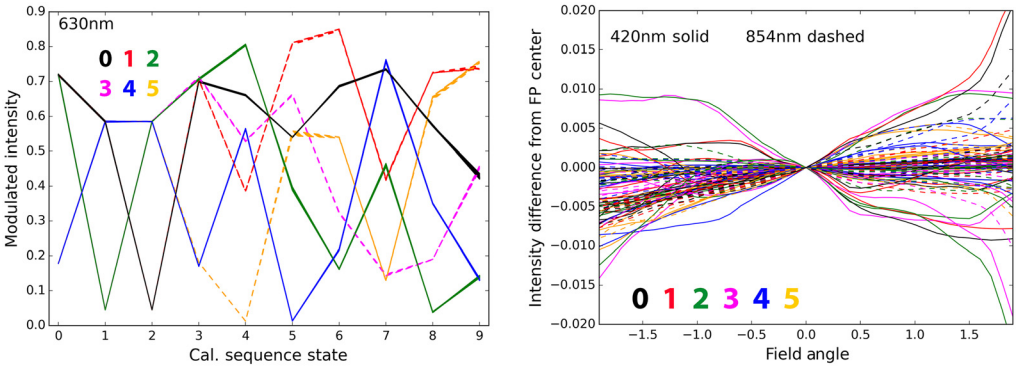

Fig. 12 (a) The intensities for 6 state modulation with the 10 state calibration sequence at all simulated field angles after averaging intensity across each beam footprint for a wavelength of 630 nm. Each color shows a different modulation state. Multiple thin lines are used to plot intensities at different spatial locations giving rise to the line thickness variation for each color. The modulation matrix symmetry gives nearly identical intensities for the first three input states using only the polarizer. (b) The change from aperture median intensity as a function of field angle at two wavelengths. Each of the six modulation states is now plotted using the same line color scheme giving rise to multiple lines for each modulation state color. Solid lines show 420 nm while dashed lines show 854 nm. We leave the intensities referenced to the unpolarized input at 1.

spatial variation can be seen as some colored lines becoming slightly more or less thick for certain calibration and modulation states.

We simulate the calibration process by averaging the detected intensity across the beam footprint as an approximation of an ideal detector recording the average intensity. Figure 12(b) shows the variation in aperture average intensity as a function of field angle for each of the six modulation states for each of the 10 calibration inputs. Multiple wavelengths are plotted to show diversity in errors for each modulation state (color). We note that the polarizer and retarder transmission spatial variation are the larger terms in this simulation. Though we have previously shown the impact of retardance spatial uniformity, which falls roughly proportional to wavelength, in this simulation most wavelengths show similar errors as the transmission uniformity is not a very strong function of wavelength. For more detail on the beam footprint variations see Appendix A.

5 Fitting Footprint-Averaged Model Across Field

We have created simulated intensities averaged over the beam footprint as a function of field angle, wavelength, calibration state, and modulation state. At each field angle and each wavelength, we can now fit our system model for calibration parameters and modulation matrices to this synthetic data set. Our nominal model is to fit two calibrator transmissions and three elliptical retardances, along with the 23 modulation matrix elements per Table 2. We note that we enforced intensity normalization of the modulation matrix by setting the [0,0] element to 1 and thus loose one variable. We have not included separate modulated intensity measurements (clears) with the polarizer out of the beam in our simulated data set. Thus, the polarizer transmission is degenerate with any transmission scaling of the modulation matrix. We show details and alternate fitting algorithms in Appendix B. We include optional fits to optic transmission separately for each input Stokes vector (similar to I08). We also compare the modulation matrix intensity normalization by the maximum I modulation element to enforce all elements in the first column (I modulation) being less than or equal to 1. See Appendix B for details.

We nominally fit each field angle separately at each wavelength as most astronomical instruments can record data of sufficient signal-to-noise ratio (SNR). We reduce photometric errors by doing the field-dependent fit, but this introduces systematic errors, skewing to the fit parameters. This introduces calibration inaccuracy through the modulation matrix best fit values not reflecting the true values. The fitting algorithms generally try to reproduce the measured intensities, but

for calibration purposes, the ultimate output goal is to have the most accurate demodulation matrix. There are many trade offs to consider when choosing a calibration sequence. More input states covering a variety of angles can reduce some of these field-dependent calibration artifacts, but make temporal and thermal issues worse. A detailed trade study is beyond the scope of this paper, but we present here a method for doing such a trade in Appendix B.

5.1 *Fitted Calibrator Transmission Variable Field Dependence*

Transmission for the polarizer, transmission for the retarder, and the three elliptical retardance values all vary as a function of wavelength and field angle after performing fits on the footprint-averaged intensities. We highlight the transmission variation as the larger factors. Figure 13 shows the variation of these best transmission fit values changing as a function of field angle. The polarizer transmission varies by up to 0.5% with field though the footprints presented above show variation a factor of a few larger. Similarly, the fitted retarder transmission varies by up to 0.35% with substantially more variation seen in the footprints. See Appendix B.7 for some additional details. Appendices B.6 and B.7 outline field and wavelength dependence, respectively.

5.2 *Error Matrix with Field Angle*

We can define an effective field angle within which the calibration inaccuracies stay below certain thresholds. We showed in HS17[61] how the mirror coating behavior with incidence angle created field-dependent polarization errors. We can now add to this the field angle and wavelength dependence of the inaccuracies caused by the calibration process. The error matrix elements show how errors in the demodulated Stokes vectors grow as a function of field angle and wavelength. Figure 14 shows the error matrix variation with field angle for two distinct wavelengths: 420 and 854 nm. As we included the ∼2.5-mm decenter of the calibration optics, these terms do not go to zero for the optical bore sight. With the DKIST beam without ao stabilized to roughly ±9.7-arc sec field angle on the coudé laboratory, we expect some mild field dependence. See Appendix B.12 for some error matrix details at small field angles.

5.3 *Error Matrix with Wavelength at 60 and 114 ArcSec Field Angles*

Figure 15 shows the error matrix variation with wavelength. Figure 15(a) shows a 60-arcsec field angle whereas Fig. 15(b) shows a 114-arcsec field angle. No clear large trend is obvious with wavelength. A few terms drop strongly toward longer wavelengths but several other terms stay constant or even increase toward long wavelengths. As we showed previously in HS18b[66] and H20,[86] retarder spatial variation leads to errors that decrease as λ^{-1}. However, the polarizer transmission has a spatial scale similar to the beam footprints with inhomogeneity throughout the

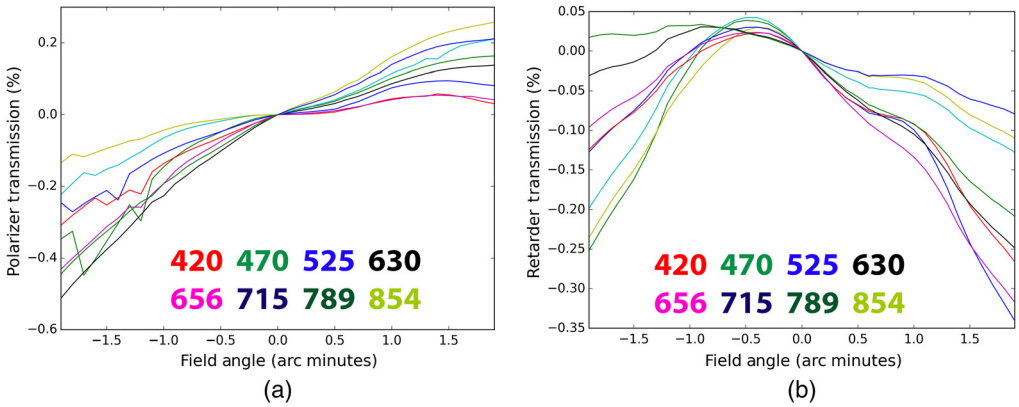

Fig. 13 (a) Transmission changes for the polarizer from field center as a function of field angle. (b) Retarder transmission. Each wavelength is plotted as a separate color for both transmission graphics.

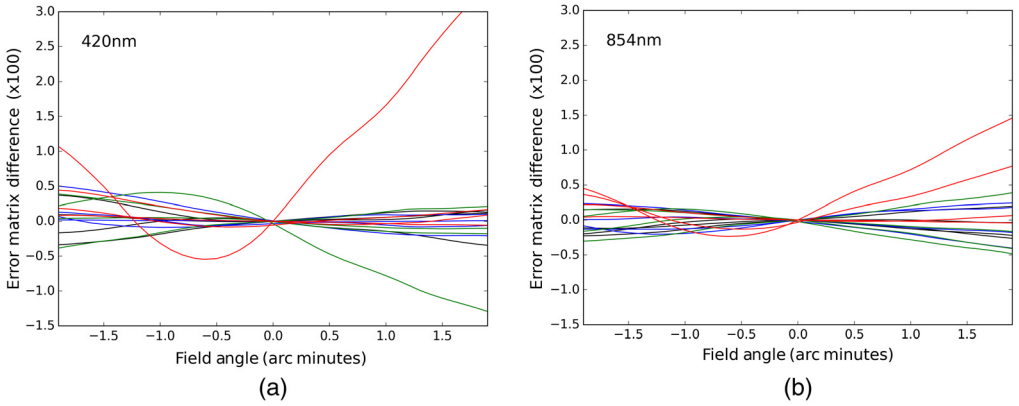

Fig. 14 The error matrix elements across the field of view multiplied by 100. Each color shows a different Stokes parameter with four matrix elements per Stokes parameter. (a) 420 nm and (b) 854 nm.

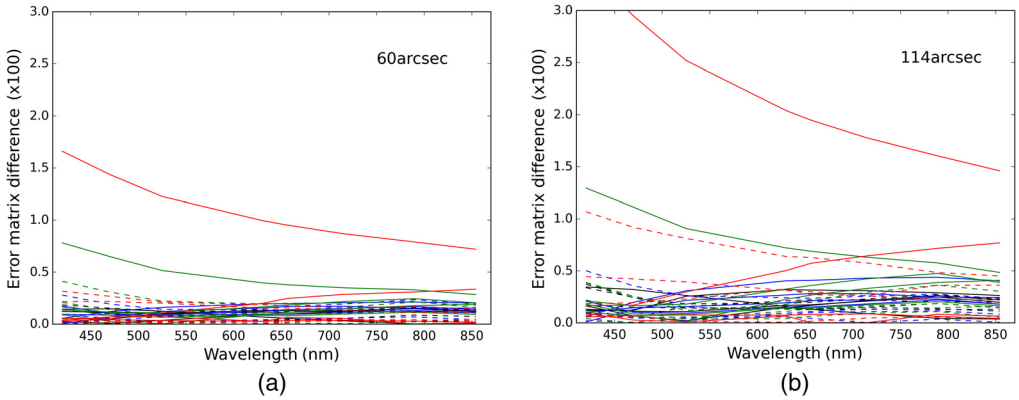

Fig. 15 The error matrix elements across wavelength multiplied by 100. Each color shows a different Stokes parameter with four matrix elements per Stokes parameter. (a) ±60-arc sec field angles. (b) ±114-arc sec field angles.

aperture. The retarder transmission is quite uniform at levels below measurement noise of 0.02% except for the few small patches of optical contact defect.

5.4 *Error Budget Comparison to Error Matrices*

$$\mathbf{E}_{420\ \mathrm{nm},0'} = 10^{-3}\begin{pmatrix} 0 & 0 & 0 & 0 \\ 0 & -0.3 & -0.1 & 0 \\ 0 & 0.1 & -0.3 & 0 \\ 0 & 0 & 0 & -0.6 \end{pmatrix}, \tag{13}$$

$$\mathbf{E}_{420\ \mathrm{nm},1'} = 10^{-3}\begin{pmatrix} 0.2 & 0.9 & 1.4 & -0.3 \\ -1.4 & -0.5 & -1.4 & -0.4 \\ 1.2 & -1.7 & -7.8 & 16.6 \\ 0.6 & 0 & -0.9 & 0.6 \end{pmatrix}. \tag{14}$$

As examples of DKIST calibration errors, we show the difference between the identity matrix and the response matrix at 420 nm wavelength in Eq. (13) for the on bore sight beam at zero field angle and in Eq. (14) for a field angle of 1 arcmin. The arrays shown are in parts per thousand and

rounded to 1 decimal place. Errors are typically above a few 10^{-4} and above 10^{-3} for some terms. We choose these values for comparison with our prior work HS18b[66] Eq. (4) where we only included the terms from the retardance spatial variation in the simulation. The error matrix values here are more than an order of magnitude larger than from the retardance spatial variation alone. Now the on-axis beam also shows errors above a few 10^{-4} caused by the decentered footprints seen with misaligned GOS calibration optics:

$$\frac{\mathbf{E}_{420\ \mathrm{nm},0'}}{\mathbf{E}_{\mathrm{budget}}} = \begin{pmatrix} 0 & 0 & 0 & 0 \\ 0 & 0.03 & 0.01 & 0 \\ 0 & 0.01 & 0.03 & 0 \\ 0 & 0 & 0 & 0.06 \end{pmatrix}, \tag{15}$$

$$\frac{\mathbf{E}_{420\ \mathrm{nm},0.2'}}{\mathbf{E}_{\mathrm{budget}}} = \begin{pmatrix} 0 & 0 & 0 & 0 \\ 0.8 & 0 & 0.1 & 0 \\ 0.5 & 0.1 & 0.2 & 0.8 \\ 0.2 & 0 & 0 & 0 \end{pmatrix}, \tag{16}$$

$$\frac{\mathbf{E}_{420\ \mathrm{nm},1'}}{\mathbf{E}_{\mathrm{budget}}} = \begin{pmatrix} 0 & 0.1 & 0.1 & 0 \\ 2.9 & 0.1 & 0.3 & 0.1 \\ 2.4 & 0.3 & 0.8 & 3.3 \\ 1.1 & 0 & 0.2 & 0.1 \end{pmatrix}. \tag{17}$$

If we divide the error matrix terms of Eq. (13) for a field position on axis (0 arcmin) at 420 nm wavelength by a nominal error matrix goal of Eq. (12), we get the error ratio of Eq. (15). This shows that the beam on the telescope bore sight is in error by at most 6% of the nominal error budget of Eq. (12). In Eq. (16), we show the same calculation for a field angle of 0.2-arc min field angle (12 arcsec) where two terms are within 80% of the error budget limit. The other 14 error terms are low. Similarly, we divide the error matrix terms for a field angle of 0.2 arcmin at 420 nm wavelength by a nominal error matrix goal of Eq. (12) to get the error ratio of Eq. (16). This highlights a few terms that are factors of 2× to 3× larger than our nominal error limit from Eq. (12). We show the 1-arcmin field angle error ratio in Eq. (17). Calibrations at this wavelength and field angle would have a few error matrix terms in the I to QUV polarizance column roughly factor of few above the nominal error tolerance. Of course, the exact error limits required depend on the science use case, observing conditions, cadence, instrumentation, and a very long list of telescope and instrumental factors. However, the process outlined here shows that we have combined several polarizer inhomogeneities (transmission, contrast, and extinction orientation) with several retarder inhomogeneities (transmission and elliptical retardance) including misalignments to the calibration optics to show the combined system error compared with nominal error limits.

These simulations show that the retardance spatial uniformity from HS18b[66] and H20[86] is currently not the major limitation of our calibration process. Producing a more detailed error budget extracting the relative contribution of each error term is possible with these kinds of simulations. This work suggests improving the uniformity of polarizer transmission, retarder transmission, and centering of the calibration optics as immediate and feasible ways to improve calibration accuracy over wider field angles. We note that calibrations taken around the telescope optical bore-sight will have errors much smaller than at the 1-arcmin field angle. Observations requiring high calibration accuracy can easily be planned with frequent repointing of the telescope as opposed to using very wide instrument field scanning techniques. We also note that there are several algorithmic techniques, which introduce more fitting variables that can also mitigate these issues for the optics DKIST currently owns. We show examples of these algorithms in Appendix B. With design simulations as presented here, future observatories can perform more realistic system level performance trades combining several error sources. The trade offs between various error sources given optical specifications and measured as-built performance can be assessed using this kind of calculation.

6 Wire Grid Polarizer Spatial and Spectral Fringes

For solar telescopes, the optic heat loads can easily degrade and damage polarizers. There is a particular concern for calibrators, which must be placed as far up the optical path as possible in primary or Gregorian foci. A crystal sapphire substrate presents advantages in substrate strength, thermal conductivity roughly 20 times larger than fused silica and improved infrared transmission. In particular, the DKIST instrument Cryo-NIRSP calibrations at the 4.6-μm wavelength spectral line can benefit from transmission improving by a factor of at least 2. The Cryo-NIRSP instrument throughput can be further improved through rebuilding the analyzer beam splitting assembly as there is another transmission through a fused silica wire grid polarizer for both polarized beams incurring similar absorption losses. The high refractive index of sapphire makes fringes a substantially larger concern. Alternates such as CaF2 or MgF2 are also possible but did not seem manufacturable at large size given materials source limitations and fragility.

As we presented in H21,[68] the measured polarizer substrate edge temperatures are over 100°C with estimates of the aperture center temperature roughly double this value. The polarizers have performance guaranteed for some few thousand hours of operation at 250°C but reduced temperatures would likely extend the lifetime as well as potentially mitigate any local seeing effects. A crystal sapphire substrate has several disadvantages though as the substrate is now birefringent. This leads to design choices when using a C-plane substrate cut as a window or an A-plane substrate cut as a retarder with wires aligned along the substrate fast axis. There are additional concerns about interference fringes, transmitted wavefront error through substrate flatness, and also reflected wavefront flatness for use in analyzing beam splitter applications. We did not apply any antireflection coatings to the polarizer substrate back surfaces for several reasons including very wide wavelength range, durability, and high temperature operations.

At DKIST, we funded and worked with Moxtek to develop a sapphire substrate wire grid polarizer similar to the UVT-240A model of other DKIST polarizers. Moxtek tested a few wire heights, pitch sizes, and manufacturing processes. We also tested A-plane and C-plane cut substrates and samples for polarizer contrast and transmission. For collimated beams in our labs, we did not see much difference between contrast measurements with the wire side of the polarizer facing each other (wires-in configuration) or when the polarizer substrates were in between the wires (substrate-in configuration). Ultimately, we decided to fabricate a C-plane cut calibration polarizer for DKIST as the uncoated substrate side faces the incoming beam. In DKIST, our calibration algorithms allow for fitting the partial polarization of the incoming beam so we wanted a substrate with as little retardance as possible at the risk of possibly lower contrast through crossed polarizers in the substrate-in orientation.

We show here the detection of transmission interference fringes using our lab Mueller matrix spectropolarimetry system along with use of the fringes to derive substrate thickness variation. We find the crystal sapphire substrate has roughly eight times worse thickness uniformity compared with the fused silica substrate over a 90-mm diameter aperture.

6.1 *Spectrally Resolving Fringes*

The upgraded Avantes dual-EVO (DEVO) system used in our Maui labs resolves spectral interference fringes for these relatively thin polarizer substrates. As described more in Appendix C, the system achieves spectral resolving power of 2400 to 4400. We can use these fringes to derive the substrate thickness variation and relate this to expected fringe magnitudes in DKIST. Other telescopes using wire grid polarizers in more collimated beams or closer to pupil planes can use this information to derive an upper limit on interference fringes created by these wire grid polarizers. As polarizers often rotate in the beam, optical specifications of low beam deflection (wedge) and reasonably good flatness are typically required for astronomical applications.

Figure 16 shows the interference fringe spectral period computed as $\lambda^2/2dn$ for the wavelength (λ), the substrate physical thickness (d), and the substrate refractive index (n). We show our C-plane cut 0.7-mm-thick crystal sapphire substrate as the thick dashed black line. We show the fringe period for the 1.0-mm-thick fused silica substrate for the UVT parts as the dashed green line for reference. The solid blue curve and the right-hand Y axis of Fig. 16 shows the birefringence oscillation spectral period computed as $\lambda^2/2db$ for the wavelength (λ), the

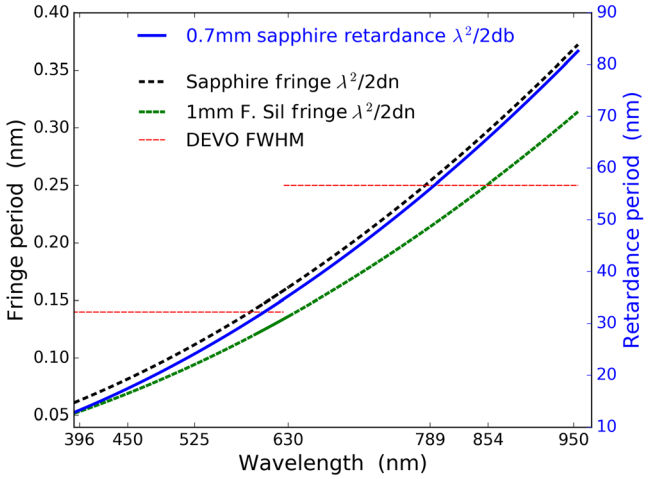

Fig. 16 The fringe periods as the dashed black curve plotted on the left-hand *Y* axis for our 0.7-mm-thick sapphire substrate. Fringe periods rise from 0.05 to 0.35 nm over the DEVO bandpass. We show the VIS and NIR optical profile FWHM as the horizontal dashed red lines to illustrate system resolving power limits. The blue line using the right-hand *Y* axis shows the retardance oscillations from the birefringence.

substrate physical thickness (d), and the substrate birefringence computed as the difference between extraordinary and ordinary refractive indices ($b = n_e - n_o$). We expect to marginally detect the interference fringes at the longer wavelength end of both EVO systems.

6.1.1 *Sapphire CalPol: transmission spectral fringes spectra and aperture oscillation*

The broad spatial transmission oscillation is highly repeatable in the sapphire polarizer. Figure 17 shows example spectra where we detect both the interference fringes and the spatial transmission oscillations in the sapphire polarizer. Different colors show the three repeated maps. The interference fringes change significantly between maps both in intensity and fringe phase. Figure 17(a) shows a bandpass near 600 nm wavelength with the VIS EVO where both the optical full width half maximum (FWHM) and the fringe period are 0.14 nm. These fringes

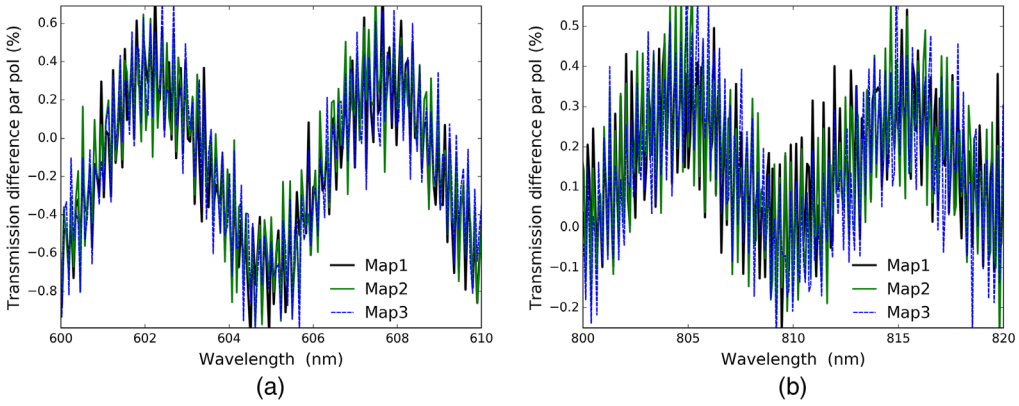

Fig. 17 The fringes resolved for a single spatial location in the three repeated spatial maps. Black shows the first repeated map. Green shows the second map. Blue dashed shows the third map. (a) 600 nm wavelength with the VIS EVO using the 1.5-mm diameter lamp mask. (b) 800 nm wavelength with the NIR EVO using the 2.5-mm diameter lamp mask. The magnitude and phase of the interference fringes change significantly between repeated maps but the broad envelope is consistent. Fringe magnitude changes with beam footprint diameter but fringes are clearly detected in all maps for all beam footprints run.

were detected at magnitudes near $\pm 0.2\%$ with the 1.5-mm diameter lamp beam. Figure 17(b) shows a bandpass near 800 nm wavelength recorded with the NIR EVO system where both the optical FWHM and the interference fringe period are 0.25 nm. This graphic shows a 2.5–mm-diameter beam footprint and detects fringes near $\pm 0.2\%$ magnitude. The theoretical fringe magnitude for uncoated sapphire at $n = 1.8$ and a single surface Fresnel reflection of 7.5% would be 30%.

6.1.2 *Sapphire CalPol: transmission spatial fringe maps*

We show the spatial maps of transmission in Fig. 18. Substantial spatial fringes are seen at all wavelengths. As we detect spectral interference fringes at some magnitude, we can use this sensitivity to measure spatial variations in wafer thickness, which modulate the spectral fringes. A single wave spatial fringe would correspond to the double-pass thickness change of one wave in the transmission of P-polarization. For the interference calculations, the 0.7-mm sapphire substrates are 6000 waves thick in double-pass at a wavelength of 414 nm falling to 3000 waves thick at 818 nm wavelength. In double-pass for interference, a sapphire extraordinary beam at $n = 1.75$ sees 854 nm of optical path change for a physical thickness change of 243 nm $[854/(2 * 1.75)]$. There are roughly 10 transmission fringe peaks spatially across a 100-mm diameter aperture at 854 nm wavelength. This corresponds to 2.4 μm of physical thickness variation across the wafer substrate. Given the fringe spatial pattern, this thickness variation has low spatial frequency and looks to be dominated by focus/spherical type terms but offset from the aperture center. The sapphire polarizer wafer was anticipated to have substantially worse thickness uniformity than common fused silica wafers.

6.1.3 *CalPol1 spare: transmission spectra, spatial fringes, and spectral fringes*

The spatial mapping also detects fringes in the CalPol1 Spare polarizer. We recorded a 0.75-mm spaced rosette with a 1.5-mm diameter beam out to a 48-mm maximum radius. The interwoven lamp exposures reduced flux gradients below $\pm 0.006\%$. In Fig. 19, we show the aperture median transmission spectrum for wire-perpendicular polarization state as the thick blue line. The thin black line shows an example spectrum from a single spatial position. We note that there are spectral fringes at magnitudes up to $\pm 0.5\%$ in addition to spatial fringe influences increasing that spectral transmission variation to magnitudes above $\pm 0.8\%$. The shot noise limit in the black curve is far below 0.1% at most wavelengths with the black curve being mostly fringes for the longer wavelengths of both spectrographs.

Figure 20(a) shows the spectral fringes for a particular bandpass and spatial location near 920 nm wavelength. The fringe period for the 1.0-mm-thick fused silica substrate is 0.30 nm at this wavelength just barely larger than the 0.25-nm optical profile of the NIR spectrograph. With roughly one optical profile per fringe, we anticipate very low fringe magnitudes. Different colors show the three repeated spatial maps with good agreement between spectra and some small

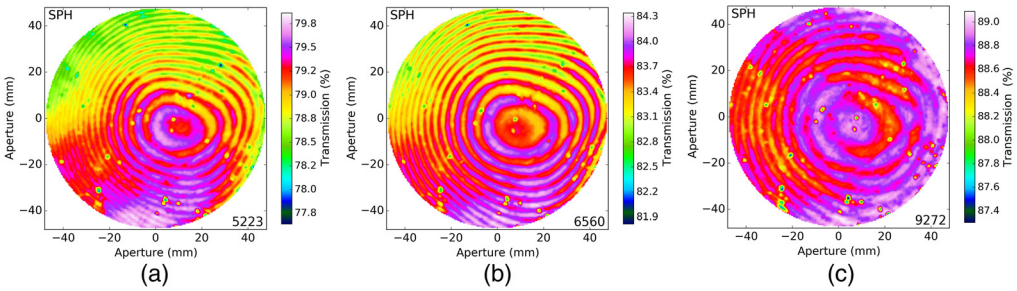

Fig. 18 The transmission maps derived from four maps of 3571 spatial samples with 2.5 mm spatial masking and 1.5 mm radial steps to a maximum radius of 51 mm. Some rejection of vignetted edge points on the right side of the aperture is seen in the noncircular shape of the aperture. Wavelengths shown are (a) 522.3 nm, (b) 656.0 nm, and (c) 927.2 nm.

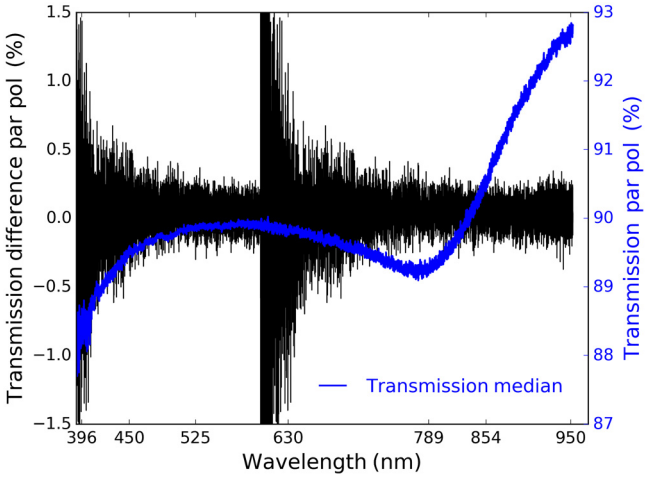

Fig. 19 The blue shows the aperture median transmission spectrum over all 12,481 spatial locations using the right-hand *Y* axis. The black curves show example transmission spectra differences from the median select spatial locations.

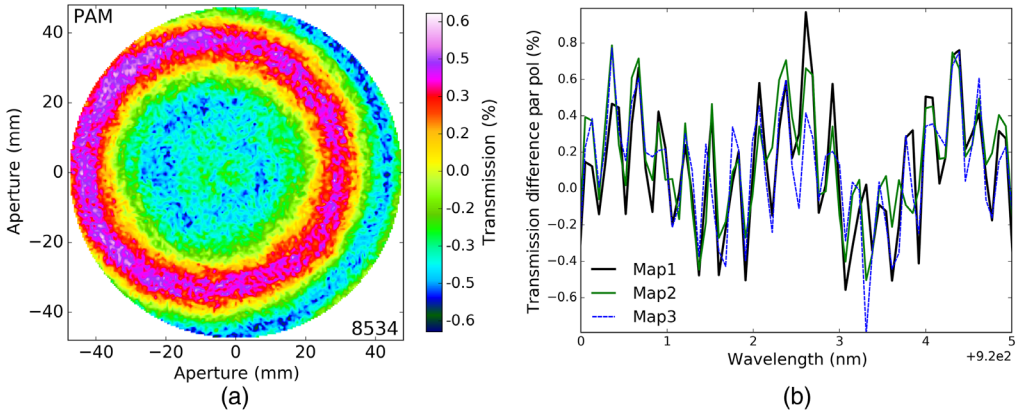

Fig. 20 (a) Spectral fringes between three repeated maps at one particular spatial location near 920 nm wavelength. (b) A spatial fringe map computed by subtracting a 16 spectral bin average to remove the spatial transmission variation. This highlights changes caused by spatial changes of spectral fringes. We note PAM in the corner as an alternate naming for the CalPol1 Spare optic has been used in instrument functional testing as a PAM.

changes in spectral fringe properties due to thermal drifts of the setup. Figure 20(b) shows a spatial fringe map computed by removing a wide spectral average map from an individual spectral pixel at full spectral resolution. We isolate the spatial fringe at a single wavelength by subtracting an average over the spectral fringes. We remove a wider bandpass transmission average as in Fig. 5 and are left with spatial fringes in Fig. 20(b). This shows a clear focus-like spatial variation of the transmission fringe with magnitudes near $\pm 0.6\%$.

For the interference calculations, the 1.0-mm fused silica substrates are 7500 waves thick in double-pass at a wavelength of 392 nm falling to 3500 waves thick at 830 nm wavelength. In double-pass for interference, a fused silica substrate at $n = 1.46$ sees 854 nm of optical path change for a physical thickness change of 292 nm $[854/(2 * 1.46)]$. There is only one transmission fringe peak spatially across the 100 mm diameter aperture at 854 nm wavelength for this polarizer. This would correspond to 0.3 μm of physical thickness variation across the substrate over the 96 mm aperture. This is roughly eight times more uniform thickness than the sapphire C-plane substrate above.

6.2 *Interference Fringes in F/13 Beam*

We previously calculated the potential mitigation of fringes in the converging beam by considering the spatial average over a footprint where the marginal ray propagating at an angle travels through a longer path leading to variable phase of interference. In HS18a,[63] we showed lab experiments and some basic calculations that were extended in H20[86] for some retarders designed to mitigate fringes in their particular mounting locations. We show here similar calculations.

The optical path length difference between chief and marginal rays provides spectral fringe reduction through averaging spatially over the beam footprint as shown in H18a.[63] The Berreman calculus[64,65] is limited to collimated beams of infinite spatial extent. As it is common with thin film calculations for filters, the Berreman calculations are first run over a range of incidence angles. These collimated beam calculations interpolated spatially over an aperture-weighted range of angles to approximate behavior in noncollimated beams. We showed a simple scaling relation where spectral fringe magnitudes are reduced as the inverse square of the marginal ray path. We found insignificant fringe magnitude reduction with ray path offsets less than a half-wave in our lab measurements of H18a.[63] For a thin window, we can neglect the incomplete overlap between the backreflected beam and the incoming beam footprints. In this situation, we recover a simple division of amplitude-type interferometer for fringes of equal inclination also called Haidingers fringes. Detailed descriptions are in several optical textbooks including Born and Wolf Chapter 7[103] and Hariharan Chapter 2.[104] In particular, Born and Wolf, 6th edition, Chapter 7.5, Eq. (2) calls out the marginal ray path in the medium as $d/\cos\theta_g$ where the substrate thickness (d) is divided by the incidence angle refracted into the medium ($\cos\theta_g$) for the fringes localized at infinity. The optical path difference between the first surface reflected component of the marginal ray and the marginal ray component reflecting off the back surface (immersed) goes as $(2dn)\cos\theta_g$ after compensation for the path traveled in air by the first surface reflected component to form an outgoing parallel wavefront.

For the sapphire substrate at 0.7 mm thickness is roughly 3300 waves thick at 0.38 μm wavelength falling to 250 waves thick at 4.6 μm wavelength. The backreflected beam traverses twice this optical path. For sapphire, the refractive index falls from 1.79 to 1.64 over the same wavelength range. The $F/13$ beam would have a marginal ray traveling at 2.2 deg in air, computed as $\tan^{-1}(1/2F)$. This angle is reduced by the refractive index to 1.23 deg at 0.38 μm rising to 1.34 deg at 4.6 μm. This gives the marginal ray only 1.5 waves of extraoptical interference path at the shortest wavelength falling to 0.14 waves at 4.6 μm. The fused silica substrate at 1.0 mm is 40% thicker with a refractive index of 1.46 falling to 1.36 over the same bandpass. The marginal ray propagates at an angle of 1.51 deg rising to 1.62 deg. The marginal ray interference path has 2.7 waves of spatial variation at 0.38 μm falling to 0.2 waves at 4.6 μm.

In the top section of Table 5, we list the optical FWHM for the instrument profile corresponding to a particular spectral resolving power at three wavelengths. In the next section of Table 5, we show the fringe properties for the crystal sapphire substrate at 0.7 mm thickness. We first list substrate optical thickness for the backreflected chief ray in waves for the rows labeled waves thick, including the double pass through the substrate. We then list the refractive index for the substrate and then compute the marginal ray angle after refraction into the substrate at $F/13$. The optical path length difference through the substrate in waves between the marginal and chief rays is shown in the rows labeled Marg. - Chief $F/13$ in double-pass. We show the spectral fringe period in nanometers. The last two rows show how many instrument profile widths sample the spectral interference fringe at two spectral resolving powers. In all cases, the instruments with spectral resolving power more than 50,000 will easily resolve the fringes with eight to hundreds of FWHM. In the bottom section of Table 5, we repeat the calculations for the fused silica substrate at 1.0 mm thickness.

As the marginal ray path is typically <1 wave different than the chief ray, we expect little fringe magnitude reduction in our $F/13$ beam. We conclude that there may be some detectable interference fringes at the predicted spectral periods for these two substrates. Both polarizer substrates had fringes detectable with our lab metrology equipment. We expect some fringe magnitude reduction from the spatial average over a footprint where the substrate thickness is nonuniform, in addition to some limited reduction from the spatial fringe average at shorter wavelengths only.

Table 5 Polarizer fringe properties: sampling and OPD F/13.

Description	0.38 μm	1.56 μm	4.6 μm
FWHM 300k	1.3 pm	5.2 pm	15.3 pm
FWHM 50k	7.6 pm	31.3 pm	92 pm
Waves thick saph.	6595	1555	500
Ref. index	1.79	1.74	1.64
Marg. ray angle	1.23 deg	1.27 deg	1.34 deg
Marg. - chief $F/13$	1.5	0.4	0.1
Fringe period	0.06 nm	1.00 nm	9.2 nm
Optical samples@300k	45	192	600
Optical samples@50k	8	32	100
Waves thick F.Sil.	7740	1840	590
Ref. index	1.47	1.44	1.36
Marg ray angle	1.50 deg	1.53 deg	1.62 deg
Marg. - chief $F/13$	2.7	0.47	0.2
Fringe period	0.05 nm	0.85 nm	7.8 nm
Optical samples@300k	38	163	510
Optical samples@50k	6	27	85

7 Summary

We presented new metrology for the DKIST polarizers and retarders on apertures larger than 90 mm diameter with thousands to tens of thousands of spatial sampling points at spectral resolving powers over a few thousand covering 390 to 1600 nm. We improved our lab metrology tools to include the polarizer contrast ratio and angle of maximum extinction in addition to transmission and elliptical retardance parameters. This metrology covers most wavelengths anticipated for the DKIST science instruments during the commissioning and early operations phase. We created a simulation to model the inaccuracies in calibrating a telescope by propagating Mueller matrices across decentered beam footprints through asymmetric calibration sequences. We include spatial variation within individual beam footprints where the calibration polarizer transmission, contrast, and angle of maximum extinction all vary, simultaneously with variations in calibration retarder transmission and elliptical retardance. The simulations used metrology results from the DKIST calibration optics to provide more realistic estimations of the inaccuracies caused by calibrating large field angles at a wide range of wavelengths. We found that the transmission variation of the calibration polarizer measured at some wavelengths to be over 5% peak to peak combined with retarder transmission defects caused substantial errors in decentered footprints. We use these simulations to inform an inner field angle within which instrument calibration accuracy can be assumed to be within some limiting threshold. We also note that there are substantial trade offs that can be studied quantitatively with this kind of analysis. Alternate system model fitting techniques including more frequent intensity normalization and different choices on diversity of input states can mitigate some of the spatial variation issues presented here though not without other complications and impacts to the errors on other fitted variables. The response matrix elements were shown as a function of field angle for two wavelengths to show the general trends for calibration errors. This type of simulation also will inform

future procedures for calibrating astronomical instruments as calibration sequences can be designed to be efficient while attempting to minimize or at least isolate optic property spatial variation. Development projects to produce more spatially uniform polarizers and retarders are in progress.

We also provided some funding and worked with Moxtek staff on development of a crystal sapphire substrate wire grid polarizer. Detection of transmission interference fringes was presented in Sec. 6 and used to derive estimates of substrate thickness variation. Along with our previous estimates of interference fringe impacts on calibration (H18,[63] HS18a,[63] H20[86]), we can add polarizer substrate fringes to the list of errors considered in our system level performance estimates. The benefits of improved infrared transmission and thermal behavior can be studied against issues with interference fringes or transmitted wavefront error should either show degradation during use at the telescope.

8 Appendix A. Footprints and Simulation Details

This appendix shows additional details of the Mueller matrices calculated from metrology, the beam optical footprints, and additional details of the model fitting.

8.1 *A.1 Footprint Details*

The beam footprints and associated optic apertures vary for the three levels in the DKIST GOS. In Fig. 21, we show the beam footprints for field angles of 2.0, 2.8, and 5.0 arcmin with an X-Y fan orientation. The master polarizer in level 3 is farthest away from Gregorian focus at 550 mm. The calibration polarizers at level 2 are closer at 450 mm ahead of focus. The calibration retarders are closest at 350 mm ahead of focus.

The optics spin during calibration but the aperture area covered can be optimized when balancing the calibration sequence efficiency. The area of the optic sampled changes as a function of field angle coupled with misalignments decentering the beam. Each footprint samples a different patch of each optic. The simulations use the metrology from the appropriate optic in a footprint of the appropriate decenter and diameter at the appropriate clocking angle.

We note that the 10 state sequence has nonuniform weighting across the aperture of each calibration optic. The polarizer swings through a 120-deg arc but there are four inputs at 0 deg and four inputs at 45 deg putting 80% of the inputs within a fairly small patch of the optic aperture. A globally constrained transmission fit adds heavy weighting and constraint to these states, reducing the influence of other issues related to the nonuniform retarder rotating underneath. We show these two footprints in Fig. 22 as a function of field angle.

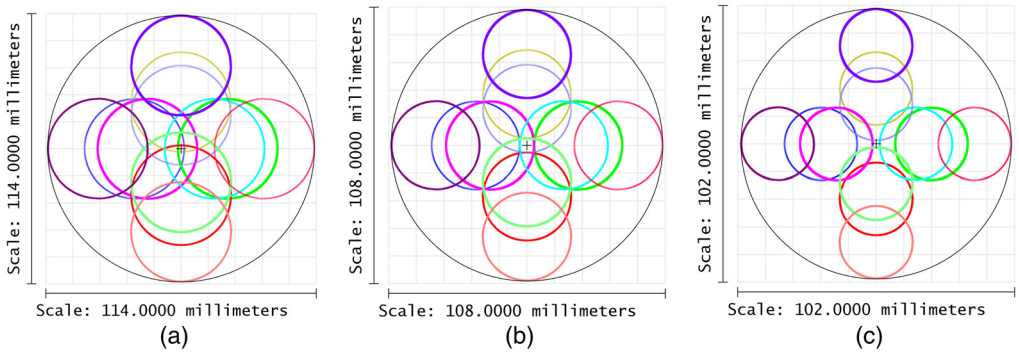

Fig. 21 The footprints over the field of view for the GOS polarization calibration optics. (a) The level 3 master polarizer. (b) The level 2 calibration polarizer. (c) The level 1 calibration retarder station. Field angles are depicted in a linear *X Y* fan at 1, 1.4, and 2.5 arcmin radius to cover the 2, 2.8, and 5 arcmin fields.

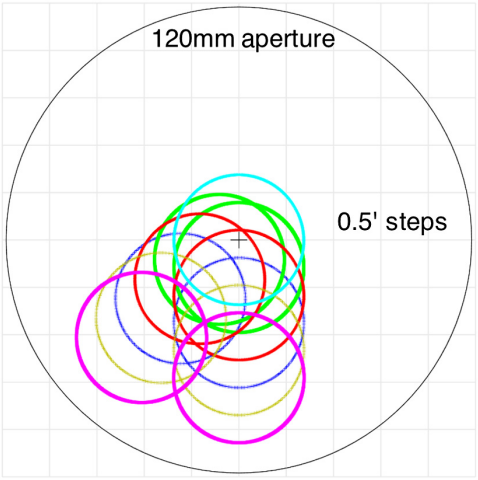

Fig. 22 The 0-deg and 45-deg orientation footprints on the calibration polarizer for positive field angles from 0 to 2.5 arcmin in steps of 0.5 arcmin. Note that 8 of the 10 calibration inputs for our sequence are at these two orientations.

8.2 *A.2 Retarder Footprint Mueller Matrix Element Spatial Variation*

On the retarder transmission, there are three calibration input states with the GOS retarder out of the beam, and seven input states with the retarder in the beam when using our nominal 10 state calibration sequence. The retarder uses a 150-deg arc of the optic aperture and only the 0-deg orientation is repeated twice. No other aperture positions are repeated. Input states use 30-deg

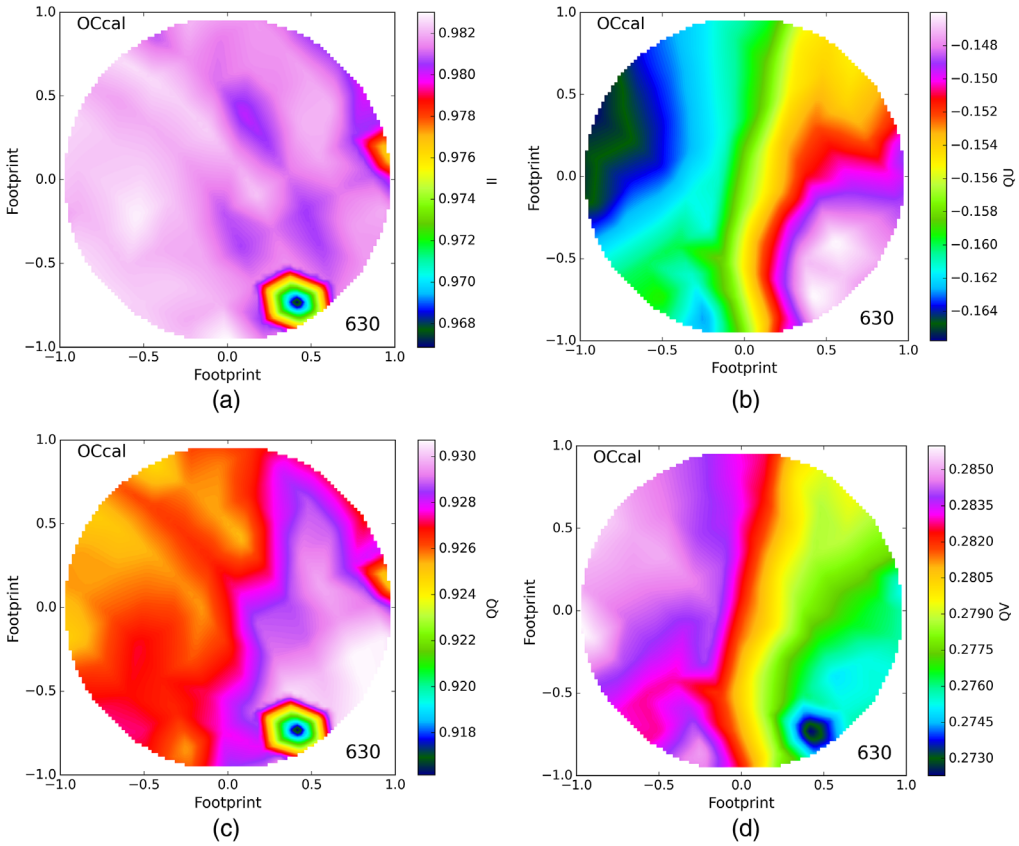

Fig. 23 The properties within individual footprints for the beam on the OCcal while at a 45-deg orientation for a +1.9-arcmin field angle at a wavelength of 630 nm. (a) II, (b) QU, (c) QQ, and (d) QV.

retarder rotation spacing. This results in a very different impact of retarder transmission uniformity with stronger coupling of the elliptical retardance nonuniformity. Examples of the spatial variation of the Mueller matrix elements across a beam footprint are shown in Fig. 23 for the OCcal retarder at an orientation of 45 deg, a wavelength of 630 nm, and a field angle of +1.9 arcmin. We see one aperture defect patch in the lower right-hand corner of the footprint dominating the II term errors in Fig. 23(a). The QU term, however, does not show substantial impact from this transmission artifact in the aperture.

8.3 *A.3 Footprint Mueller Matrix Variation: Polarizer at 0 deg*

The variation across the individual beam footprint on the polarizer contains several combined artifacts. We show the Mueller matrix variation across the beam footprint for a polarizer orientation of 0 deg at a wavelength of 420 nm in Fig. 24. We use the convention where all elements besides II are normalized by the II element to remove transmission from all other elements. We note the UU and VV terms range from roughly 0.017 to 0.034 under this scaling. This corresponds to a polarizer contrast of roughly 2000 to 6000. See Appendix E for additional details on relating an imperfect polarizer to contrast and Mueller matrix element magnitudes. There is substantial symmetry in the agreement between IQ and QI, IU and UI, and finally QU and UQ. All terms related to V aside from VV are also zero.

8.4 *A.4 Footprint Mueller Matrix: Polarizer at 0 deg, Retarder 0 deg*

The variation across the individual beam footprint for the polarizer combined with the retarder contains several additional artifacts. We show the Mueller matrix variation across the beam footprint for a polarizer orientation of 0 deg followed by the OCcal retarder with an orientation of

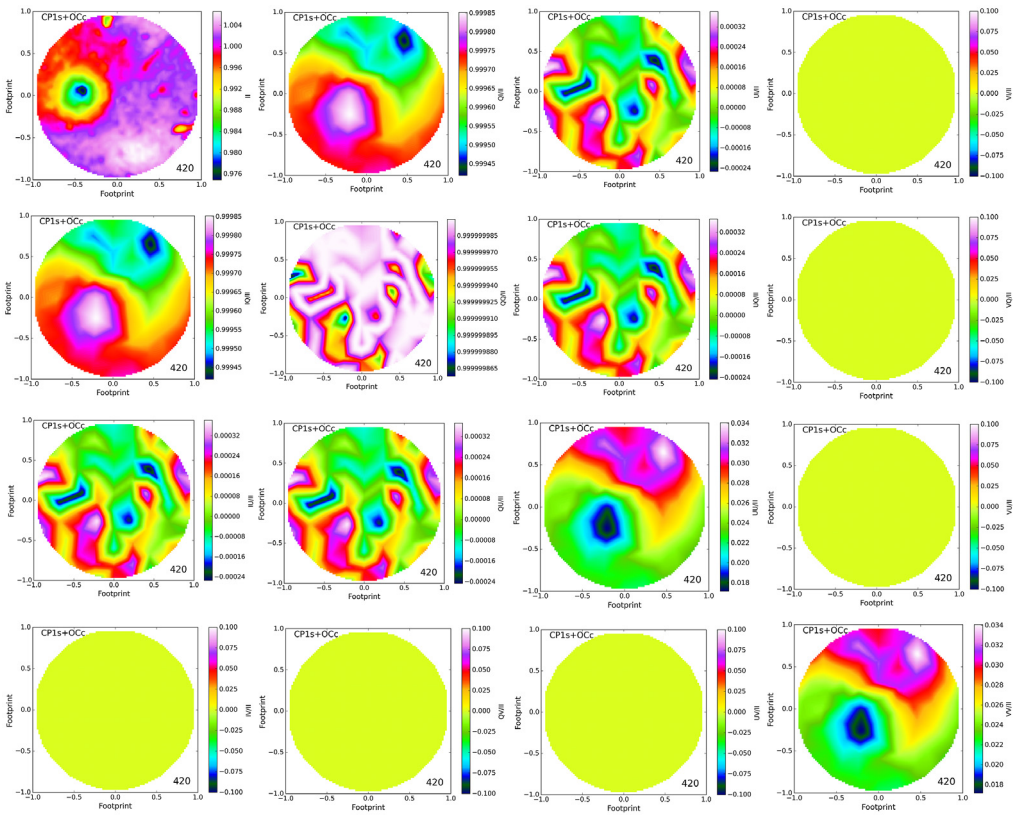

Fig. 24 Example Mueller matrix element variation within individual footprints for the beam on the calibration polarizer (CalPol1 Spare) while at a 0-deg orientation for zero field angle at a wavelength of 420 nm.

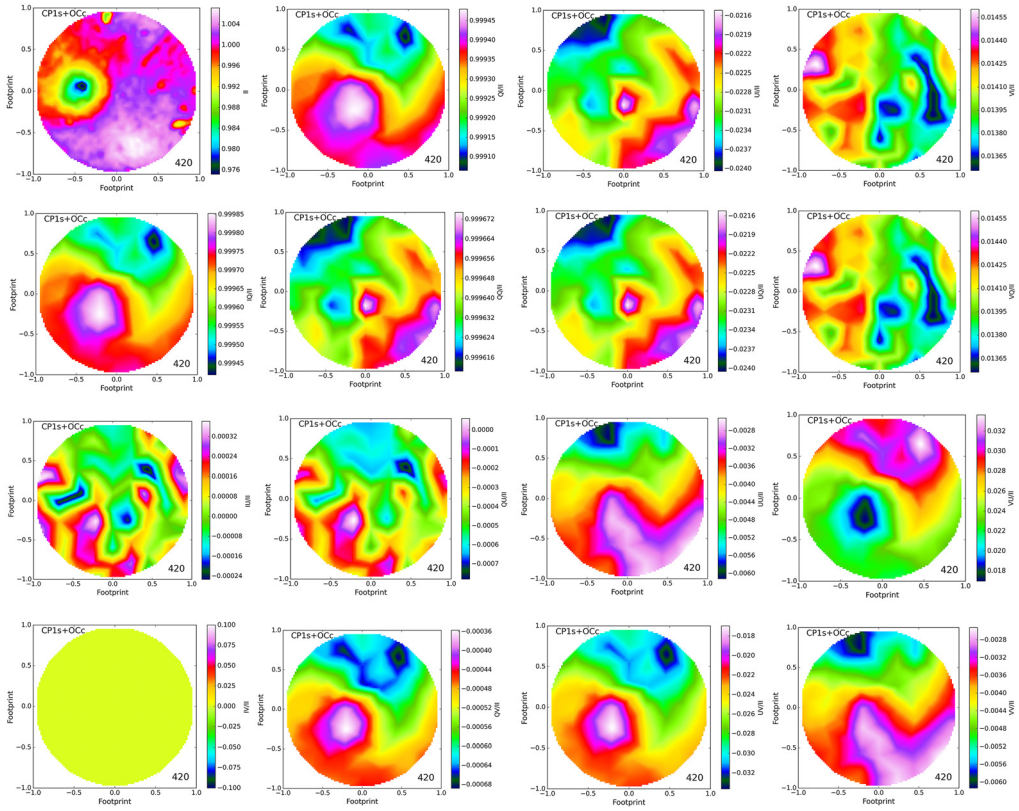

Fig. 25 Example Mueller matrix element variation within individual footprints for the beam on the calibration polarizer (CalPol1 Spare) followed by the calibration retarder (OCcal) while both optics are at a 0 deg orientation for zero field angle at a wavelength of 420 nm.

0 deg at a wavelength of 420 nm in Fig. 25. We use the convention where all elements besides II are normalized by the II element to remove transmission from all other elements.

9 Appendix B. Comparing Various Intensity Normalization Models

Many algorithmic choices are available for fitting variables accounting for optic transmission variation, performance parameters, atmospheric transparency fluctuations, etc. However, more variables in any simulation can degrade accuracy even though the formal fit metric might improve. We show in this appendix some examples of adding or restricting variables and their impact on the accuracy of demodulation. A thorough examination of all possible algorithms in the presence of multiple systematic errors is beyond the scope of this paper. We illustrate here a few common choices. In general, we find that adding more variables degrades the demodulation accuracy though improving the fit to the modulated intensities with the few systematic errors included in this study.

9.1 *B.1 Relative Polarization and Normalization by One Modulation State*

In the case of polarization calibration, adding intensity normalization may be beneficial to compensate for spatial variation of optic transmission and future atmospheric variations. However, there is also the competing possibility of degraded calibration accuracy due to the degenerate coupling of various optic imperfections into the fitted intensities. The metric for our success is the accuracy of the derived modulation matrix. The metric for model fitting success is minimizing intensity differences between data and model. Intensity fitting could improve at the cost of lower calibration accuracy. We outline here a fit to our simulations using a relative polarization model, similar to I08, but done without use of a response matrix.

We adopted a notation where n is the index of the calibration state for the configuration of both calibration optics. We denote the total number of modulation states as m. In total, this system contains $(m \times n)$ linear equations and contains $(m \times 4)$ unknowns. The $(m \times n)$ equations can equally be represented as

$$i_{mn} = \begin{pmatrix} O_{m1} & O_{m2} & O_{m3} & O_{m4} \end{pmatrix} \begin{pmatrix} I \\ Q \\ U \\ V \end{pmatrix}_n, \quad n = 1,2,3,\ldots,N; \quad m = 1,2,3,\ldots,M, \tag{18}$$

which is also equivalent to

$$i_{mn} = \begin{pmatrix} I & Q & U & V \end{pmatrix}_n \begin{pmatrix} O_{m1} \\ O_{m2} \\ O_{m3} \\ O_{m4} \end{pmatrix}, \quad n = 1,2,3,\ldots,N; \quad m = 1,2,3,\ldots,M. \tag{19}$$

Since each row of modulation parameters are independent, the solution to this system is made simpler by solving each row of the modulation matrix individually, which is the method used by Selbing.[100] Stated alternatively, we treat separately the collection of N modulated intensities for each individual row of M rows of the modulation matrix. To write this explicitly, we solve M separate sets of linear equations defined as follows:

$$\begin{pmatrix} i_{m1} \\ i_{m2} \\ \vdots \\ i_{mN} \end{pmatrix} = \begin{pmatrix} I_1 & Q_1 & U_1 & V_1 \\ I_2 & Q_2 & U_2 & V_2 \\ \vdots & \vdots & \vdots & \vdots \\ I_N & Q_N & U_N & V_N \end{pmatrix} \begin{pmatrix} O_{m1} \\ O_{m2} \\ \vdots \\ O_{mN} \end{pmatrix}, \quad m = 1,2,\cdots,M. \tag{20}$$

This is equivalent to writing $\mathbf{i}_m = \mathbf{M}_{\text{Stokes}}\mathbf{O}_m^T$ in matrix notation with m in the range $(1, M)$. This form of the equations is a direct analog to those often used in linear regression theory. Applying this solution to Eq. (20), we can write the Morse–Penrose inverse as the standard least squares solution:

$$\hat{\mathbf{O}}_M^T = (\mathbf{M}_{\text{Stokes}}^T\mathbf{M}_{\text{Stokes}})^{-1}\mathbf{M}_{\text{Stokes}}^T\mathbf{i}_m, \quad m = 1,2,\ldots,M. \tag{21}$$

Using this equation, we directly infer the solution to the ordinary linear least squares problem without the need for iterative nonlinear methods. In the absence of intensity variations and/or unknowns regarding the calibration vectors introduced to a polarimeter, Eq. (21) is the simplest means to determine the modulation matrix of the system. Similar methods can be used for the Mueller matrix if the measurements represent Stokes vectors.

Alternatively, fitting only the relative DoP after dividing out an intensity measurement improves our resilience to absolute polarization fluctuations caused by either intensity changes and/or the coupling of our model with a polarizing telescope. One method for this applied to the Mueller matrix response matrix formalism is discussed by I08 for the Hinode spectropolarimeter. Note that to fit for the relative DoP, we require a way to normalize the data that is distinct from I08. We can extend this method for the modulation matrix as follows. We can write the measured intensities as

$$\begin{pmatrix} i_1 \\ i_2 \\ i_3 \\ \vdots \\ i_m \end{pmatrix}_n = I_n \begin{pmatrix} O_{11} & O_{12} & O_{13} & O_{14} \\ O_{21} & O_{22} & O_{23} & O_{24} \\ O_{31} & O_{32} & O_{33} & O_{34} \\ \vdots & \vdots & \vdots & \vdots \\ O_{M1} & O_{M2} & O_{M3} & O_{M4} \end{pmatrix} \begin{pmatrix} 1 \\ q \\ u \\ v \end{pmatrix}_n, \quad n = 1,2, \cdots, N. \tag{22}$$

We need to normalize each set of modulation states by the unknown intensity i_n. Assuming i_n is constant for one modulation cycle, every measured modulation state has this intensity encoded within it. For example,

$$i_{1,n} = i_n(O_{11} + O_{12}q + O_{13}u + O_{14}v). \tag{23}$$

Dividing each side of Eq. (22) by i_1, we get

$$\frac{\begin{pmatrix} i_1 \\ i_2 \\ i_3 \\ \vdots \\ i_m \end{pmatrix}_n}{i_n(O_{11} + O_{12}q + O_{13}u + O_{14}v)} = \frac{i_n \begin{pmatrix} O_{11} & O_{12} & O_{13} & O_{14} \\ O_{21} & O_{22} & O_{23} & O_{24} \\ O_{31} & O_{32} & O_{33} & O_{34} \\ \vdots & \vdots & \vdots & \vdots \\ O_{M1} & O_{M2} & O_{M3} & O_{M4} \end{pmatrix} \begin{pmatrix} 1 \\ q \\ u \\ v \end{pmatrix}_n}{i_n(O_{11} + O_{12}q_n + O_{13}u_n + O_{14}v_n)}, \quad n = 1,2, \cdots, N, \tag{24}$$

which reduces to a normalized form

$$\begin{pmatrix} i_2/i_1 \\ i_3/i_1 \\ \vdots \\ i_m/i_1 \end{pmatrix}_n = \frac{\begin{pmatrix} O_{21} & O_{22} & O_{23} & O_{24} \\ O_{31} & O_{32} & O_{33} & O_{34} \\ \vdots & \vdots & \vdots & \vdots \\ O_{M1} & O_{M2} & O_{M3} & O_{M4} \end{pmatrix} \begin{pmatrix} 1 \\ q \\ u \\ v \end{pmatrix}_n}{(O_{11} + O_{12}q_n + O_{13}u_n + O_{14}v_n)}, \quad n = 1,2, \cdots, N. \tag{25}$$

This formulation has the advantage of only considering the relative DoP generated by the telescope and calibration optics. It also removes the effect of intensity variations between calibration states, assuming that the intensity is constant during one modulation sequence. Once a sufficient solution is found with this formulation, one may attempt to parameterize the intensity variations more generally by demodulating the calibration data using the pseudoinverse of the inferred modulation matrix and then repeating the model using the absolute polarization. For our upcoming implementation, we adopt a slightly modified version of Eq. (25). Instead of normalizing by i_1, we normalize by the intensity state that has the maximum signal $\mathrm{Max}(i_m)$ for each N.

9.2 *B.2 Comparing Fits with Multiple Algorithms*

We list in Table 6 five different algorithmic scenarios to demonstrate various methods of intensity normalization. The first column gives a short name for the scenarios. All algorithm scenarios include three elliptical retardance variables constrained globally (ER) shown as the second column. In our nominal scenario, we enforce a single global variable for transmission of the polarizer (T_{pol}) and the retarder (T_{ret}). In the second simulation seen in row 2 (Rel Pol), we implement a fit including a separate polarizer transmission for each input Stokes vector. This adds nine variables to the fit for 10 total polarizer transmission fits (T_{pol}). This increases the total number of fitted variables from 28 to 37. We leave the retarder transmission (T_{ret}) as globally. In the third simulation seen in row 3 (Indiv T), we now combine the retarder and polarizer transmissions into

Table 6 Model variables and constraints.

	Descrip.	ER	T_{pol}	T_{ret}	T_{both}	Mod norm.	Vars
1	Global T	3	1	1	—	[0,0]	28
2	Indiv Pol	3	10	1	—	[0,0]	37
3	Indiv T	3	10	—	10	[0,0]	36
4	Indiv T Norm	3	—	—	10	Max([:,0])	36
5	Rel Pol	3	—	—	—	—	27

a degenerate transmission function for both combined optics in each input Stokes vector. This reduces the number of variables by 1 to a total of 36. In the fourth simulation seen in row 4 (Indiv T Norm), we change the way the first column of the modulation matrix is normalized. In the first three simulations, we enforced the [0,0] element of the modulation matrix to be 1. In the fourth simulation, we show a common alternate algorithm, where the entire modulation matrix is normalized by the maximum I modulation value. The Mod Norm column shows [0,0] for the first three simulations. We denote the "max first column" matrix normalization in Table 6 as Max([:,0]). The fifth simulation is the relative polarization simulation (Rel Pol) described in the prior section. There is no transmission function fit as the intensities are all normalized to the highest flux measurement.

In all cases, we had 60 measurements (10 input Stokes by six modulations) fitted to this range of variables from 27 to 37. In graphics of this section, we note that we do not show the Indiv Pol simulation where there are 10 transmissions of the polarizer (T_{pol}) and one global retarder transmission (T_{ret}). Results were very similar to the (Indiv T) simulation where each input Stokes vector is normalized using a transmission fit to a degenerate combination of polarizer and retarder transmission. There are no significant differences in fitted intensities, modulation matrix elements, or the resulting error matrix elements.

9.3 *B.3 Fitted Intensity Variation with Wavelength*

The field-dependent intensity variation of over ± 0.02 is reduced below ± 0.008 by the field-dependent fits. For the few algorithms demonstrated here, we do not see a very significant reduction in the difference between the fitted intensity and the synthetic data. Figure 26 shows fitted intensity residual differences between the best fit models and the synthetic data as a function of wavelength for the ± 114-arc sec field angle. Figure 26(a) shows the 28 variable global transmissions model with some modulated intensity outliers near ± 0.006. The bulk of the intensity

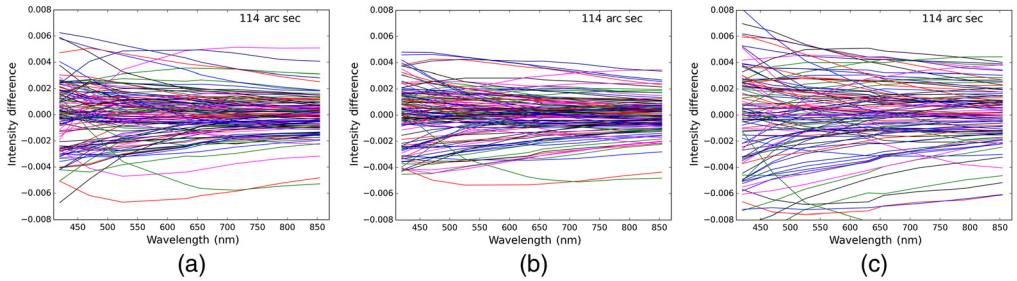

Fig. 26 The intensity fitting error for all six modulation states plotted against field angle for all wavelengths modeled. Each modulation state is a different color and there are 10 calibration states represented. (c) The same intensity fitting errors as a function of field angle using the same color scheme at 630 nm wavelength only. (a) The 28 variable global transmissions model. (c) The 36 variable individual transmissions model. This is nearly identical to the Max[0,:] modulation matrix normalization for the 36 variable individual transmissions model. (c) The relative polarization normalization model.

errors cluster around ±0.003. Adding the 10 transmission variables for the Indiv T model reduces the intensity difference outliers only slightly in Fig. 26(b). The intensity normalization of the relative polarization model seems to degrade the overall fitting at all wavelengths in Fig. 26(a).

9.4 *B.4 Fitted Intensity Variation with Field Angle*

Figure 27 shows the fitted intensity residual differences between the best fit models and the synthetic data as a function of field angle for a 630-nm wavelength. The added 10 transmission variables of the Indiv T model in Fig. 27(b) reduce the intensity errors slightly. There does not seem to be significant difference between the [0,0] normalization of the modulation matrix in Fig. 27(b) and Max(I) modulation matrix normalization so this model was not shown. The intensity fitting of the relative polarization model is again slightly worse as a function of field angle.

9.5 *B.5 Fitted Intensity Variation with Calibration State*

We show an example of the fitting errors with calibration input state at 114-arcsec field angle and a wavelength of 630 nm in Fig. 28. The difference between the best fit model intensities and the synthetic data intensities does not show substantial trends with calibration sequence state for the three different intensity normalization algorithms. There are differences in the errors between the algorithms, in particular Fig. 28(b) corresponding to the 10 individual polarizer transmission function fits. This 36 variable model shows better centering about zero for each modulated intensity. Figure 28(a) using global fits can show individual input Stokes vectors may be intensity normalized better or worse as they are not individually fit. Figure 28(c) shows the relative polarization model with marginally worse intensity fitting errors.

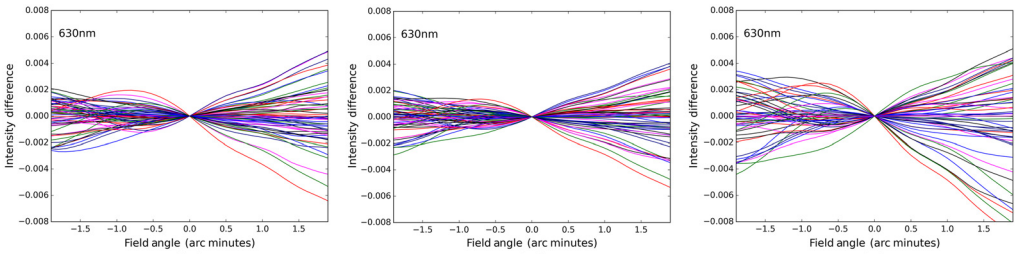

Fig. 27 The same intensity fitting errors as a function of field angle using the same color scheme at 630 nm wavelength only. (a) The 28 variable global transmissions model. (b) The 36 variable individual transmissions model. This is nearly identical to the Max[0,:] modulation matrix normalization for the 36 variable individual transmissions model. (c) The relative polarization model.

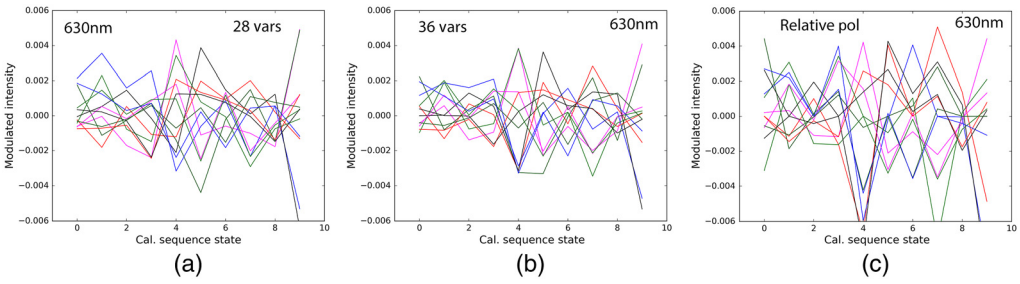

Fig. 28 The intensity fitting errors as a function of input calibration state for a field angle of 114 arcsec and a wavelength of 630 nm. The first three states have only the polarizer in the beam while the rest have both the polarizer and retarder. Each color shows the six different modulation states simulated. (a) The 28 variable global transmissions model. (b) The 36 variable individual transmissions model. This is nearly identical to the Max[0,:] modulation matrix normalization for the 36 variable individual transmissions model. (c) The relative polarization model.

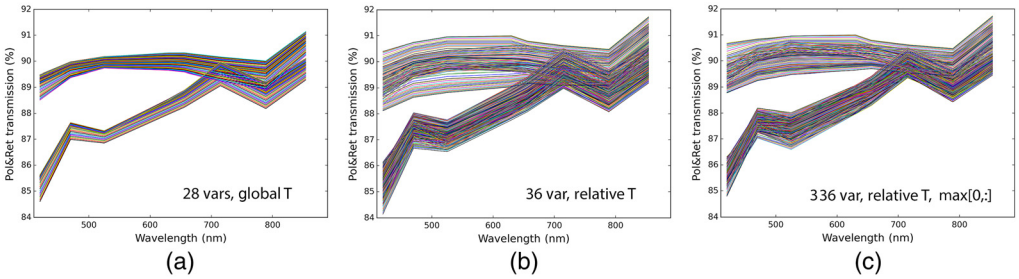

Fig. 29 The transmission of the polarizer and the combination of the polarizer and retarder as a function of wavelength. Each colored curve represents a different field angle. (a) The 28 variable global transmissions model. (b) The 36 variable relative transmissions model. (c) The Max[0,:] modulation matrix normalization for the 36 variable relative transmissions model. We note that the relative pol model does not fit transmission at all with the normalization.

9.6 *B.6 Fitted Calibrator Transmission Wavelength Dependence*

By fitting the calibration optic transmission variables as a function of wavelength and field angle, much of the variation across all footprints is mitigated even for the globally constrained fit. Figure 29 shows the transmission comparison between the retarder and combined polarizer with retarder. Each field angle is a different color. Substantial variations between different wavelengths can be seen in the polarizer, especially near the aluminum absorption band around 800 nm wavelength. The OCCal retarder has an antireflection coating with spectral oscillations (see H20[86]) and shows much less fitted transmission variation.

Figure 29(a) shows the 28 variable model with only one global transmission each for the retarder and polarizer. We note that for the first 28 variable model, we graph the fitted polarizer transmission multiplied by the fitted retarder transmission to generate the best fit combined transmission for the input Stokes vectors that use both retarder and polarizer. However, these were fit separately and globally for this particular model whereas Figs. 29(b) and 29(c) show the degenerate combination fit. Figure 29(b) shows the 36 variable model with 10 relative transmissions. There is nearly identical performance for the Max[0,:] modulation matrix normalization 36 variable model shown in Fig. 29(c). We note that the relative polarization model does not fit transmission for either optic.

Figure 30 shows the transmission comparison for a field angle of ± 114 arc sec compared to the field center fit. Dashed lines show the negative field angle whereas solid lines show positive field angles. For the 28 variable model, the is only one transmission function fit at each field angle. In Figs. 30(b) and 30(c), each colored curve is a different input Stokes vector showing a spread of over 1.5% variation for the fitted transmission functions. We note relative polarization model does not fit transmission at all given normalization hence it is not shown.

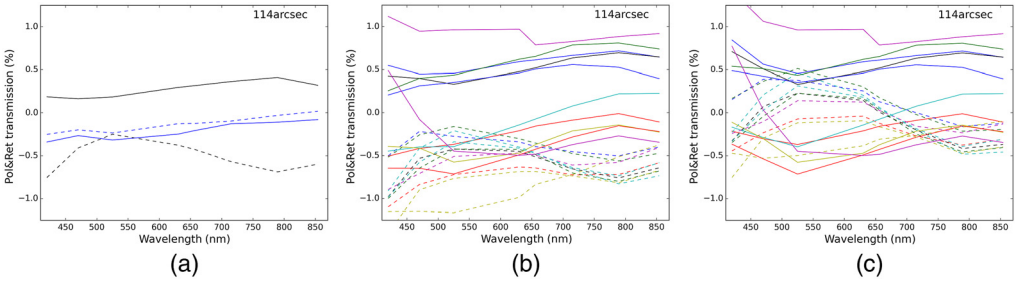

Fig. 30 The combined polarizer and retarder transmission function variation with wavelength at a ± 114-arc sec field angle. (a) The 28 variable global transmissions model. (b) The 36 variable relative transmissions model. (c) The Max[0,:] modulation matrix normalization for the 36 variable relative transmissions model.

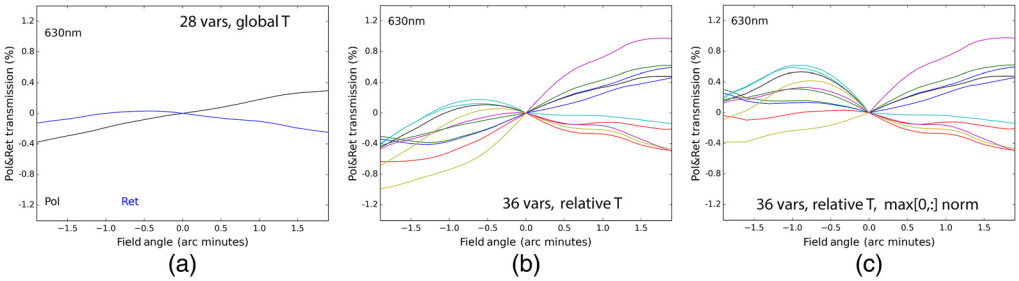

Fig. 31 The combined polarizer and retarder transmission function variation with field angle at 630 nm wavelength. (a) The 28 variable global transmissions model. (b) The 36 variable relative transmissions model. (c) The Max[0,:] modulation matrix normalization for the 36 variable relative transmissions model.

9.7 *B.7 Fitted Calibrator Transmission Field Dependence*

Figure 31 shows the transmission dependence as a function of field angle for a 630-nm wavelength. In Figs. 31(b) and 31(c), each colored curve is a different input Stokes vector showing a spread of over 1.5% variation for the fitted transmission functions. For the 28 variable model, in Fig. 31(a), there is only one global fit the retarder transmission in blue and polarizer transmission in black. We note that the relative polarization model does not fit transmission at all given normalization.

9.8 *B.8 Fitted Retardance with Wavelength and Field Dependence*

The elliptical retardance spatial variation is quite small compared with the magnitude of the retardance components. Figure 32 shows the elliptical retardance variation with field angle and wavelength. The first and second linear retardance components are shown in blue and green, respectively. The circular retardance is shown in red. Note that the 10-deg rotation was applied to the retardance metrology data to keep the retarder fast axis roughly aligned with the modeled zero position. This keeps almost all of the retardance magnitude contained within in the first component of roughly 100 deg at 400 nm wavelength falling to 45 deg at 850 nm. The second linear term and the circular term are below 3 deg.

Figure 33 shows the elliptical retardance parameters as a function of field angle. Multiple wavelengths are plotted each with the same color. Figure 33(a) shows the 28 variable global transmissions model. Figure 33(b) shows the 36 variable relative transmissions model. The Max[0,:] modulation matrix normalization for the 36 variable relative transmissions model is

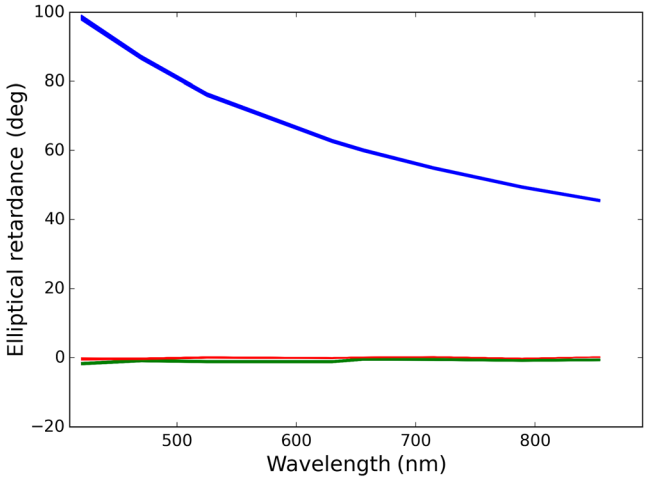

Fig. 32 The elliptical retardance at left as a function of wavelength and the field-dependent differences for all wavelengths at right.

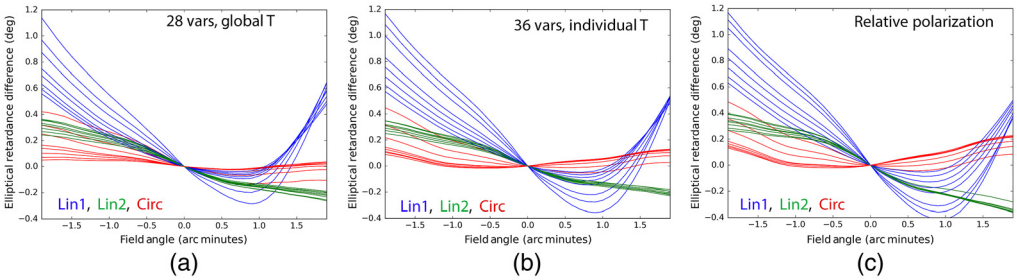

Fig. 33 The elliptical retardance changes with field angle. (a) The 28 variable global transmissions model. (b) The 36 variable individual transmissions model. This is nearly identical to the Max[0,:] modulation matrix normalization for the 36 variable individual transmissions model. (c) The relative polarization model.

nearly identical to the [0,0] normalization and is not shown. Figure 33(c) shows the relative polarization model fits on the same Y scale. The elliptical retardance variation shows that the first component of linear retardance (blue) varies by a factor of few more than the second linear component (green). The circular retardance fit field variation shown in red is yet again half as variable. We note that the first linear component is almost 100 deg at 420 nm wavelength falling to 50 deg at 850 nm wavelengths. Though both the circular and second linear components are near zero, a factor of 10 to >40 less than the first linear component, the field variation of those fitted values is driven to be much larger than the relative magnitudes.

9.9 *B.9 Fitted Modulation with Wavelength and Field Dependence*

The 24 terms of the modulation matrix represent the required calibration output for this system calibration model. The modulation matrix derived for an instrument is subsequently used to demodulate all data collected with that particular instrument configuration. Inaccuracies in this best-fit modulation matrix directly impact the accuracy of the measurements derived with the instrument. Figure 34 shows the modulation matrix field variation fit at 420 nm wavelength for the three different intensity normalization scenarios. In real instruments, we anticipate and must correct real variation of modulation matrix elements with field angle as retarder spatial variation causes substantial variation (see HS18b[66] and H20[86]). However, in this simulation, there is only one true matrix and all differences represent calibration errors. Though the added variables improve the agreement between the fitted intensities and the synthetic data set, the modulation matrix errors actually increased for the fits with more variables.

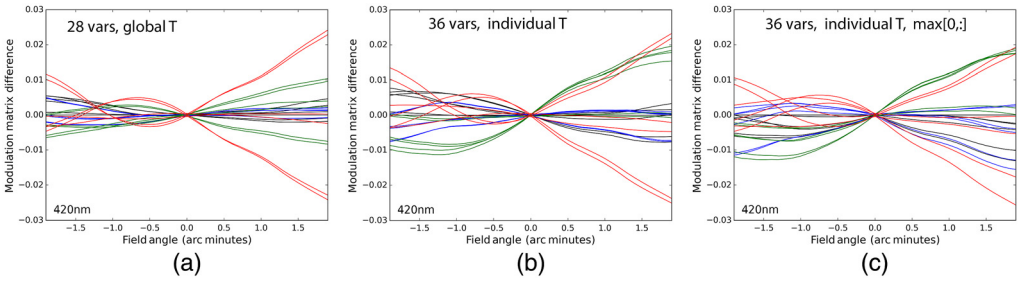

Fig. 34 The modulation matrix element variation from field center. Each color shows a different Stokes parameter with I modulation in black, Q in blue, U in green, and V in red. There are six modulation states per Stokes parameter. (a) The 28 variable global transmissions model. (b) The 36 variable individual transmissions model. This is nearly identical to the Max[0,:] modulation matrix normalization for the 36 variable individual transmissions model. (c) The relative polarization model.

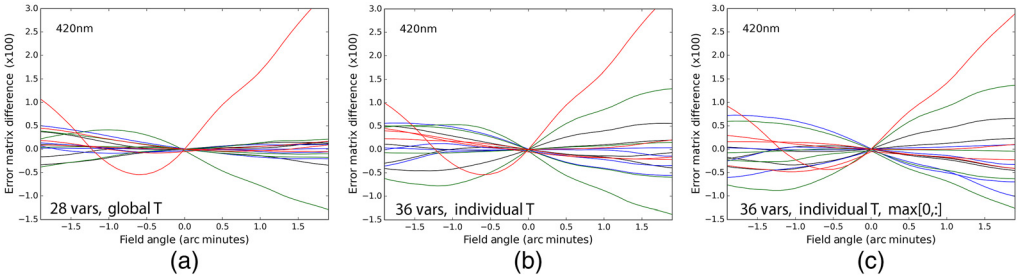

Fig. 35 The error matrix elements across the field of view multiplied by 100. Each color shows a different Stokes parameter with four matrix elements per Stokes parameter. (a) The 28 variable global transmissions model. (b) The 36 variable individual transmissions model. This is nearly identical to the Max[0,:] modulation matrix normalization for the 36 variable individual transmissions model. (c) The relative polarization model.

9.10 *B.10 Error Matrix with Field Angle*

We can define an effective field angle within which the calibration inaccuracies stay below certain thresholds. We showed in HS17[61] how the mirror coating behavior with incidence angle created field-dependent polarization. Figure 35 shows the error matrix variation with field angle at 420 nm wavelength.

9.11 *B.11 Error Matrix with Wavelength*

Figure 36 shows the error matrix variation with wavelength for a 114-arcsec field angle. No clear large trend is obvious with wavelength. Figure 36(a) shows the 28 variable global transmissions model. Figure 36(b) shows the 36 variable relative transmissions model with slightly reduced outliers but slightly worse overall errors. Figure 36(c) shows the Max[0,:] modulation matrix normalization for the 36 variable relative transmissions model. A few terms drop strongly toward longer wavelengths but several other terms stay constant or even increase toward long wavelengths. As we showed previously in HS18b[66] and H20,[86] retarder spatial variation leads to errors that decrease as λ^{-1}. However, the polarizer transmission has a spatial scale similar to the beam footprints with inhomogeneity throughout the aperture. The retarder transmission is quite uniform at levels below measurement noise of 0.02% except for the few small patches of optical contact defect.

9.12 *B.12 Error Matrix to 10 Arc Second Field Angles*

The error matrix elements mostly reduce below 0.05% within the inner $\pm$1-arcsec field angle. Not much difference is seen between the various algorithms for our simulations at small field

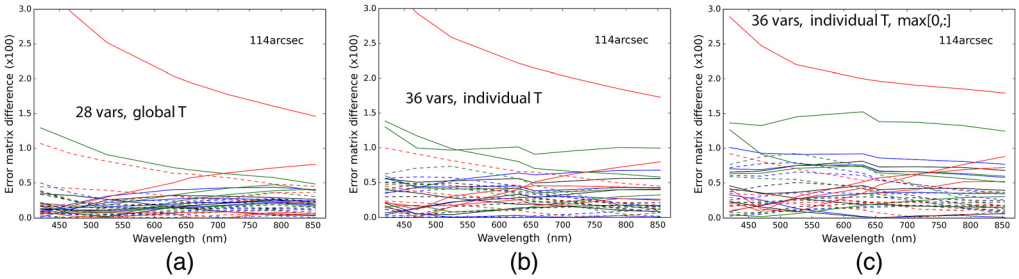

Fig. 36 The error matrix elements at a $\pm$114 arcsec field angle across wavelength. Each value has been multiplied by 100. Each color shows a different Stokes parameter with four matrix elements per Stokes parameter. (a) The 28 variable global transmissions model. (b) The 36 variable individual transmissions model. This is nearly identical to the Max[0,:] modulation matrix normalization for the 36 variable individual transmissions model. (c) The relative polarization model.

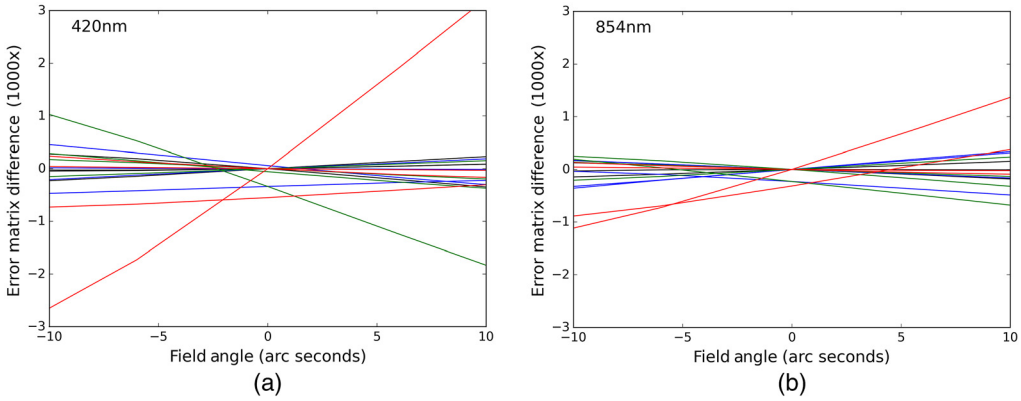

Fig. 37 The error matrix elements across the field of view multiplied by 1000. Each color shows a different Stokes parameter with four matrix elements per Stokes parameter. (a) 420 nm and (b) 854 nm. We show only the inner ±10 arcsec field angle with both wavelengths plotted on the same vertical scale of ±0.003. Note this is a 10× smaller scale than Fig. 14.

angle. Figure 37 shows the error matrix variation with field angle using the nominal 28 variable model for two distinct wavelengths: 420 and 854 nm. The graphics cover only the inner ±10-arc sec field angle on the same vertical scale in parts per thousand with the range of ±0.003 in each error matrix element. The error matrix magnitudes stay below an absolute value of 0.001 within a few arc seconds field angle. As we have included the ∼2.5 mm decenter of the calibration optics, these terms do not go to zero for the optical bore sight. We note that the DKIST beam is only currently stabilized to ±9.7-arc sec field angle on the coudé laboratory when the ao system is not in use. Calibrations with uncorrected instruments are presently subject to errors at magnitudes per Fig. 37. Certainly with future improvements to the centering of the GOS optics and alignment improvements, the inner field angles will be limited by other systematic errors.

10 Appendix C. Lab Metrology and Additional Optics

We built a lab setup for spatial mapping of transmission and high contrast polarizing optics. Images of the optomechanical setup are shown in Fig. 38. We have a motorized linear translation stage for 300 mm of horizontal travel and 150 mm of vertical travel. A dual-channel configuration was made with various filters or windows functioning as a beam splitter between NIR and VIS spectrographs.

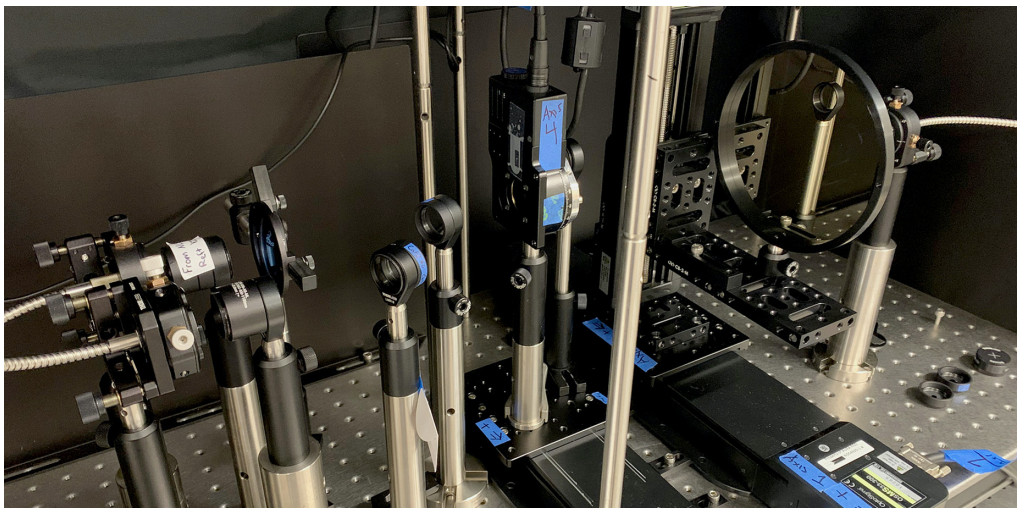

Fig. 38 The new Maui lab spatial mapping setup with a 6 in. diameter optic for scale.

10.1 *C.1 Lab Spectrograph Setups for Spatial and Spectral Mapping*

Our Boulder-based setup is called the NSO Laboratory Spectropolarimeter (NLSP) and is described in H19.[67] We made improvements to this NLSP setup with a 4096-pixel sensor unit described in H20.[86] We created a modified laboratory setup in the new NSO Maui laboratory for this work. The Maui building is named the DKIST Science and Support Center (DSSC) with the NSO DSSC spectropolarimeter (NDSP) as the new metrology tool.

We added high dynamic range capability using an Avantes CCD-based spectrograph on Maui. We also create a high spectral resolving power setup capable of resolving interference fringes in transmission using an Avantes dual-channel CMOS sensor-based EVO system. The CCD-based system presented here is a second copy of our NLSP unit H19[67] where we cover 380 to 1200 nm wavelength in over 1000 spectral pixels with roughly 1.4-nm spectral resolving power.

We procured this dual-bench EVO unit (DEVO) with two separate 4094 pixel CMOS sensors fed by two separate fibers to provide high spectral resolving power. There are roughly 27 useful background reference pixels on the short wavelength side of both sensors and another 24 masked reference pixels on the long wavelength side for both these systems. We extract roughly 4030 useful spectral pixels for each system for 8060 total independent wavelength measurements from 385 to 951 nm in the DEVO. The two spectrographs overlap between 600 and 628 nm wavelength. The visible unit inside the DEVO samples at 0.07 nm per pixel at 390 nm wavelength falling to 0.05 nm per pixel at 620 nm wavelength. The design optical FWHM is 0.14 nm for this system with the 10-μm wide slit installed. This samples roughly two spectral pixels per FWHM on the short wavelength side falling to 2.8 pixels per FWHM on the long wavelength side. This system delivers a spectral resolving power of 2800 at 395 nm wavelength rising to 4400 at 610 nm wavelength. The infrared unit in the DEVO samples at 0.10 nm per pixel at 620 nm falling to 0.07 nm per pixel at 950 nm wavelength. The design optical FWHM is 0.25 nm for this system with the 10-μm wide slit. This corresponds roughly to 2.5 pixels per optical FWHM on the short wavelength side falling to 3 on the longer wavelength side. This NIR system delivers a spectral resolving power of 2400 on the short wavelength side of 600 nm wavelength rising to 3800 at 950 nm wavelength. We detail the detection and use of interference fringe measurements here to assess polarizer substrate flatness. We also use the reference pixels provided by this new sensor architecture to provide much more stable background reference as required for high dynamic range measurements of contrast above 1 part per 50,000. The different lab setups used various combinations of spectrographs but performance is as expected given the range of spectral resolving powers and sampling. We collected extensive metrology on the several polarizers including both spatial and spectral variation of transmission, contrast, and orientation of maximum extinction.

10.2 *C.2 Sapphire CalPol*

The sapphire CalPol was mounted in a DKIST rotary stage polarizer cell and then tested in the Maui DEVO setup. With this new higher spectral resolving power setup, we detect the spectral interference fringes anticipated for these thin polarizer substrates. We show here the spatial and spectral properties for transmission, contrast, and orientation of maximum extinction in the presence of the transmission interference fringes.

10.2.1 *C.2.1 Sapphire CalPol: transmission spectra and mapping aperture variation*

Transmission for the linear polarization state perpendicular to wires was measured for a range of beam footprints and durations. We set the analyzer to wire-parallel polarization orientation derived from contrast maps. We repeated the spatial transmission mapping several times with a range of beam diameters and different spatial samples to assess the impacts of temporal variation and illumination conditions on the results. We measured spatial and spectral oscillation patterns in transmission that were stable between several repeated mapping configurations. After applying dark subtraction as well as frame by frame reference pixel correction with the

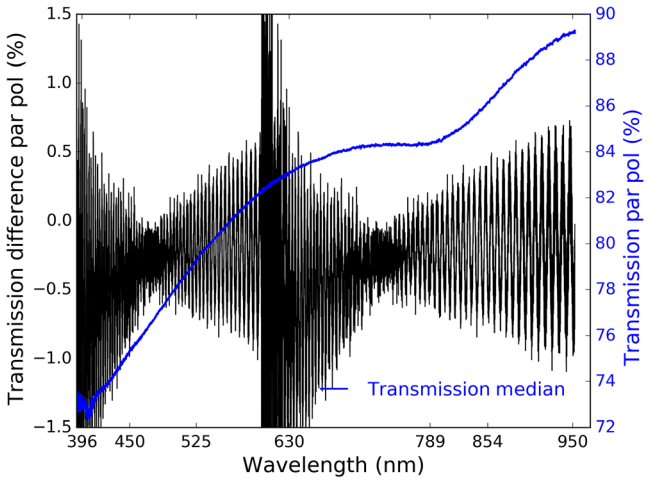

Fig. 39 The aperture-median transmission spectrum of the sapphire C-plane polarizer upgrade for the polarization state perpendicular to the wires is shown as the thicker blue line using the right-hand *Y* axis. The thin black lines show examples of deviations from the median curve for two individual spatial locations using the left-hand *Y* axis. The aperture oscillations are obvious to the eye. At longer wavelengths, the width of the black curves corresponds to resolving significant interference fringes, not to system noise.

DEVO sensor reference pixels, we also apply the correction for lamp temporal variation. We reduce the lamp brightness temporal change to better than $\pm 0.005\%$, with the 9.5-min calibration cadence by interpolating frequent lamp calibrations onto our temporal data sets.

The aperture-median spectrum for the transmission of polarization perpendicular to the wires is shown as the solid blue curve in Fig. 39 using the right-hand *Y* axis. The spatial variation in transmission is a narrow envelop following this median curve $\pm 1.5\%$ with oscillations and interference fringes dominating the deviations from median. We show a few example spatial locations in Fig. 39. Note that the single-surface Fresnel losses are 7.9% at 390 nm falling to 7.4% at 950 nm wavelength.

We show two selected spatial maps of transmission in Fig. 40. Maps were made after applying a nonlinear spectral averaging procedure to achieve a minimum signal level threshold per pixel. This bins between 2 and over 50 spectral pixels with a dependence on the detected intensity levels. Substantial spatial fringes are seen at full spectral resolving power for all wavelengths

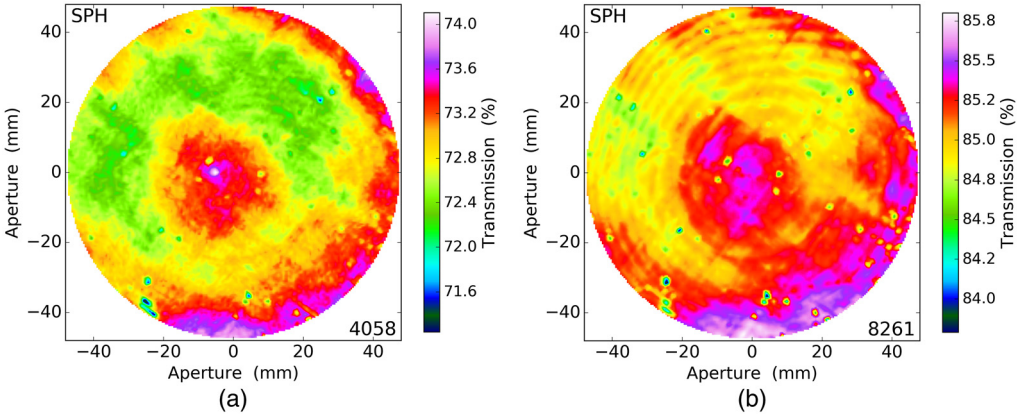

Fig. 40 The transmission maps derived from four maps of 12,481 spatial samples with 1.5 mm spatial masking and 0.75 mm radial steps to a maximum radius of 48 mm. We applied a spectral bin of several pixels to average over the interference fringes. Some rejection of vignetted spatial points on the far right side of the aperture are seen in the noncircular shape of the aperture. Wavelengths shown are (a) 405.8 nm and (b) 826.1 nm.

with this setup. We bin spectrally by additional factors of 3 to 10 pixels to average over spectral fringes. Some of the spectral fringes are still visible in Fig. 40(b) at amplitudes of a fraction of a percent. We use spectrally averaged transmission maps such as these later to remove the spatial variation of transmission and highlight the spectral transmission fringes.

10.2.2 *C.2.2 Sapphire CalPol: contrast and extinction orientation spectra*

The sapphire calibration polarizer was also tested in this DEVO setup for contrast and orientation of maximum extinction spatial variation. Spatial maps were run with a 4-mm-diameter lamp mask on a rosette with 4 mm spacing out to a 52-mm max radius and 547 spectra per map. We applied similar lamp flux temporal correction and sensor background drift corrections to every data set. Separate contrast spectra were recorded at 1951 spatial locations in an additional mapping set. The contrast spectra are shown in Fig. 41(a) after applying nonlinear spectral binning to a minimum signal to noise. We recorded 28 separate maps covering a range of 4.4 deg with multiple repeated spatial maps near the orientation of maximum extinction. Figure 41(b) shows the orientation of maximum contrast spectra at every spatial location derived from the 547 spatial sample maps using the 28 orientations. There is significant spatial variation detected at amplitudes of 0.04 deg along with some significant wavelength-dependent behavior. The solid blue curve shows the median orientation across the aperture at every wavelength in both sides of Fig. 41.

10.2.3 *C.2.3 Sapphire CalPol: mapping contrast spatial variation*

The spatial variation of contrast for the sapphire calibration polarizer is substantially lower than the fused silica polarizers. Example contrast spatial maps are shown in Fig. 42. Wavelengths shown are 399.6 nm in Fig. 42(a), 623.9 nm in Fig. 42(b), and 854.3 nm in Fig. 42(c). The results of single-map testing at a single analyzer orientation shown here are very similar in both spatial behavior and magnitude to the model fitting results (not shown). We note that there are several small areas of relatively low contrast, but these areas are consistently low at all wavelengths representing robust results. We also note that the average contrast change across the aperture is roughly a factor of two or less, and there are other polarizers shown in this paper that have spatial gradients in contrast up to factors of 6. This is a relatively uniform contrast aperture.

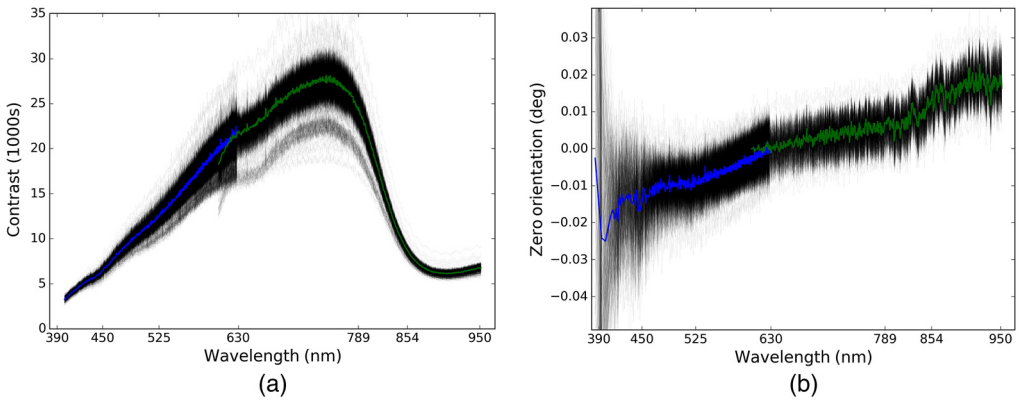

Fig. 41 (a) The contrast spectra and (b) orientation of maximum extinction spectra for the sapphire polarizer upgrade recorded with the DEVO setup. The contrast spectra represent the 1951 spatial samples for four repeated maps at constant analyzer orientation near the max extinction orientation. The extinction orientation spectra in (b) derived from 28 individual maps show good agreement between VIS and NIR spectrographs and spatial variation below ± 0.01 deg for all but the shortest wavelengths.

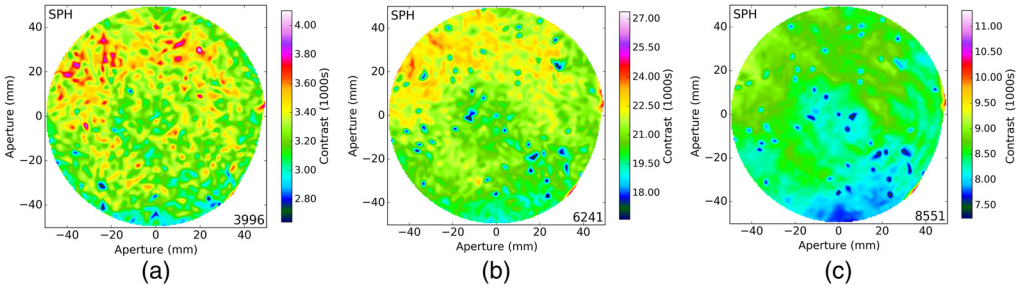

Fig. 42 The sapphire polarizer contrast spatial maps at maximum extinction orientation from 1951 spatial spectra with 4 mm spatial footprint and 2 mm radial steps in the rosette. Wavelengths show are (a) 436.4 nm, (b) 604.0 nm, and (c) 846.1 nm. These maps and the associated spectra are very similar to those derived at constant analyzer orientation.

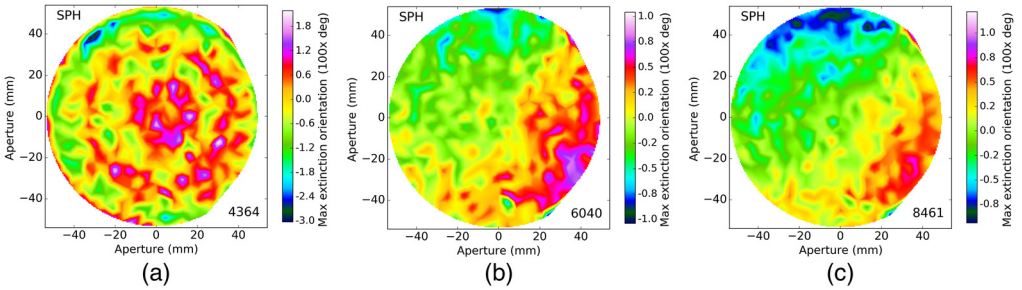

Fig. 43 The orientation of maximum extinction reconstructed from model fitting of 547 spatial spectra at 28 separate analyzer orientations with 4 mm spatial footprint and 4 mm radial steps. The orientation variation has been multiplied by 100 for clarity. Variation ranges by less than ± 0.02 deg. Wavelengths show are (a) 436.4 nm, (b) 604.0 nm, and (c) 846.1 nm.

10.2.4 *C.2.4 Sapphire CalPol: mapping extinction orientation spatial variation*

The sapphire polarizer also has relatively lower orientation variation than the fused silica polarizers. Example maps of spatial variation of the orientation for maximum extinction are shown in Fig. 43. Wavelengths shown are 422.1 nm in Fig. 43(a), 625.7 nm in Fig. 43(b), and 833.2 nm in Fig. 43(c). The spatial variation is <0.02 deg orientation with a linear change from left to right as the dominant feature at longer wavelengths. At the shorter wavelengths, the noise amplitude is larger and discerning a signal above these higher noise levels is difficult.

10.3 *C.3 Master Polarizer*

We collected a range of maps with the analyzer parallel for transmission of the S-polarization state and crossed for contrast measurement. We ran five repeated contrast maps overnight January 2, 2020, as well as an independent test the morning of January 2. We used a 500-ms exposure time and four coadds for 2 s total integration during contrast measurement. The beam diameter was set using the lamp mask with most data sets using a constant 1.5 mm diameter. The first higher SNR contrast map used a 2.5-mm-diameter lamp mask. We also collected multiple repeated S-polarization state transmission maps with an analyzer parallel to the wires. We used rosette patterns with spatial sampling of 1.25 mm for 4921 points, 2.0 mm for 1951 points, 2.5 mm for 1261 points, and 3.125 mm for 817 points.

10.3.1 *C.3.1 master polarizer: mapping contrast spatial variation*

We did not collect a range of angles near the orientation of maximum extinction but instead used a simpler method of fitting a single aperture-center spectrum to set the orientation. The master polarizer contrast spatial maps shown in Fig. 44 are reasonable maps of contrast as we have

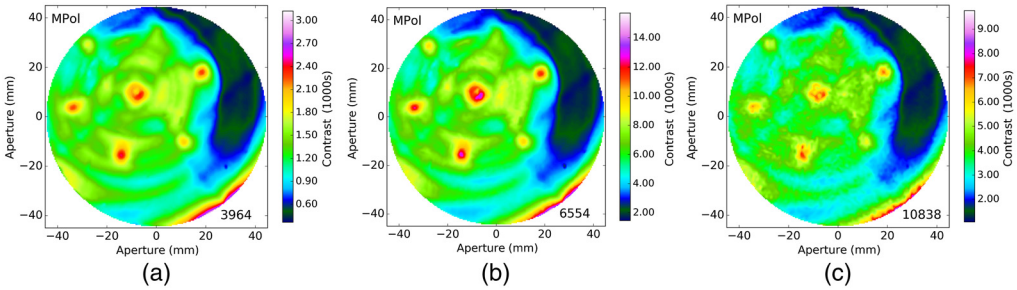

Fig. 44 The highest signal-to-noise contrast map for wavelengths (a) 396.4 nm, (b) 655.4 nm, and (c) 1083.8 nm.

shown the orientation of maximum extinction does not vary by more than a small fraction of a degree either with wavelength or across the aperture. The aperture is also slightly decentered as the laser tracker nests prevented our particular mounting technique from centering the optic in the range of the linear stages. We note that subsequently, larger stages were bought and integrated into our system.

10.3.2 *C.3.2 master polarizer: mapping transmission spatial variation*

Figure 45 shows the transmission map for this optic. Spatial variation of transmission is mostly on spatial scales larger than 10 mm with magnitudes of up to 5% transmission expected in a 30-mm diameter GOS beam footprint.

10.3.3 *C.3.3 master polarizer: transmission and contrast spectra*

Figure 46(a) shows 817 transmission spectra across the aperture. Figure 46(b) shows 4921 contrast spectra after also applying an 8-pixel boxcar average in wavelength to achieve sufficient SNR. This particular sensor has significant electronic instabilities impacting the data for this setup in the 600- to 800-nm bandpass seen in the transmission curves.

10.4 *C.4 Cryo-NIRSP Instrument Polarizers*

We show here tests on two separate UBB polarizers from the Cryo-NIRSP instrument filter wheel to compare against the UVT-240A-type polarizers. This UBB style has a different wire pitch and with no conformal coating over the wires. We note that these UBB-style polarizers had similar transmission and contrast spatial and spectral variation as the UVT-240A polarizers shown. We highlight here that the spatial and spectral variations of the orientation for maximum extinction are similar as well.

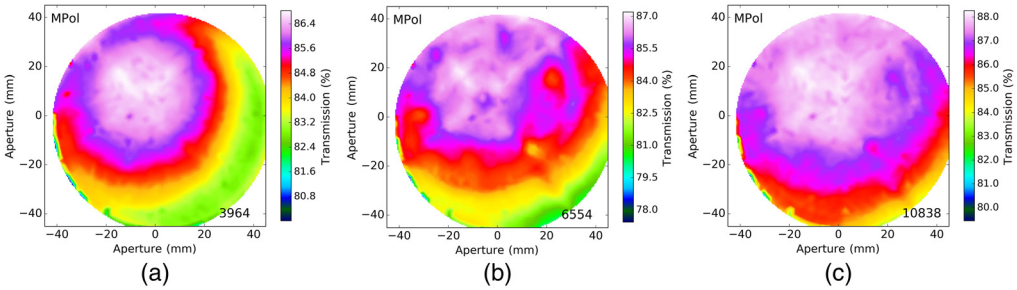

Fig. 45 The transmission map of the master polarizer with 0.6 h duration and 2.5 mm rosette for wavelengths (a) 396.4 nm, (b) 655.4 nm, and (c) 1083.8 nm.

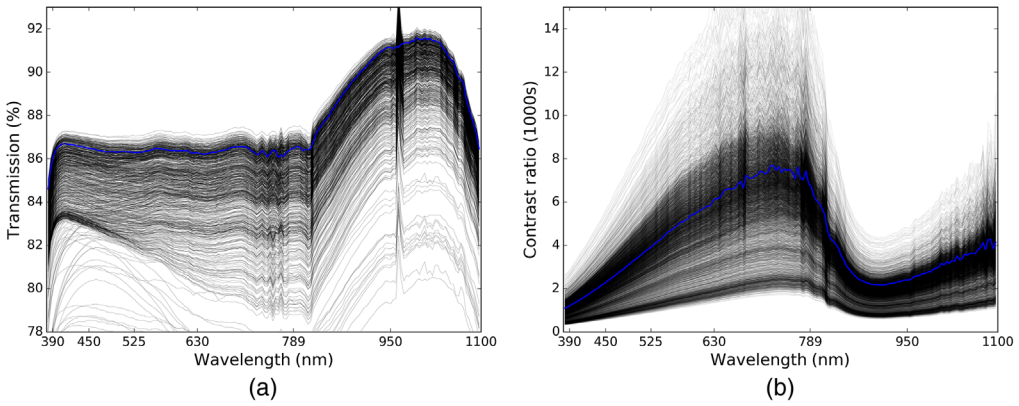

Fig. 46 (a) The transmission spectra for 817 spatial locations on a 3.125-mm spacing rosette. Five separate maps of 0.4 h duration were median-combined to produce spectra mitigating some sensor electronic issues. (b) The contrast spectra for 4921 spatial locations on a 1.25-mm spacing rosette. Five separate 4.3 h duration maps were averaged and then binned by 8× in wavelength to produce high SNR spectra. The solid blue curves in both graphics show the map center spectrum.

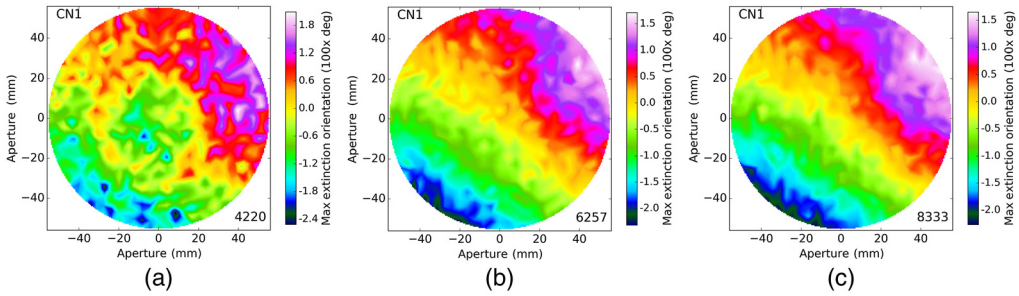

Fig. 47 The orientation of maximum extinction spatial maps for the Cryo-NIRSP instrument calibration polarizer number 1 UBB type wire grid reconstructed from 631 contrast spectra from March 2020 with 5-mm spatial masking and 4-mm radial steps with the dual-channel EVO NDSP setup.

10.4.1 *C.4.1 Cryo-NIRSP instrument polarizers: mapping extinction orientation spatial variation*

This new system was used to collect a large data set for deriving orientation angle for minimum transmission through the combined sample polarizer and analyzer. In Fig. 47, we show the spatial maps for the orientation of maximum extinction at 422.1 nm Fig. 47(a), 625.7 nm Fig. 47(b), and 833.2 nm Fig. 47(c). We do not observe the spatial pattern of high contrast spots seen in the UVT style polarizers.

10.4.2 *C.4.2 Cryo-NIRSP instrument polarizers: extinction orientation spectra*

We find similar spectral and spatial dependence to the angle of polarization in both Cryo-NIRSP UBB wire grid polarizers. We show the angle of polarization spectra for both UBBs in Fig. 48. The spatial variation is a smooth rotation of the angle of polarization at magnitudes of ± 0.04 deg spectrally and about the same spatially.

11 Appendix D. Sapphire Polarizer Alignment with Master Pol

The master polarizer was installed at the telescope and aligned to define an absolute polarization reference axis tied to the common tilt plane of the DKIST primary and secondary mirrors (M1:M2). Details can be seen in H21.[68] The VBI blue channel with one of the 4k Andor

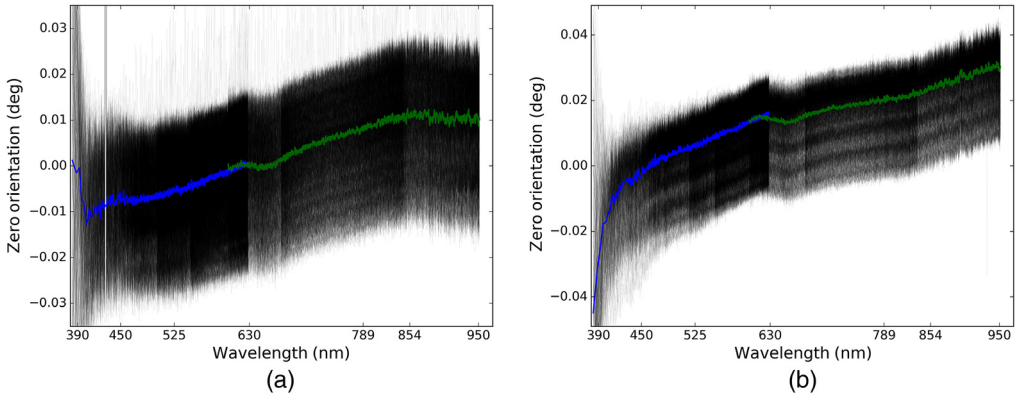

Fig. 48 The 631 spectra for the orientation of maximum extinction of the two Cryo-NIRSP fused silica substrate UBB polarizers from March 2020. The blue thick line shows the aperture average for the blue channel of the new dual-EVO system while green shows the aperture average for the red-optimized channel.

Balor cameras was used to collect unpolarized flux as there is no analyzer in the system.[20–26] We defocused the VBI camera significantly to avoid having any significant spatial structure in the images. We also note that the GOS polarizers are mounted well away from any instrument focal planes and thus are well away from conjugate to the VBI image plane. We fit the detected flux versus polarizer angle to detect the minimum in intensity through the crossed polarizers at GOS. The fit to Malus' law for rotating polarizers gives a three variable equation for the detected intensity $I_0 \cos^2(\theta + \theta_0) + C$. Provided a wide enough angular sampling is obtained, we can fit for the peak intensity for parallel polarizers separate from the background. The background is a combination of dark/bias residuals as well as actual flux from imperfect polarizer contrast. Data were recorded late in the afternoon in August 2020 with cumulus clouds very close to the observatory. With multiple repeated data sets any photometric issues could be reduced. We showed in H21[68] that the fitting precision is better than 0.001 deg. The photometric stability and other effects limit accuracy with more attempts to refine this preliminary alignment anticipated.

The critical parameter fit from Malus's law is the orientation offset (θ_0). This orientation allows us to rotate both calibration polarizers to their proper position in absolute telescope coordinates referenced to the M1:M2 tilt axes. Figure 49(a) shows the spatial variation for the best fit polarizer orientation (θ_0) across the 4 k × 4 k image of the VBI blue sensor. The color scale runs from ±0.013 deg in polarizer extinction orientation variation about the mean θ_0 of 57.304 deg.

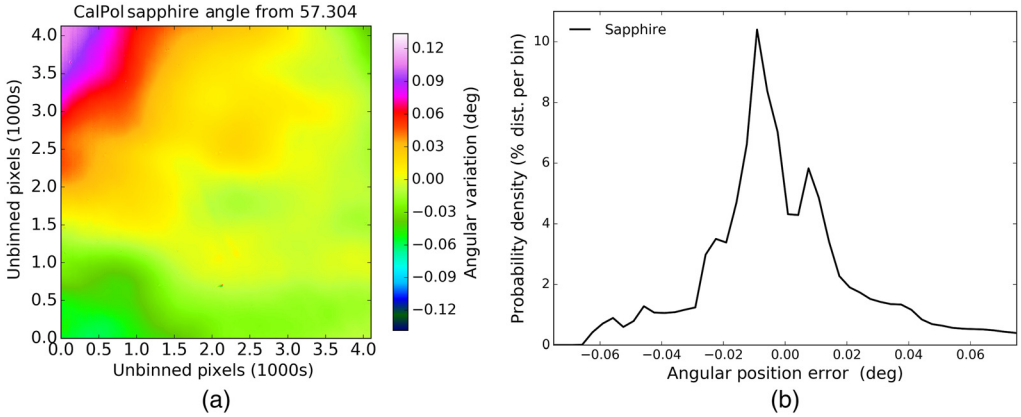

Fig. 49 The best fit polarizer orientation to achieve minimum VBI counts with the sapphire polarizer is shown in (a) across the 4096 × 4096 pixel VBI blue camera on a ±0.013 deg color scale. (b) The histogram of the best fit extinction orientations (θ_0) about the minimum of 57.304 deg.

Table 7 VBI 430 nm fit θ_0.

Name	θ_0	68%	95%
Saph	57.304 deg	±0.022 deg	±0.059 deg

The best fit orientations do vary spatially. We derive the confidence intervals in the precision of the estimated polarizer orientations. Figure 49(a) shows a histogram of the best fit orientations about the focal plane median value. The sapphire polarizer is shown about a median of 57.304 deg with bins running ±0.02 about the median. Table 7 shows the best fit orientation along with the confidence intervals for fit precision. We derive the cumulative distribution function (CDF) of errors from the histogram in Fig. 49. These CDFs show a measure of fit precision as assessed by spatial variation across the VBI sensor. We use them to define the 68% and 95% confidence without assuming Gaussian errors.

11.1 *D.1 Alignment of the Calibration Polarizers with NCSP and MasterPol*

We compare a single VBI wavelength fit with spectral data sets collected with NCSP similar to H21.[68] On Saturday August 15, 2020, we ran scripts that coordinated bursts of five NCSP spectra as the calibration polarizers were rotated down stream of the master polarizer. The MasterPol was set to the nominal orientation and the calibration polarizers rotated down stream. The benefit of NCSP is the simultaneous recording of more than 1500 spectral pixels with continuous wavelength coverage from 380 to 1650 nm. The complication is that the nominal NCSP optical configuration includes an analyzing polarizer in the beam, which couples polarization artifacts into this measurement. The rotating calibration polarizer does extinguish the >99.9% +Q beam created by the MasterPol. However, rotating the calibration polarizer rotates the linear polarization state injected into the telescope. The telescope has wavelength-dependent retardance, which also changes with time as the telescope tracks the sun. This retardance can cause the intensity passed by the NCSP analyzer to be skewed away from the nominal null between the master polarizer and calibration polarizer. We used the Az coude tracking mode to minimize system retardance by ensuring that the M5:M6 mirror group share a plane of incidence with

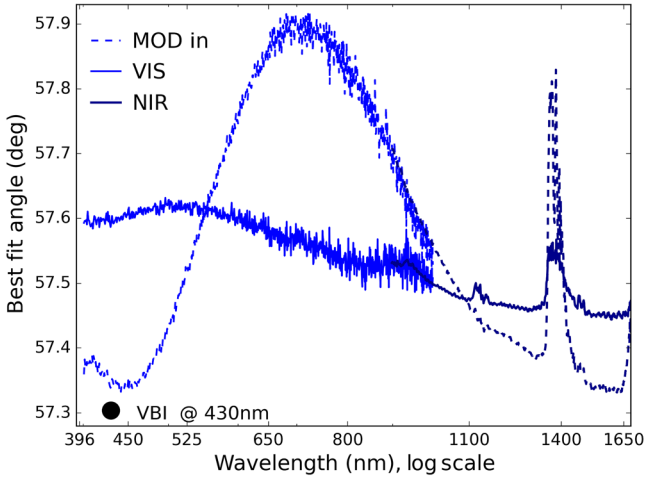

Fig. 50 The best fit angle to achieve minimum NCSP flux for the sapphire calibration polarizer. Each spectral pixel is fit independently. Blue shows the VIS spectrograph while dark blue shows the NIR spectrograph. The dashed lines show the fit results when the NCSP modulator is in the beam parked at the nominal 0 deg rotational position. The single large black dot shows the best fit angle derived from the 430-nm wavelength VBI data sets at 57.304 deg for the sapphire polarizer.

the coudé mirrors M7:NCSP. We also recorded data sets with and without the NCSP modulator in the beam. This in/out test can highlight systematic errors tied to the polarization response of NCSP. As VBI does not have an analyzer, the artifacts caused by system polarization are greatly reduced.

We perform the same fit to Malus's law as in VBI. We fit each spectral pixel separately but now have no spatial information as the NCSP fiber samples some particular patch of the focal plane. The NCSP fiber samples 2.9 arcsec of field using the 0.6-mm diameter fiber core and a magnification to 1.0 mm by the 5:3 focal length ratio of the lenses inside NCSP. There is significant wavelength dependents to the best fit angle for null flux at magnitudes of up to 0.5 deg with the modulator in the beam and 0.2 deg with the modulator out of the beam. The wavelength dependence of this null flux angle is shown in Fig. 50. Dashed lines show the modulator in fits with the larger wavelength dependencies. The atmospheric absorption band wavelengths are significantly impacted with the 1400 nm bandpass showing 0.3-deg systematic errors through the transparency variation. The coudé table angle was set to track the telescope azimuth, ensuring the M5:M6 mirror group and M7 to NCSP mirrors shared an incidence plane. The DKIST mirror coatings have zero retardance at wavelengths near 450 and 850 nm. The sapphire polarizer measurement is near 57.6 deg for the modulator-out fit at 400 nm wavelength falling to 57.4 deg at 1600 nm wavelength. The modulator insertion increases these wavelength dependence by 0.6 deg peak to peak but with a similar wavelength average. The NCSP fits are consistently 0.2 deg to 0.3 deg above the VBI fit of 57.304 deg.

12 Appendix E. Mueller Matrix Conventions

We summarize here the Mueller matrix terms and conventions for relating reflectivity and retardance to Mueller matrix elements outlined in several references.[88,89,94]

12.1 *E.1 Elliptical Retarders and Rotation Matrices*

Here, we describe elliptical retarder models as a rotation matrix. In the axis-angle representation of a rotation, two quantities are typically given. The first is a unit vector e indicating the direction of an axis for the rotation. The second is an angle θ describing the magnitude of the rotation about the axis. Only two numbers are needed to define the direction of a unit vector because the magnitude of e is a specified constraint. The equation for the rotation in matrix notation is thus a magnitude times the basis vector $\mathbf{r} = \theta e$. Alternatively, the three components of the vector can be specified and the magnitude computed from the vector components.

In Ref. 15, fits for elliptical retardance are applied to the DKIST six crystal retarder optics. We rewrite this rotation matrix equation in the published form while adopting a slightly different notation and fixing a typographical error in Eq. (26). We use a notation where $\cos(\theta)$ is denoted C_θ and $\sin(\theta)$ is denoted S_θ. We adopted the notation substitution $r_H = r_x$, $r_{45} = r_y$, and $r_z = r_r$ to explicitly denote an xyz coordinate frame for the rotation matrix ($\mathbb{R}_{ij}$). This substitution makes the notation similar to other references on rotation matrices as the $(H, 45, R)$ notation corresponds to naming conventions of horizontal as x or preservation of Stokes Q, the 45 as y or preservation of Stokes U and R as z or preservation of Stokes V. The rotations are about (x, y, z) axes, respectively, when the Poincaré sphere is represented in (x, y, z) coordinates. This equation is an axis-angle version of a rotation matrix:

$$\mathbb{R}_{ij} = \begin{pmatrix} \frac{r_x^2}{d^2} + \left(\frac{r_y^2+r_z^2}{d^2}\right) C_\theta & \frac{r_x r_y}{d^2}(1-C_\theta) + \frac{r_z}{d} S_\theta & \frac{r_x r_z}{d^2}(1-C_\theta) - \frac{r_y}{d} S_\theta \\ \frac{r_x r_y}{d^2}(1-C_\theta) - \frac{r_z}{d} S_\theta & \frac{r_y^2}{d^2} + \left(\frac{r_x^2+r_z^2}{d^2}\right) C_\theta & \frac{r_y r_z}{d^2}(1-C_\theta) + \frac{r_x}{d} S_\theta \\ \frac{r_x r_z}{d^2}(1-C_\theta) + \frac{r_y}{d} S_\theta & \frac{r_y r_z}{d^2}(1-C_\theta) - \frac{r_x}{d} S_\theta & \frac{r_z^2}{d^2} + \left(\frac{r_x^2+r_y^2}{d^2}\right) C_\theta \end{pmatrix}. \quad (26)$$

12.2 *E.2 Polarizer Mueller Matrices and Normalization*

$$\mathbf{M}_{ij} = \frac{1}{2}\begin{pmatrix} T_x + T_y & T_x - T_y & 0 & 0 \\ T_x - T_y & T_x + T_y & 0 & 0 \\ 0 & 0 & 2\sqrt{T_x T_y} & 0 \\ 0 & 0 & 0 & 2\sqrt{T_x T_y} \end{pmatrix}, \tag{27}$$

$$\mathbf{M}_{ij} = \frac{t_{\rm pol}}{2}\begin{pmatrix} 1 + p_y^2 & 1 - p_y^2 & 0 & 0 \\ 1 - p_y^2 & 1 + p_y^2 & 0 & 0 \\ 0 & 0 & 2p_y & 0 \\ 0 & 0 & 0 & 2p_y \end{pmatrix}, \tag{28}$$

$$\mathbf{M}_{ij} = \frac{t_{\rm pol}(1 + p_y^2)}{2}\begin{pmatrix} 1 & \frac{1-p_y^2}{1+p_y^2} & 0 & 0 \\ \frac{1-p_y^2}{1+p_y^2} & 1 & 0 & 0 \\ 0 & 0 & \frac{2p_y}{1+p_y^2} & 0 \\ 0 & 0 & 0 & \frac{2p_y}{1+p_y^2} \end{pmatrix}. \tag{29}$$

We show the Mueller matrix form used for a partial polarizer from Ref. 94 in Eq. (27). The variables T_x and T_y correspond to the intensity transmittances along the X and Y axes, respectively (horizontal and vertical).

A common substitution in solar telescope calibration is to describe the transmission of the more transmissive polarization state as the transmission of the polarizer ($t_{\rm pol}$). There is another substitution for the ratio of horizontal and vertical polarization state transmission as p_y^2. We show the Mueller matrix form used for the calibration polarizer in Eq. (28). We note that this matrix form needs to be further normalized for the [0,0] element to be equal to 1. If the input Stokes vector is purely unpolarized as $[1,0,0,0]^T$ then we recover an output Stokes vector with a transmission $t_{\rm pol}/2$ and a vector $[1 + p_y^2, 1 - p_y^2, 0, 0]^T$. We also note that for a pure Q input polarization of $[1,1,0,0]^T$, we recover a transmission of $t_{\rm pol}$ with the same pure Q output Stokes vector of $[1,1,0,0]^T$:

$$\mathbf{M}_{ij} = t_{\rm pol}^2\begin{pmatrix} p_y^2 & 0 & 0 & 0 \\ 0 & p_y^2 & 0 & 0 \\ 0 & 0 & p_y^2 & 0 \\ 0 & 0 & 0 & p_y^2 \end{pmatrix}. \tag{30}$$

The normalized form for the polarizer Mueller matrix is in Eq. (29) with the additional $(1 + p_y^2)$ term included with the transmission function. We note that around 630 nm wavelength for the DKIST nominal values, we use p_y^2 of roughly 5×10^{-5} and a parallel polarization state transmission of $t_{\rm pol} \sim 95\%$ for the calibration optic. Under these circumstances, the normalization puts the fit transmission in error at 0.005% magnitudes.

Extinction ratio (or contrast ratio) is often defined as the ratio of transmitted intensity through parallel polarizers to the transmitted intensity through crossed polarizers for an unpolarized input beam. We use the normalized form for the polarizer Mueller matrix from Eq. (29) and multiply by the same matrix form for a crossed polarizer with reversed signs in the [0,1] and [1,0] elements. We get the Mueller matrix for crossed polarizers per Eq. (30) as a scaled identity matrix.

We list in Table 8 some calculations about the quality of the beam created by the calibration polarizer. The contrast ratio goes as $(2p_y^2)^{-1}$. The VV term of the Mueller matrix for a polarizer goes as $2\mathrm{p}_y$. The DoP goes as $(1 - p_y^2)/(1 + p_y^2)$. For the DKIST calibration polarizers,

Table 8 Imperfect polarizer.

Contrast	p_y	VV	DoP (%)
200	0.05	0.1	99.5
312	0.04	0.08	99.7
555	0.03	0.06	99.8
1250	0.02	0.04	99.92
5000	0.01	0.02	99.98
20,000	0.005	0.01	99.995
31,250	0.004	0.008	99.997
55,556	0.003	0.006	99.998

metrology shows contrast above 500 for all wavelengths. We note that the converging $F/13$ beam on a retarder creates depolarization terms of order 0.5% per Ref. 15.

Acknowledgments

This work was supported by the National Science Foundation's (NSF's) Daniel K. Inouye Solar Telescope project (DKIST). DKIST is operated by NSF's National Solar Observatory under a cooperative agreement with the Association of Universities for Research in Astronomy, Inc. (AURA). DKIST is located on land of spiritual and cultural significance to Native Hawaiian people. The use of this important site to further scientific knowledge is done so with appreciation and respect. We are honored to have the opportunity to conduct astronomical research on Haleakala on the Island of Maui in Hawaií. We recognize and acknowledge the very significant cultural role and reverence that this site has to the Native Hawaiian community. The Polarimetry Analysis & Calibration (PA&C) team worked diligently to design, install, test, and assist with the various metrology tools available to the community. This includes scientific input from David Elmore and Christian Beck as well as the PA&C team: Andy Ferayorni, Scott Gregory, Austin Kootz, Chris Runyan, Wes Cole, and many others. This project would not have been possible without the massive effort of the DKIST construction team. In particular, the summit team for their dedication and for dealing with all the challenges from building such a complex custom facility. Amanda White acknowledges funding from the George Ellery Hale Graduate Fellowship at University of Colorado Boulder. Thanks to Lucas Tarr for discussing many variable fitting techniques and for having a very large white board full of equations. We thank Moxtek and their staff Eric Gardner and Alex Gao for engagement with us on upgrade projects and many technical conversations about polarizer performance. Thanks goes to Meadowlark Optics staff, the metrology and analysis from Michael Kraemer, assistance from Larry Opila on metrology equipment, spectroscopy, data analysis, and also for numerous lengthy physics discussions with the one and only Tom Baur. This research made use of Astropy, a community-developed core Python package for Astronomy.[105,106]

References

1. T. R. Rimmele et al., "The Daniel K. Inouye Solar Telescope – observatory overview," *Solar Phys.* **295**, 172 (2020).
2. J. P. McMullin et al. "Construction status of the Daniel K. Inouye Solar Telescope," *Proc. SPIE* **9145**, 914525 (2014).
3. S. L. Keil et al., "ATST: the largest polarimeter," in *Solar Polarization 6. Proc. Conf.*, Maui, Vol. 437, p. 319 (2011).

4. T. R. Rimmele et al., "Instrumentation for the advanced technology solar telescope," *Proc. SPIE* **5492**, 944 (2004).
5. J. Marino, E. Carlisle, and D. Schmidt, "Simulation of DKIST solar adaptive optics system," *Proc. SPIE* **9909**, 99097C (2016).
6. J. P. McMullin et al., "Construction status of the Daniel K. Inouye solar telescope," *Proc. SPIE* **9906**, 99061B (2016).
7. L. C. Johnson et al., "Status of the DKIST system for solar adaptive optics," *Proc. SPIE* **9909**, 99090Y (2016).
8. D. F. Elmore, S. R. Sueoka, and R. Casini, "Performance of polarization modulation and calibration optics for the Daniel K. Inouye Solar Telescope," *Proc. SPIE* **9147**, 91470F (2014).
9. D. F. Elmore et al., "The Daniel K. Inouye solar telescope first light instruments and critical science plan," *Proc. SPIE* **9147**, 914707 (2014).
10. P. Sekulic et al., "Daniel K. Inouye solar telescope optical alignment plan," *Proc. SPIE* **9906**, 990653 (2016).
11. R. Hubbard, S. Craig, and R. Kneale, "Daniel K. Inouye Solar Telescope systems engineering update," *Proc. SPIE* **9911**, 99112F (2016).
12. S. R. Sueoka, R. A. Chipman, and D. F. Elmore, "Characterization of DKIST retarder components with polarization ray tracing," *Proc. SPIE* **9293**, 929308 (2014).
13. D. F. Elmore et al., "Utilization of redundant polarized solar spectra to infer the polarization properties of the new generation of large aperture solar telescopes," *Proc. SPIE* **7735**, 77354E (2010).
14. D. Elmore, "Telescope calibration using polarization calibration data," *Astron. Nachr.* **331**(6), 655–657 (2010).
15. S. Sueoka, "Polarization optical components of the Daniel K. Inouye Solar Telescope," PhD thesis, University of Arizona (2016).
16. J. C. Guzman and J. Ibsen, Eds., *Motor Control for 0.1-Meter Diameter Crystal Retarders on the Daniel K. Inouye Solar Telescope*, SPIE (2018).
17. A. Ferayorni et al., "DKIST controls model for synchronization of instrument cameras, polarization modulators, and mechanisms," *Proc. SPIE*, **9152**, 91520Z (2014).
18. W. Schmidt et al., "End-to-end simulations of the visible tunable filter for the Daniel K. Inouye Solar Telescope," *Proc. SPIE* **9908**, 99084N (2016).
19. W. Schmidt et al., "A two-dimensional spectropolarimeter as a first-light instrument for the Daniel K. Inouye Solar Telescope," *Proc. SPIE* **9147**, 91470E (2014).
20. F. Wöger, "DKIST visible broadband imager interference filters," *Proc. SPIE* **9147**, 91479I (2014).
21. A. Ferayorni et al., "Bottom-up laboratory testing of the DKIST visible broadband imager (VBI)," *Proc. SPIE* **9911**, 991106 (2016).
22. A. Beard, B. Cowan, and A. Ferayorni, "DKIST visible broadband imager data processing pipeline," *Proc. SPIE* **9152**, 91521J (2014).
23. P. Sekulic et al., "DKIST visible broadband imager alignment in laboratory: first results," *Proc. SPIE* **9908**, 99085A (2016).
24. A. Ferayorni, "Instrument control software for the visible broadband imager using ATST common services framework and base," *Proc. SPIE* **8451**, 845113 (2012).
25. F. Wöger and A. Ferayorni, "Accelerated speckle imaging with the ATST visible broadband imager," *Proc. SPIE* **8451**, 84511C (2012).
26. W. R. McBride et al., "ATST visible broadband imager," *Proc. SPIE* **8446**, 84461B (2012).
27. H. Socas-Navarro et al., "High precision polarimetry with the Advanced Technology Solar Telescope," *Proc. SPIE* **5901**, 590105 (2005).
28. K. Richards et al., "The adaptive optics and wavefront correction systems for the Advanced Technology Solar Telescope," *Proc. SPIE* **7736**, 773608 (2010).
29. S. Berukoff et al., "Petascale cyberinfrastructure for ground-based solar physics: approach of the DKIST data center," *Proc. SPIE* **9913**, 99131F (2016).
30. F. T. Watson et al., "Calibration development strategies for the Daniel K. Inouye Solar Telescope (DKIST) data center," *Proc. SPIE* **9910**, 99101G (2016).

31. C. Mayer, S. Wampler, and B. Goodrich, "World coordinate information for the Daniel K. Inouye Solar Telescope," *Proc. SPIE* **9913**, 99130S (2016).
32. W. H. Schubert, E. Petrak, and T. G. Baur, "Measurement of polarization assemblies for the Daniel K. Inouye Solar Telescope," *Proc. SPIE* **9369**, 93690N (2015).
33. A. G. de Wijn et al., "Preliminary design of the visible spectro-polarimeter for the Advanced Technology Solar Telescope," *Proc. SPIE* **8446**, 84466X (2012).
34. J. Sánchez-Capuchino, "Current concept for the 4m European Solar Telescope (EST) optical design," *Proc. SPIE* **7733**, 773336 (2010).
35. F. C. M. Bettonvil et al., "The polarization optics for the European Solar Telescope (EST)," *Proc. SPIE* **7735**, 77356I (2010).
36. M. Collados et al., "European Solar Telescope: project status," *Proc. SPIE* **7733**, 77330H (2010).
37. M. De Juan Ovelar et al., "Instrumental polarisation at the Nasmyth focus of the E-ELT," *Astron. Astrophys.* **562**, A8 (2014).
38. F. Joos et al., "Reduction of polarimetric data using Mueller calculus applied to Nasmyth instruments," *Proc. SPIE* **7016**, 70161I (2008).
39. C. U. Keller and F. Snik, "Polarimetry from the ground up," in *Solar Polarization 5: In Honor of Jan Stenflo ASP Conf. Ser.*, Vol. 405, p. 371 (2009).
40. C. U. Keller et al., "EPOL: the exoplanet polarimeter for EPICS at the E-ELT," *Proc. SPIE* **7735**, 77356G (2010).
41. C. U. Keller, "Solar polarimetry close to the diffraction limit," *Proc. SPIE* **4843**, 100 (2003).
42. M. Rodenhuis et al., "The extreme polarimeter: design, performance, first results and upgrades," *Proc. SPIE* **8446**, 84469I (2012).
43. R. Roelfsema et al., "The ZIMPOL high-contrast imaging polarimeter for SPHERE: design, manufacturing, and testing," *Proc. SPIE* **7735**, 77354B (2010).
44. J. Sánchez Almeida, "Instrumental polarization in the focal plane of telescopes. 2: Effects induced by seeing," *Astron. Astrophys.* **292**, 713–721 (1994).
45. J. Sánchez Almeida and V. Martinez Pillet, "Instrumental polarization in the focal plane of telescopes," *Astron. Astrophys.* **260**, 543–555 (1992).
46. J. Sánchez Almeida, V. Martinez Pillet, and A. D. Wittmann, "The instrumental polarization of a Gregory-Coude telescope," *Solar Phys.* **134**, 1–13 (1991).
47. W. Schmidt et al., "POLIS: a spectropolarimeter for the VTT and for GREGOR," *Astron. Nachr.* **324**, 300 (2003).
48. F. Snik et al., "Design of a full-Stokes polarimeter for VLT/X-shooter," *Proc. SPIE* **8446**, 844625 (2012).
49. F. Snik et al., "The upgrade of HARPS to a full-Stokes high-resolution spectropolarimeter," *Proc. SPIE* **7014**, 70140O (2008).
50. F. Snik, "Calibration strategies for instrumental polarization at the 10-5 level," *Proc. SPIE* **6269**, 62695P (2006).
51. H. Socas-Navarro et al., "Characterization of telescope polarization properties across the visible and near-infrared spectrum. Case study: the Dunn Solar Telescope," *Astron. Astrophys.* **531**, A2 (2011).
52. H. Socas-Navarro, "Polarimetric calibration of large-aperture telescopes. II. Subaperture method," *J. Opt. Soc. Am. A* **22**, 907 (2005).
53. H. Socas-Navarro, "Polarimetric calibration of large-aperture telescopes. I. Beam-expansion method," *J. Opt. Soc. Am. A* **22**, 539 (2005).
54. P. Spano et al., "Optical design of CAOS: a high-resolution spectropolarimeter for the Catania Astrophysical Observatory 0.91-m telescope," *Proc. SPIE* **5492**, 373 (2004).
55. K. G. Strassmeier et al., "PEPSI: the Potsdam Echelle polarimetric and spectroscopic instrument for the LBT," *Proc. SPIE* **7014**, 70140N (2008).
56. K. G. Strassmeier et al., "PEPSI spectro-polarimeter for the LBT," *Proc. SPIE* **4843**, 180 (2003).
57. J. Tinbergen, "Accurate optical polarimetry on the Nasmyth platform," *Publ. Astron. Soc. Pac.* **119**, 1371–1384 (2007).
58. C. Beck et al., "A polarization model for the German Vacuum Tower Telescope from in situ and laboratory measurements," *Astron. Astrophys.* **443**, 1047–1053 (2005).

59. C. Beck et al., "Polarimetric Littrow Spectrograph - instrument calibration and first measurements," *Astron. Astrophys.* **437**, 1159–1167 (2005).
60. L. Kleint et al., "GREGOR: Optics redesign and updates from 2018–2020," *Astron. Astrophys.* **641**, A27–10 (2020).
61. D. M. Harrington and S. R. Sueoka, "Polarization modeling and predictions for DKIST part 1: telescope and example instrument configurations," *J. Astron. Telesc. Instrum. Syst.* **3**, 018002 (2017).
62. D. M. Harrington, J. R. Kuhn, and A. L. Ariste, "Daytime sky polarization calibration limitations," *J. Astron. Telesc. Instrum. Syst.* **3**, 018001 (2017).
63. D. M. Harrington and S. R. Sueoka, "Polarization modeling and predictions for DKIST part 3: focal ratio and thermal dependencies of spectral polarization fringes and optic retardance," *J. Astron. Telesc. Instrum. Syst.* **4**(1), 018006 (2018).
64. D. W. Berreman, "Optics in stratified and anisotropic media: 4X4-matrix formulation," *J. Opt. Soc. Am.* **62**, 502 (1972).
65. M. W. McCall, I. J. Hodgkinson, and Q. Wu, *Birefringent Thin Films and Polarizing Elements*, Vol. 1, 2nd ed., Imperial College Press, London (2014).
66. D. M. Harrington and S. R. Sueoka, "Polarization modeling and predictions for DKIST part 4: calibration accuracy over field of view, retardance spatial uniformity, and achromat design sensitivity," *J. Astron. Telesc. Instrum. Syst.* **4**, 044006 (2018).
67. D. M. Harrington, S. R. Sueoka, and A. J. White, "Polarization modeling and predictions for DKIST part 5: impacts of enhanced mirror and dichroic coatings on system polarization calibration," *J. Astron. Telesc. Instrum. Syst.* **5**, 038001 (2019).
68. D. M. Harrington et al., "Polarization modeling and predictions for Daniel K. Inouye Solar Telescope, part 7: Preliminary NCSP system calibration and model fitting," *J. Astron. Telesc. Instrum. Syst.* **7**, 018004 (2021).
69. L. C. Johnson et al., "Quasi-static wavefront control for the Advanced Technology Solar Telescope," *Proc. SPIE* **8444**, 84443O (2012).
70. L. C. Johnson et al., "Solar adaptive optics with the DKIST: status report," *Proc. SPIE* **9148**, 91481S (2014).
71. J. Marino, "Expected performance of solar adaptive optics in large-aperture solar telescopes," *Opt. Eng.* **51**(10), 101709 (2012).
72. D. Schmidt et al., "A review of solar adaptive optics," *Proc. SPIE* **9909**, 99090X (2016).
73. M. Semel, "Spectropolarimetry and polarization-dependent fringes," *Astron. Astrophys.* **401**, 1–14 (2003).
74. D. Clarke, "Interference effects in compound and achromatic wave plates," *J. Opt. A: Pure Appl. Opt.* **6**, 1041–1046 (2004).
75. D. Clarke, "Effects in polarimetry of interference within wave plates," *Astron. Astrophys.* **434**, 377–384 (2005).
76. D. Clarke, "Interference effects in single wave plates," *J. Opt. A: Pure Appl. Opt.* **6**, 1036–1040 (2004).
77. D. Clarke, "Interference effects in Pancharatnam wave plates," *J. Opt. A: Pure Appl. Opt.* **6**, 1047–1051 (2004).
78. D. Clarke, *Stellar Polarimetry*, John Wiley & Sons, Weinheim (2009).
79. O. S. Heavens, *Optical Properties of Thin Solid Films*, Dover Books on Physics, Dover, New York (1965).
80. D. K. Aitken and J. H. Hough, "Spectral modulation, or ripple, in retardation plates for linear and circular polarization," *Publ. Astron. Soc. Pac.* **113**, 1300 (2001).
81. T. J. Harries and I. D. Howarth, "Linear spectropolarimetry of the Hα emission line of ζ puppis," *Astron. Astrophys.* **310**, 533 (1996).
82. D. M. Harrington et al., "Correcting systematic polarization effects in keck LRISp spectropolarimetry to 0.05 percent," *Publ. Astron. Soc. Pac.* **127**, 757–775 (2015).
83. F. Snik et al., "A multi-domain full-Stokes polarization modulator that is efficient for 300–2500nm spectropolarimetry," *Proc. SPIE* **9613**, 96130G (2015).
84. A. Derks, C. Beck, and V. Pillet, "Inferring telescope polarization properties through spectral lines without linear polarization," *Astron. Astrophys.* **615**, A22 (2018).

85. P. M. Rojo and J. Harrington, "A method to remove fringes from images using wavelets," *Astrophys. J.* **649**, 553–560 (2006).
86. D. M. Harrington et al., "Polarization modeling and predictions for DKIST part 6: fringe mitigation with polycarbonate modulators and optical contact calibration retarders," *J. Astron. Telesc. Instrum. Syst.* **6**, 038001 (2020).
87. E. Collett, *Polarized Light. Fundamentals and Applications*, Vol. 1, 1st ed., CRC Press, (1992).
88. R. A. Chipman, "Chapter 15: Polarimetry," in *Handbook of Optics*, M. Bass, ed., McGraw Hill, New York (2014).
89. R. A. Chipman, *Handbook of Optics: Chapter 14, Mueller Matrices*, Vol. 1, 3rd ed., McGraw Hill, New York (2010).
90. F. Snik and C. U. Keller, *Astronomical Polarimetry: Polarized Views of Stars and Planets*, Vol. 1, 2nd ed., Springer, Dordrecht (2013).
91. J. C. del Toro Iniesta, *Introduction to Spectropolarimetry*, Cambridge University Press, Cambridge (2003).
92. J. C. del Toro Iniesta and M. Collados, "Optimum modulation and demodulation matrices for solar polarimetry," *Appl. Opt.* **39**, 1637 (2000).
93. J. C. del Toro Iniesta and V. Martinez Pillet, "Assessing the behavior of modern solar magnetographs and spectropolarimeters," *Astrophys. J. Suppl. Ser.* **201**, 22 (2012).
94. R. A. Chipman, W. S. T. Lam, and G. Young, *Polarized Light and Optical Systems*, CRC Press, Boca Raton, Florida (2018).
95. S. Tomczyk et al., "Wavelength-diverse polarization modulators for Stokes polarimetry," *Appl. Opt.* **49**, 3580–3586 (2010).
96. A. G. D. Wijn et al., "Wavelength-diverse polarization modulators for Stokes polarimetry," *Solar Polarization 6. Proc. Conf.*, Maui, Vol. 437, p. 413 (2011).
97. A. Skumanich et al., "The calibration of the Advanced Stokes Polarimeter," *Astrophys. J. Suppl. Ser.* **110**, 357–380 (1997).
98. F. Snik, T. Karalidi, and C. Keller, "Spectral modulation for full linear polarimetry," *Appl. Opt.* **48**(7), 1337–1346 (2009).
99. A. G. de Wijn et al., "The polychromatic polarization modulator," *Proc. SPIE* **7735**, 77354A (2010).
100. J. Selbing, "SST polarization model and polarimeter calibration," Master's thesis, Dissertation, Stockholm (2005).
101. D. F. Elmore, "A polarization calibration technique for the Advanced Stokes Polarimeter, NCAR Technical Note," (1990).
102. K. Ichimoto et al., "Polarization calibration of the solar optical telescope onboard hinode," *Solar Phys.* **249**, 233–261 (2008).
103. M. Born and E. Wolf, *Principles of Optics*, 7th ed., Cambridge University Press, Cambridge (1999).
104. P. Hariharan, *Basics of Interferometry*, 2nd ed., Academic Press, Burlington (2007).
105. The Astropy Collaborationet al., "The Astropy project: building an inclusive, open-science project and status of the v2.0 core package," https://iopscience.iop.org/article/10.3847/1538-3881/aabc4f (2018).
106. The Astropy Collaborationet al., "Astropy: a community python package for astronomy," arXiv.org A33 (2013).

Biographies of the authors are not available.